

AD-A135 533

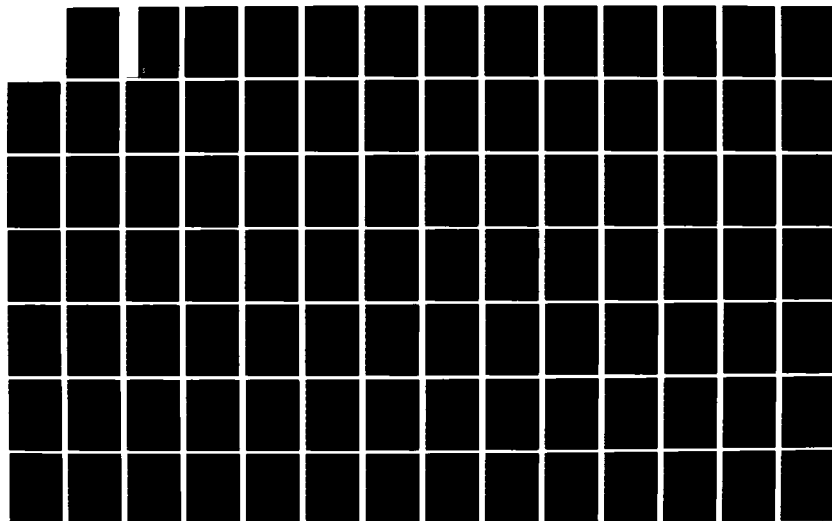
NUMERICAL SIMULATIONS OF THE NRL COLLECTIVE PARTICLE  
ACCELERATOR(U) MISSION RESEARCH CORP ALEXANDRIA VA  
R J BARKER NOV 83 MRC/WDC-R-073 N00014-83-C-0519

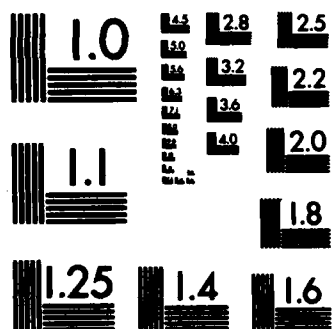
1/2

UNCLASSIFIED

F/G 12/1

NL





MICROCOPY RESOLUTION TEST CHART  
NATIONAL BUREAU OF STANDARDS-1963-A

2

MRC/WDC-R-073

**NUMERICAL SIMULATIONS OF THE NRL  
COLLECTIVE PARTICLE ACCELERATOR**

Robert J. Barker  
MISSION RESEARCH CORPORATION  
5503 Cherokee Avenue, Suite 201  
Alexandria, Virginia 22312  
(703) 750-3556

November 1983

Final Report for Period 1 July 1983 - 31 December 1983

**DISTRIBUTION STATEMENT A**  
Approved for public release;  
Distribution Unlimited

Prepared for: Scientific Officer  
Geophysical and Plasma Dynamics Branch  
Plasma Physics Division  
Naval Research Laboratory  
4555 Overlook Avenue, S.W.  
Washington, DC 20375

Attention: Dr. Peter J. Palmadesso

DTIC FILE COPY

**DTIC**  
**ELECTED**  
**DEC 8 1983**  
**S**  
**D**  
**H**

83 12 08 031

**NUMERICAL SIMULATIONS OF THE NRL  
COLLECTIVE PARTICLE ACCELERATOR**

Robert J. Barker  
MISSION RESEARCH CORPORATION  
5503 Cherokee Avenue, Suite 201  
Alexandria, Virginia 22312  
(703) 750-3556

November 1983

Final Report for Period 1 July 1983 - 31 December 1983

Prepared for: Scientific Officer  
Geophysical and Plasma Dynamics Branch  
Plasma Physics Division  
Naval Research Laboratory  
4555 Overlook Avenue, S.W.  
Washington, DC 20375

Attention: Dr. Peter J. Palmadesso

REPORT DOCUMENTATION PAGE		READ INSTRUCTIONS BEFORE COMPLETING FORM
1. REPORT NUMBER	2. GOVT ACCESSION NO.	3. RECIPIENT'S CATALOG NUMBER
4. TITLE (and Subtitle) Numerical Simulations of the NRL Collective Particle Accelerator		5. TYPE OF REPORT & PERIOD COVERED Final Report- 1 July 1983 - 31 December 1983
7. AUTHOR(s) Robert J. Barker		6. PERFORMING ORG. REPORT NUMBER MRC/WDC-R-073
9. PERFORMING ORGANIZATION NAME AND ADDRESS Mission Research Corporation 5503 Cherokee Ave., Suite 201 Alexandria, Virginia 22312		8. CONTRACT OR GRANT NUMBER(s) N00014-83-C-0519
11. CONTROLLING OFFICE NAME AND ADDRESS Naval Research Laboratory 4555 Overlook Ave., S.W. Washington, DC 20375		10. PROGRAM ELEMENT, PROJECT, TASK AREA & WORK UNIT NUMBERS
14. MONITORING AGENCY NAME & ADDRESS (if different from Controlling Office)		12. REPORT DATE November 1983
		13. NUMBER OF PAGES 106
		15. SECURITY CLASS (of this report) UNCLASSIFIED
		15a. DECLASSIFICATION/DOWNGRADING SCHEDULE
16. DISTRIBUTION STATEMENT (of this Report)  Approved for public release; distribution unlimited.		
17. DISTRIBUTION STATEMENT (of the abstract entered in Block 20, if different from Report)		Accession For NTIS GRA&I <input checked="" type="checkbox"/> DTIC TAB <input type="checkbox"/> Unannounced <input type="checkbox"/> Justification
18. SUPPLEMENTARY NOTES		By _____ Distribution/ _____ Availability Codes _____ Avail and/or _____
19. KEY WORDS (Continue on reverse side if necessary and identify by block number) Collective Particle Accelerator Numerical Simulation Relativistic Electron Beam Foilless Diode		Dist Special A-1
20. ABSTRACT (Continue on reverse side if necessary and identify by block number) Two-dimensional, electromagnetic, particle-in-cell numerical simulations of the NRL Collective Particle Accelerator (CPA) have been completed using the MAGIC code. Employing parameters which closely approximated the actual experiment, these simulations revealed the spontaneous formation of a virtual cathode which severely limited the net current flowing in the central beam of the device. These results explain experimental observations and indicate possible modifications which might make the CPA operational.		

## CONTENTS

	<u>Page</u>
1 INTRODUCTION .....	1
2 THE EXPERIMENTAL DEVICE .....	3
3 THE NUMERICAL MODEL .....	10
4 THE MAGIC SIMULATION CODE .....	19
5 RESULTS .....	23
5.1 "Cold Test" of the CPA .....	23
5.2 Hollow Beam Only .....	34
5.3 Dual Beam Case I .....	47
5.4 Central Beam Only .....	57
5.5 Dual Beam Case II .....	62
6 CONCLUSIONS .....	79
7 REFERENCES .....	80
APPENDIX DISSPATCH, A Software Package for Using NCAR Graphics with DISSPLA Commands .....	A-1

# FIGURES

		<u>Page</u>
FIGURE 1.	The experimental CPA device .....	4
2.	The simulation grid .....	14
3.	Scale drawing of the numerical model .....	16
4.	Voltage pulses applied in the CPA simulations .....	18
5.	$E_r$ at $t = 500\Delta t$ for "Cold Test" case .....	25
6.	$E_z$ at $t = 500\Delta t$ for "Cold Test" case .....	27
7.	$E_r$ at $t = 2500\Delta t$ for "Cold Test" case .....	28
8.	$E_z$ at $t = 2500\Delta t$ for "Cold Test" case .....	29
9.	Axial profiles of $E_z$ at $R = 20$ (top two) $E_z$ at $R = 5$ (bottom right) and $E_r$ at $R = 5$ (bottom left) .....	31
10.	Time histories of (a) voltage on hollow cathode, (b) voltage on rod cathode, and (c) $E_z$ at tip of rod cathode .....	33
11.	Particle plot for hollow beam case at $t = 500\Delta t$ ...	36
12.	Particle plot for hollow beam case at $t = 1000\Delta t$ ..	38
13.	$E_r$ at $t = 1500\Delta t$ for hollow beam case .....	39
14.	$E_z$ at $t = 1500\Delta t$ for hollow beam case .....	40
15.	Equipotential contours for a typical hollow beam foilless diode (from Reference 16) .....	41
16.	Axial profiles of $E_z$ (top) and $E_r$ (bottom) at $R = 1.94$ cm and $t = 1000\Delta t$ for beam case .....	43
17.	Axial profiles of $E_z$ at $R = 0.24$ cm and $t = 1000\Delta t$ for hollow beam case .....	44
18.	Hollow beam case time histories for (a) hollow cathode voltage pulse, (b) $E_z$ at (142,5), (c) $B_\theta$ at (34,24), and (d) $B_\theta$ at (129,24) .....	46
19.	Hollow beam at $t = 500\Delta t$ and $t = 1500\Delta t$ for dual beam case I. ....	48
20.	Both beams at $t = 2000\Delta t$ and $t = 2500\Delta t$ for dual beam case I. ....	49
21.	Both beams at $t = 3000\Delta t$ and $t = 3500\Delta t$ for dual beam case I. ....	50
22.	$E_z$ at $t = 3500\Delta t$ for dual beam case I. ....	51
23.	$E_r$ at $t = 3500\Delta t$ for dual beam case I. ....	52
24.	Axial profiles of $E_z$ (top) and $E_r$ (bottom) at $t = 3500\Delta t$ and $R = 18\Delta R$ for dual beam case I. ....	54
25.	Axial profile of $E_z$ at $R = 3\Delta R$ and $t = 3500\Delta t$ for dual beam case I. ....	55
26.	Case I time histories for (a) hollow cathode voltage, (b) rod cathode voltage, (c) $B_\theta$ at (34,24), and (d) $B_\theta$ at (129,24) for dual beam case I. ....	56

# FIGURES

		<u>Page</u>
FIGURE 27.	Central beam at $t = 500\Delta t$ and $t = 750\Delta t$ .....	58
28.	Central beam at $t = 1750\Delta t$ and $t = 2500\Delta t$ .....	59
29.	Axial profile of $E_z$ at $t = 2500\Delta t$ and $R = 3e\Delta R$ for central beam case .....	60
30.	Time history plots for radially and axially measured voltages of rod cathode (top left and right) and $E_z$ measured at tip of rod cathode and hollow cathode (bottom left and right) for central beam .....	61
31.	Time history plots for $B_\theta$ measured at $R = 1.41$ cm for distances of 0.22 (top left), 2.235 (top right), 4.565 (bottom left), and 19.955 cm (bottom right) downstream of rod cathode for central beam case .....	63
32.	Real space plot for both beams and phase space plot for central beam for dual beam case II at $t = 1750\Delta t$ .....	64
33.	Real space plot for both beams and phase space plot for central beam for dual beams case II at $t = 2000\Delta t$ .....	65
34.	Real space plot for both beams and phase space plot for central beam for dual beams case II at $t = 2250\Delta t$ .....	66
35.	Real space plot for both beams and phase space plot for central beam for dual beam case II at $t = 2500\Delta t$ .....	67
36.	Real space plot for both beams and phase space plot for central beam for dual beam case II at $t = 2750\Delta t$ .....	68
37.	Real space plot for both beams and phase space plot for central beam for dual beam case II at $t = 3000\Delta t$ .....	69
38.	Phase space plot ( $P_z$ vs. $Z$ ) beam at $t = 3000\Delta t$ in dual beam case II .....	71
39.	Plots of $P_R$ versus $P_z$ for central beam (left) and hollow beam (right) at $t = 3000\Delta t$ in dual beam case II .....	72
40.	Axial profile of $E_z$ at $R = 0.24$ cm (just inside central beam) at $t = 3000\Delta t$ for dual beam case II .....	74
41.	Axial profile of $E_z$ at $R = 1.94$ cm (just inside hollow beam) at $t = 3000\Delta t$ for dual beam case II .....	75



## FIGURES

	<u>Page</u>
Figure 42. Time history plots to voltage on hollow cathode (top left), voltage on rod cathode (top right), $E_z$ near tip of hollow cathode (bottom left), and $E_z$ near tip of rod cathode (bottom right) for dual beam case II .....	76
43. Time history plots for $B_\theta$ measured at $R = 1.41$ cm for distances of 0.22 (top left), 2.235 (top right), 4.565 (bottom left), and 19.955 cm (bottom right) downstream of rod cathode for dual beam case II .....	78
A-1. The "Expendable" DISSPLA calls .....	A-3
A-2. The NCAR replacement for DISSPLA's frame .....	A-6
A-3. The COMMON block for DISSPATCH .....	A-7
A-4. The DISSPATCH DISSPLA emulators .....	A-8
A-5. The PHYINT utility routine .....	A-15
A-6. Sample line-printer curve .....	A-16
A-7. Sample DISSPATCH curve .....	A-17
A-8. Sample line printer particle plot .....	A-19
A-9. Sample DISSPATCH particle plot .....	A-20

## 1. INTRODUCTION

The Plasma Physics Division of the Naval Research Laboratory has long played a leading role in advancing the physical understanding of intense charged particle beam generation and acceleration. A particularly noteworthy aspect of NRL's contribution to the field is presented by the series of innovative techniques proposed by the Lab to accomplish the acceleration of multi-kiloamp electron beams to energies well above 100 MeV. Among these suggested schemes is the Collective Particle Accelerator (CPA) concept introduced by Dr. Moshe Friedman (Reference 1) in 1977 and experimentally investigated by him for about three years thereafter. Although initial results were negative, recent theoretical analysis by Dr. Peter Palmadesso (Reference 2) indicates that some simple changes in the device's operating parameters could produce a positive result. Given the potential significance of such an accelerator to various programs underway in the Navy, it is highly desirable to resolve the question of the CPA's feasibility. Reconstructing the now dismantled experiment to test the suggested theoretical modifications would be an extremely costly and time-consuming undertaking which would be better justified if an independent verification of the theorized improvements were available. For this purpose, Mission Research Corporation (MRC) conducted two-dimensional, relativistic, electromagnetic, particle-in-cell simulations using a model of the CPA with realistic operating parameters. The results of these simulations have pinpointed the probable cause for the previous problems and indicate possible solutions which could spell success for a renewed experimental effort.

In the technical discussion that follows, the general research topic is described and the specific objective of this work is delineated. The discussion begins with a brief review of the experimental CPA device in question. The underlying, general theory is spelled out and the fundamental operative equations are listed. Thereafter follows a detailed

picture of the actual experimental apparatus constructed at NRL to test the feasibility of the concept. The observed negative results are then described. At that point, the specifics of this effort are initiated with a reduction of the actual physical device to a numerical model which is both physically valid and computationally tractable. Particular attention is paid to the assumptions which are made to arrive at the model. These assumptions determine which phenomena can or cannot manifest themselves in the simulations. Having fixed the subject of the study, the discussion then turns in Section 4 to the computational tool which was applied to its analysis. For this work MRC used its 2-1/2-D, electromagnetic, relativistic MAGIC code. A complete description is given of the code's capabilities and limitations. Section 5 presents the detailed results of the five major sets of simulation runs conducted with MAGIC to diagnose the CPA device. Numerous figures are included to provide as complete as possible a picture of the various physical phenomena at work. The major experimental observations are duplicated and their causes are carefully diagnosed. Clear conclusions are drawn in Section 6.

A short appendix is included at the end of this report to document a concise but important piece of software developed by MRC for the NRL VAX during the course of this work. This software adapts the NCAR Graphics System hosted on that machine to respond to commands for the much more widely used DISSPLA Graphics System. This feature has now been made available to all users of the machine.

## 2. THE EXPERIMENTAL DEVICE

Mission Research Corporation has applied its MAGIC simulation code to examine specific, critical physics questions involving the technical feasibility of NRL's Collective Particle Accelerator (CPA). These simulations now provide critical additional information to the parties concerned at NRL to determine the possible future of a revived CPA experimental effort. If the CPA is again brought to life, MRC proposes to continue its computational support of that program to optimize its performance. This section of the report reviews the NRL-CPA experiment and its chief results.

An approximate drawing of the CPA device experimentally tested at NRL by Dr. Moshe Friedman appears in Figure 1. The essential elements consisted of two opposing e-beam, foilless diodes installed at opposite ends of a five-meter-long, 4.76 cm diameter metal drift tube. Both diodes were fed from the same 1.0 megavolt, 100 nanosecond pulsed power generator. However, a transformer installed in the feed-line branch leading to the hollow cathode diode introduced an impedance mismatch in that line which resulted in an effective diode voltage at that end of 1.5 MV compared with the 1.0 MV of the opposing rod diode. The hollow-beam diode consisted of a 4.0 cm diameter tapered graphite cathode inserted into the flared anode structure at one end of the drift tube. The anode diameter increased from 4.76 to 15.24 cm over an axial distance of 12.7 cm. This flaring was accomplished in two parts: first, a diameter increase from 4.76 to 7.0 cm over a 5.1 cm axial distance, and then, an increase from 7.0 to 15.24 cm over the remaining 7.6 cm. This two-staged anode flaring was exactly repeated on the opposite end of the drift tube where the rod diode was placed. The axial positioning of the cathodes was not a fixed parameter in the experiments. The electron beam produced by this cathode had an outside diameter of about 4.0 cm and a radial beam thickness of about 0.2 cm. It carried a peak average current of about 20

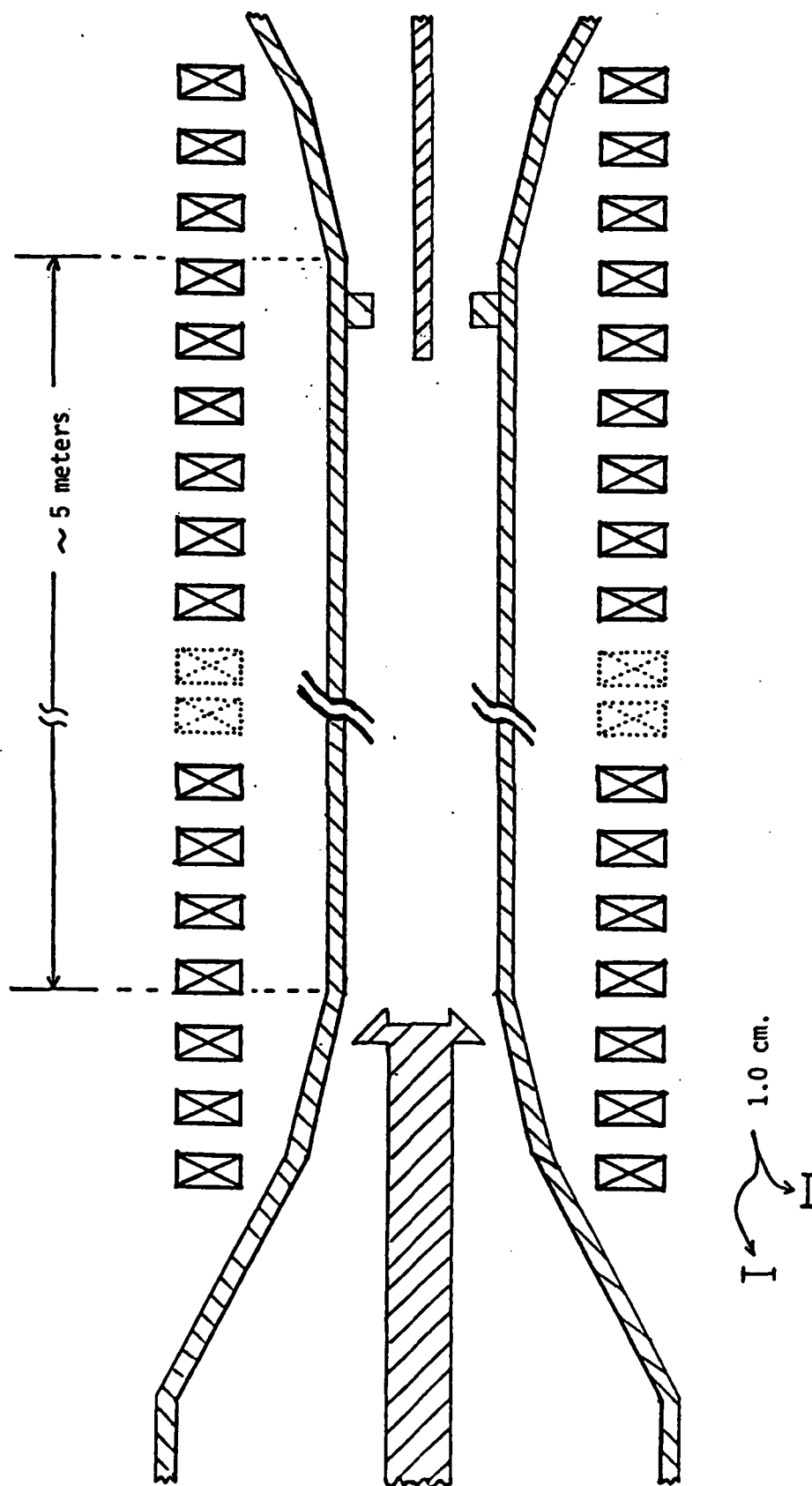


Figure 1. The Experimental CPA Device

kiloamperes. The tip of the rod cathode typically projected one or two centimeters into the drift tube. A graphite ring less than 1.0 cm in cross-section hugged the inner drift tube wall in the vicinity of the rod tip to act as a beam stop for the hollow electron beam. The axial position of this graphite beam-stop was again not a fixed experimental parameter. In some cases it was placed a short distance in front of in some cases a short distance behind the rod cathode tip. The rod cathode emitted a pencil e-beam of diameter 0.5 cm with a peak current of 2 kA and a current and voltage rise time of about 5.0 ns. In the actual CPA, the hollow electron beam would experience a density modulation sinusoidally to zero at a predetermined frequency. Uniformly positioned several centimeters apart down the entire external length of the drift tube were a series of magnetic field coils which could create either a constant 15 kilogauss  $B_z$  or an axially-rippled B-field consisting of an average 22.5 kilogauss component to which is added a ripple of the form  $B_1 \cos\left(\frac{2\pi z}{L}\right)$  where  $B_1 = 7.5$  kG and  $L = 60.0$  cm. (Note that the uniform field coil spacing was compressed for the last several coils at both ends of the tube to provide intensified  $B_z$ -fields behind the respective diodes.)

To describe the physics of the CPA device, we rely on excerpts from Reference 1. In that report, it is pointed out that the axial electric field component at  $r=0$ , produced by an annular, unneutralized, magnetically-focused intense relativistic electron beam (IREB) propagating through a drift tube of radius  $R$  can be approximated by

$$E_z = - \left[ \frac{1}{2\pi\epsilon_0} \right] \frac{\partial Q}{\partial z} \ln \frac{R}{r_b} - \left[ \frac{\mu}{2\pi} \frac{\partial I}{\partial t} \right] \ln \frac{R}{r_b} + \frac{Q}{2\pi\epsilon_0} \frac{1}{r_b} \frac{\partial r_b}{\partial z} \quad (1)$$

where  $Q$  is the beam's charge per unit length ( $Q = I/v_b$ ),  $I$  is the beam current,  $r_b$  is the beam radius, and  $v$  is the electron velocity. If the drift tube walls are covered with a thin dielectric layer of thickness,  $\delta R$ , and permeability,  $\epsilon$ , one finds

$$E_z = -\frac{\mu}{2\pi} \frac{1}{\beta^2 \gamma^2} \frac{\partial I}{\partial t} \ln \frac{R}{r_b} + \frac{\mu}{2\pi \beta^2} \frac{\epsilon}{\epsilon-1} \frac{\delta R}{R} \frac{\partial I}{\partial t} + \frac{Q}{2\pi \epsilon_0} \frac{1}{r_b} \frac{\partial r_b}{\partial z}. \quad (2)$$

Furthermore, by choosing

$$\frac{\delta R}{R} = \frac{\epsilon}{\epsilon-1} \frac{1}{\gamma^2} \ln \frac{R}{r_b} \quad (3)$$

Equation (2) reduces to

$$E_z = \frac{Q}{2\pi \epsilon_0} \frac{1}{r_b} \frac{\partial r_b}{\partial z}. \quad (4)$$

Now assume a charge density modulation of the IREB of frequency and wavelength,  $f$  and  $\lambda$  respectively, such that  $\lambda f = v$  and

$$Q(z, t) = \frac{Q_0}{2} \left[ 1 + \sin \left( \frac{2\pi}{\lambda} z - 2\pi f t \right) \right] \quad (5)$$

If an axially, sinusoidally rippled magnetic field with ripple wavelength,  $L$ , is now imposed in the drift tube, the annular beam will follow the B-field lines and have an axially varying radius of

$$r_b = r_0 + r_1 \cos \frac{2\pi z}{L}; \quad r_1 < r_0 \quad (6)$$

where  $r_0$  is the mean IREB radius and  $r_1$  is the amplitude of the radius ripples. Inserting (5) and (6) into (4) along with the assumption that the beam velocity,  $v$ , is approximately equal to the speed of light,  $c$ , yields

$$E_z = -\frac{1}{4} \frac{Q_0}{\epsilon_0} \frac{r_1}{r_0 L} \cos \left\{ \left[ 2\pi z \left( \frac{1}{\lambda} + \frac{1}{L} \right) - 2\pi ft \right] - \cos \left[ 2\pi z \left( \frac{1}{L} - \frac{1}{\lambda} \right) + 2\pi ft \right] + 2 \sin \frac{2\pi z}{L} \right\}. \quad (7)$$

Thus, there are two "waves" with phase velocities

$$v_{\phi 1} = v \frac{L}{\lambda + L}, \text{ for the forward wave, and} \quad (8)$$

$$v_{\phi 2} = -v \frac{L}{\lambda - L}, \text{ for the backward wave.}$$

The amplitude of these "waves" is given by

$$E_{z0} = \frac{Q}{4\epsilon_0} \left( \frac{r_1}{r_0 L} \right). \quad (9)$$

Since only the backward wave can have a phase velocity approaching  $c$ , only the backward wave can accelerate electrons. Note that both waves can accelerate ions but ion acceleration is beyond the scope of this proposed research.

In the experiments conducted to date with the device in Figure 1, the hollow beam density was not modulated so acceleration could not be tested. However, for the beam and rippled  $B_z$  that was in place,  $L = 0.60$  meter,  $r_1/r_0 = 0.17$ , and  $Q = I/c = 2 \times 10^4 / 3 \times 10^8 = 6.67 \times 10^{-5}$



coulomb/meter. Assuming that the hollow beam could be density modulated with  $\lambda \approx 2L$ , then Equation (8) predicts a phase velocity of  $c$  for the backward wave which, with this value for  $Q$  inserted into Equation (9) yields 530 kV/meter as the effective axial acceleration field. Over the full 5 meter length, this amounts to a 2.5 MV energy gain which should be easily observable experimentally. It is worth noting as well that an IREB propagating through a rippled magnetic field can produce significant microwave radiation if the field strength is below a critical value given by

$$B_C \approx \frac{2\pi}{L} \frac{mc}{e} \gamma \quad (10)$$

For the experimental parameters of  $L = 0.6$  and  $\gamma = 1 + 1.5/.511 = 3.9$ ,  $B_C$  becomes about 0.7 kG which is far below the average 15 kG baseline axial guide field. It is also important to note the axial and temporal scale lengths in the experiment. The relativistic electron gyroradius is given by

$$r_G = 1.7 \times 10^3 (\gamma^2 - 1)^{1/2} B^{-1} \text{ cm} \quad (11)$$

so that in the peak axial field of 30 kG,  $r_G \approx 0.22$  cm. Similarly, the relativistic electron gyroperiod is found to be about  $5 \times 10^{-11}$  second.

In the actual experiments that were run at NRL, the hollow beam was not density modulated and the central pencil beam apparently did not propagate down the full length of the tube (Reference 3). Thus, the experiment never proceeded to the point of testing the acceleration concept itself. Specifically, with the 20 kA hollow beam in steady state propagation down the full length of the five-meter tube (confirmed by damage patterns) the pencil diode voltage was ramped up from 0 to 1.0 MV over about five nanoseconds. The pencil diode current rose likewise from 0 to 2.0 kA over about the same five nanoseconds. The pencil beam was

never observed to reach the other end of the tube in the presence of the hollow beam. In fact, magnetic field probe measurements made just 50 cm downstream from the pencil diode failed to detect the presence of the pencil beam. Therefore, the most significant immediate question addressed by these numerical simulations of the device was the simple one of survivability of the central beam. This report documents the numerical duplication of all of the above experimental observations. In addition, it was found that the central beam does in fact propagate down the axis of the tube but that its current is drastically reduced due to the formation of an effective virtual cathode right next to the emitting tip of the central rod cathode.

Before describing these results in Section 5, the following two sections first detail the numerical model of the CPA which was used in this effort and then explains the major features of the MAGIC simulation code.

### 3. THE NUMERICAL MODEL

From a practical computational standpoint, it was clear that a reasonable simulation must be modeled upon a device significantly shorter than the one depicted in Figure 1 and one with some simplifications in the two beam injection regions as well. To arrive at that conclusion, consider the spatial and temporal resolution mandated by the physics of the problem. As stated in the previous section, the gyroradius for the 1.5 MeV electrons in the 30 kG magnetic field is about 0.22 cm with a gyroperiod of  $5.0 \times 10^{-11}$  second. Even more stringent, for the 1.0 MeV pencil beam these quantities become 0.16 cm and  $3.6 \times 10^{-11}$  second respectively. The maximum numerical grid spacings in either dimension and the timestep must be small enough to resolve those electron motions. (Luckily the beam currents are low enough so that the maximum azimuthal magnetic field strengths at the outer radius of the inner and outer beams are only 1.25 and 3.1 kG respectively which are small compared to the axial field.) Thus, the axial B-field strength peaks midway between the two diodes so the largest grid spacing in that region must be less than or equal to 0.16 cm. Actually, in the radial dimension there is even more severe a restriction, namely that which demands adequate spatial resolution along the electron-emitting cathode surfaces. The central rod cathode has an emitting tip only 0.25 cm in radius while the hollow cathode emits from a strip only 0.2 cm wide. Clearly, a radial cell spacing of 0.16 cm is grossly inadequate to resolve any radial beam profile. To rectify this, the rod cathode is given a radius of 0.32 cm and the hollow cathode emission region is widened to 0.24 cm. In addition, the radial cell spacing near those electrodes is shortened to 0.08 cm. Even with those new parameters, the rod beam emitter is only four cells wide and the hollow beam only three. Widening the beam radii further seems unwise if reasonable resemblance to the experiment is to be maintained. On the other hand, making  $\Delta R$  smaller than 0.08 cm seems unwise from a numerical standpoint due to the limitation of computer data

storage for the numerical mesh points and to the resultant time step shortening dictated by the Courant condition. Summarizing the spatial grid considerations thus far, it would seem desirable to utilize  $\Delta R$  and  $\Delta Z$  spacings of 0.16 cm except in the beam emission regions where a resolution of 0.08 is chosen in the radial dimension to provide an adequate numerical beam width and in the axial dimension to ensure accurate determination of the normal electric field for use in the Gauss' Law calculation of emitted charge. With regard to the simulation time step, it is desirable to resolve the minimum electron gyroperiod with at least five time steps to insure physical particle dynamics. This permits a maximum time step of about  $7.2 \times 10^{-12}$  second. The Courant numerical stability condition furthermore demands that the time step,  $\Delta t$ , satisfies the expression

$$\frac{1}{c^2 \Delta t^2} > \frac{1}{\Delta R^2} + \frac{1}{\Delta Z^2} . \quad (12)$$

For the smallest cells, near the cathode tips,  $\Delta R = \Delta Z = 0.08$  and, thus, the timestep is restricted to  $\Delta t < 1.886 \times 10^{-12}$  second. Given this temporal constraint, a choice of  $\Delta t = 1.40 \times 10^{-12}$  second was deemed quite reasonable.

Now consider the implications those values of  $\Delta R$ ,  $\Delta Z$ , and  $\Delta t$  have on conducting a simulation of the full five-meter-long CPA device. The least difficult starting point is the radial dimension. For convenience, the grid can be divided into five regions in  $R$  as follows:

(a) From  $R = 0$  to  $R = 0.48$  cm, use a uniform radial spacing with six cells of  $\Delta R = 0.08$  cm since this must resolve the electron motions of the central beam.

(b) From  $R = 0.48$  to  $R = 1.18$  cm, gradually expand the spacing in this particle-free region, spanning it with five cells whose  $\Delta R$ 's are 0.10, 0.12, 0.14, 0.16, and 0.18 cm respectively.

(c) From  $R = 1.18$  to  $R = 1.70$  cm, as one approaches the domain of the outer beam, the radial cell size must gradually decrease again. This is accomplished with four cells of  $\Delta R = 0.16, 0.14, 0.12,$  and  $0.10$  cm respectively.

(d) From  $R = 1.70$  to  $R = 2.10$  cm, again use a uniform radial spacing of  $\Delta R = 0.08$  cm; this time with five cells to span the beam region.

(e) From  $R = 2.10$  to  $R = 2.40$  cm, three radial cells of  $\Delta R = 0.09, 0.10,$  and  $0.11$  cm fill the remainder of the tube interior out to the cylindrical anode wall.

This gives a total of 24 cells spanning the computational region radially. To span 5.0 meters in the axial dimension with a  $\Delta Z = 0.16$  cm (ignoring the higher resolution needed immediately near the cathode tips) would require 3125 cells to yield a total of  $22 \times 3125 = 68,750$  two-dimensional data points for the full model. A simulation of that size is doable but totally impractical. Even modeling only one full 60 cm B-field cycle would require 8250 cells which would be possible but not practical if more than just one or two simulations are desired. To resolve the problem, it should first be decided to examine only one magnetic cycle,  $L$ . Furthermore,  $L$  should be shortened from the experimental value to as small as possible a size without sacrificing significant physics. In essence, this means that  $L$  must remain "many" times the value of the tube diameter of 4.8 cm. A good value for "many" is "5", which yields an  $L$  of about 24 cm. Furthermore, given the experimental uncertainties of the ripple field's generation, a lowering of the peak field from 30.0 to 25.0 kG hardly seems unreasonable. This relaxes the minimum cell size to about 0.19 cm. Such a value for  $\Delta Z$  would allow the use of 130 cells to span the entire CPA model axially. The problem has now assumed practical proportions and is ready for detailed modeling.

The simulation model which emerges from these considerations is drawn to scale in Figure 2. That figure depicts blow-ups of the two diode regions at either end of the tube. The treatment of the radial dimension is exactly as described in the previous paragraph. The axial dimension is a bit more complicated. Consider first the hollow cathode at the left end of the tube. It is no longer tapered as was the case experimentally. Instead, it is a 2.02 cm radius cylinder with a thickness of 0.24 cm and an axial depth of 1.08 cm. The "backplane" of the hollow cathode also defines one boundary endplane of the computational region. The "open", freespace region on this endplane between  $R = 2.02$  and  $R = 2.40$  cm represents the entrance port from the 1.5 MV power transmission line. Its axial recess from the cathode tip of more than twice its radial width is important for ensuring a proper numerical representation of the free boundary potential distribution. The volume between  $Z = 0$  and  $Z = 0.38$  cm is spanned by two axial cells of width,  $\Delta Z = 0.19$  cm. Over the final five axial steps in that transmission line recess,  $\Delta Z$  is decreased from 0.18 to 0.16 to 0.14 to 0.12 to 0.10 cm until the end of the cathode shank is reached at  $Z = 1.08$  cm. An axial cell width of no more than 0.08 cm (equal to the best radial resolution) is desired along the electron-emitting cathode tip to improve the accuracy of the calculation of  $E_z$  along that surface. This field value is used by the code to determine the amount of charge emitted from those surface cells each timestep. The newly emitted electrons must furthermore travel some finite distance from the cathode before achieving their maximum drift energies. Higher than average resolution of particle motion is desired over this critical phase so  $\Delta Z$  is increased only gradually over the next 1.43 cm. Specifically, the 11 cells from  $Z = 1.08$  to  $Z = 2.51$  cm are given the following  $\Delta Z$  values: 0.08, 0.09, 0.10, 0.11, 0.12, 0.13, 0.14, 0.15, 0.16, 0.17, and 0.18 cm. Filling the bulk of the tube length, from  $Z = 2.51$  to  $Z = 23.79$  cm, are 112 axial cells of  $\Delta Z = 0.19$  cm each. Thereafter, covering the

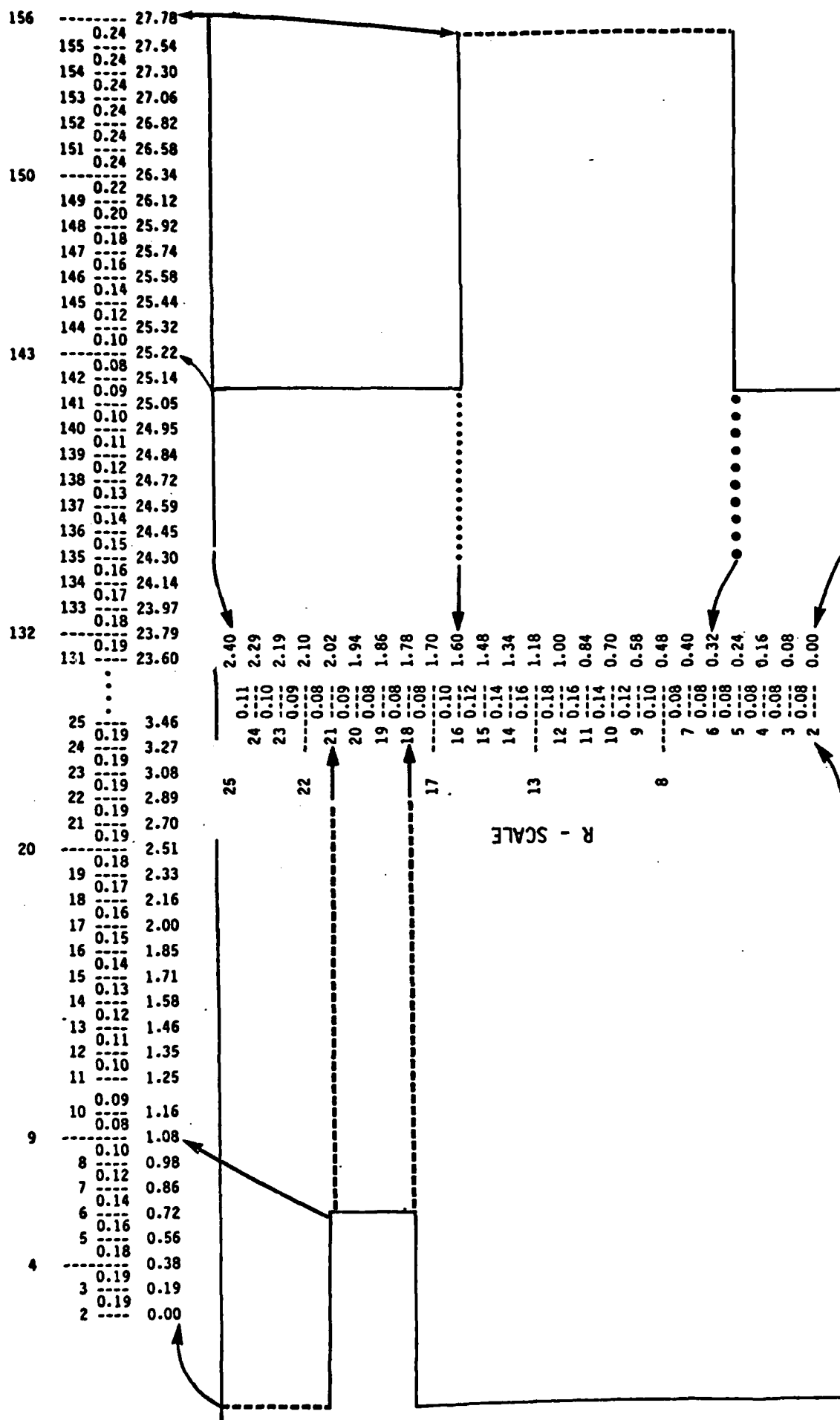
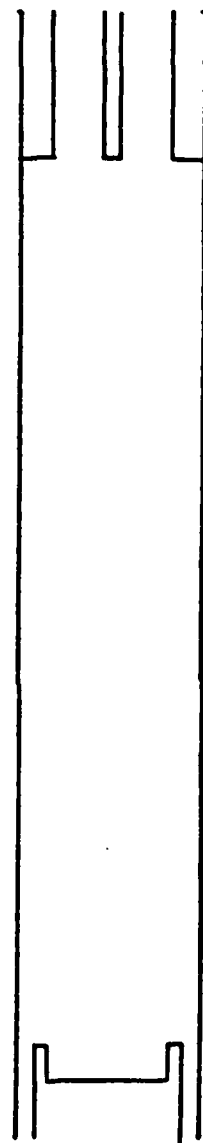


Figure 2. The Simulation Grid.

1.43 cm to the tip of the rod cathode, follows another set of 11 cells of identical values but reverse order compared to those at the hollow cathode tip. From that point,  $Z = 25.22$  cm, up to the right-hand boundary of the computational region at  $Z = 28.26$  cm. is an extension of the vacuum feed coaxial power transmission line to the rod diode. Since no particles will flow in that region, spatial resolution may be relaxed. Thus, over the next 1.12 cm, the axial grid size,  $\Delta Z$ , increases in the order; 0.10, 0.12, 0.14, 0.16, 0.18, 0.20, and 0.22 cm; in 7 cells. Finally, 8 cells of a constant  $\Delta Z = 0.24$  cm fill the remainder of the computational mesh. Thus, there are a total of 157 cells in the axial dimension. Adding a necessary monolayer of boundary cells in each dimension yields a net  $(158 \times 25 =)$  3950 grid points in the entire numerical model. To complete the numerical model of the CPA on this grid, the graphite hollow beam dump is represented by a perfectly absorbing, perfectly conducting solid, filling the cross-section from  $Z = 25.22$  to  $Z = 28.26$  cm and from  $R = 1.60$  to  $R = 2.40$  cm. It is considered to be electrically part of the cylindrical anode tube. Finally, the central rod cathode is approximated by a perfect conductor of radius, 0.32 cm, lying along the axis from  $Z = 25.22$  to  $Z = 28.26$  cm. The model device which emerges is drawn to scale in Figure 3.

Having established the number of computational cells, an estimate can be made of the number of particles needed in the typical simulation. If the two beams are roughly confined to only the high-resolution radial regions, they will normally be restricted to a maximum of  $(6 + 8) \times 143 =$  2002 cells. Requiring, for numerical noise prevention, about 10 to 20 macroelectrons per cell yields a goal of 20,000 to 40,000 particles in each simulation where both beams are present. These electrons are emitted onto the grid from the radial faces of the two cathodes according to MAGIC's Gaussian emission algorithm. At the onset of a run, the mesh is devoid of particles. Immediately, the hollow cathode is "turned on" through the imposition of a short-rise time potential pulse of -1.5 MV compared with the 0.0 volts of the "grounded" anode drift tube. The shape

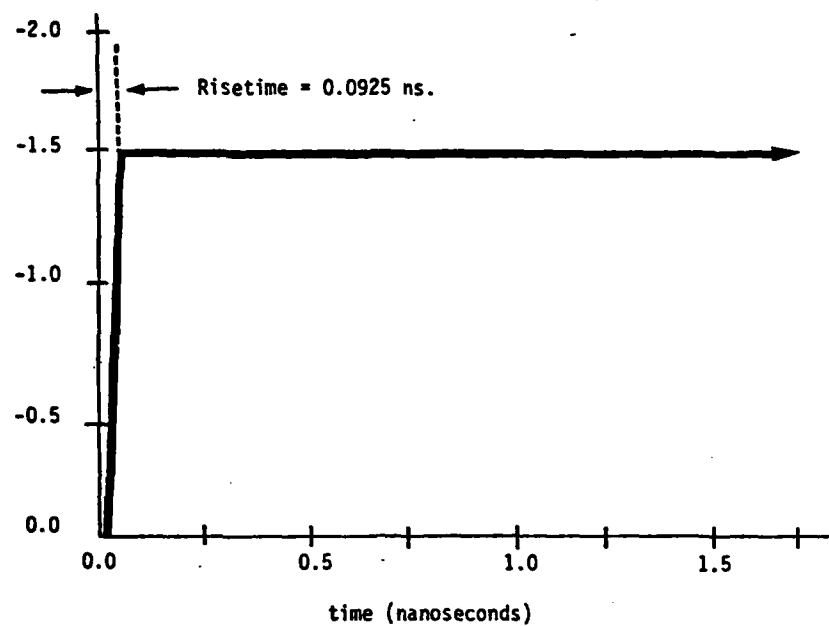




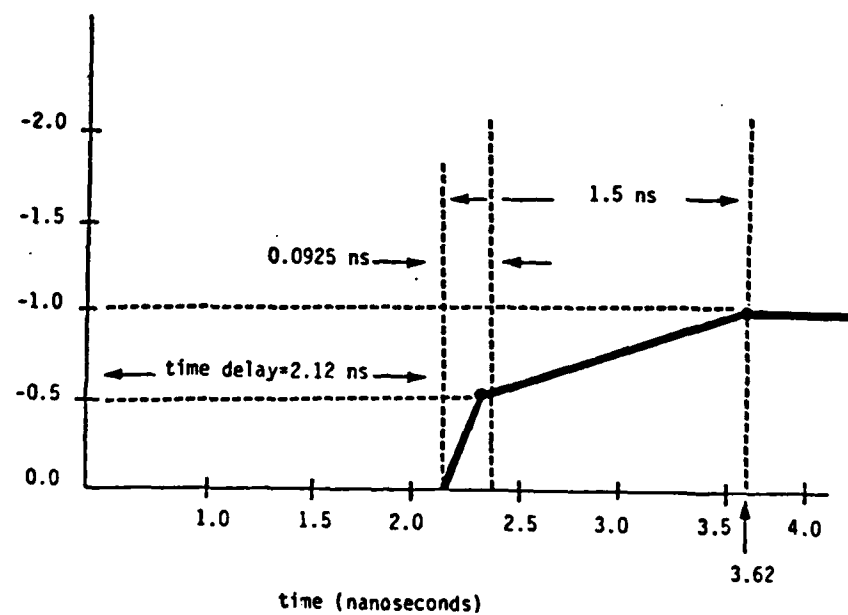
I 1.0 cm.

Figure 3. Scale Drawing of The Numerical Model.

of this pulse is shown in Figure 4a. The hollow beam requires at least 0.805 nanosecond to cross to the "graphite" beam stop at the other end of the tube. To give the hollow beam time to equilibrate, 2.12 ns (just over 1500 time steps) are allowed to pass before a voltage pulse is applied to the rod cathode. In the NRL experiments, the voltage was ramped from 0 to -1.0 MV on the rod cathode over about 5 nanoseconds. For computational efficiency, this pulse was ramped in two linear stages to -1.0 MV over 1.5 nanoseconds. This second pulse is depicted in Figure 4b. There is first a rapid (0.0925 ns) rise to -0.5MV, followed by a more gradual escalation to the full -1.0MV potential. Thereafter another 1.0 nanosecond is necessary for the 1.0 MeV electrons to cross the tube. This yields a total run time of about 4.5 nanoseconds or 3215 timesteps of  $\Delta t = 1.40 \times 10^{-12}$  second each for a complete simulation with both beams present.



(a) Hollow Cathode Voltage.



(b) Rod Cathode Voltage.

Figure 4. Voltage Pulses Applied in the CPA Simulations.

#### 4. THE MAGIC SIMULATION CODE

MAGIC (MAGnetic Insulation Code) is a computer code designed to simulate self-consistent (nonlinear) processes typically associated with pulsed power systems. Examples include power transport, beam propagation, magnetic insulation, diode operation, microwave tube design, etc. MAGIC is an intermediate size code (about 20,000 statements), and is highly optimized both for user efficiency and computational efficiency. It was developed by MRC under contract to Sandia National Laboratories for use in their light ion and electron fusion program. MAGIC is now entering the fifth year of development as a production code. There is an active user group, supported by an extensive User's Manual and active consultation with the authors. The code is available on Cyber 176, CRAY-1, and VAX-780 computers. The code has been documented extensively (References 4-6) and many results have been published (e.g., References 7-9); the discussion which follows will deal with the code's options and features which are crucial to successful simulation of relativistic electron beam devices.

Conducting surfaces can be imposed arbitrarily to exactly duplicate structural geometry in any of four coordinate systems (cartesian, cylindrical R-Z, cylindrical R- $\theta$ , and spherical). Periodic and mirror symmetry conditions, which apply to both fields and particles, can be imposed on the ends of a computational region. MAGIC has the capability of linking one-dimensional transmission lines to the two-dimensional simulation; this provides the means to model the interior structure of devices, which are plasma free. Such lines can be truncated with a "lookback" model which allows reflected waves to escape from the system.

Externally applied (static) magnetic fields can be imposed in any direction and can be a function of the spatial coordinates. (The dynamic magnetic field adds linearly to the static field to affect particle motion.) The functional form of electric fields from a static voltage can be determined initially from the solution of Poisson's equation. These

fields can be imposed by means of an external circuit to represent a power pulse propagating in the third dimension. Either the steady-state or the time dependent case can be represented. In either case, the dynamic fields again add linearly to the static fields to affect particle motion.

The emission of electrons or ions can be simulated over arbitrary predetermined conductor surfaces by application of Poisson's equation to surface cells, i.e., cells immediately adjacent to the electrode surface. The external normal electric field and charge existing within the cell are used to determine the surface normal field. To obey Child-Langmuir physics, this field should vanish. In MAGIC, enough charge is created near the surface to force this field to vanish (if the field has the wrong sign, no charge is created). This charge is normally broken up into a small number of macroparticles, which are then distributed randomly along the cell surface. A small spatial distribution in the normal direction provides effective temporal separation. The surface force algorithm is also altered to take actual surface charge into account.

This very simple model has seen effective use in a variety of applications. It has been validated by comparison with one-dimensional Child-Langmuir analysis. The primary requirement to achieve accuracy is fine normal spacing near the surface, and this is easily attained in MAGIC using the nonuniform spacing option. Finally, MAGIC has the capability to simultaneously model up to 10 particle species, which may be useful if positive ions are believed to play any role.

Two standard explicit (centered-difference and time-symmetric) and one novel implicit (time-biased) electromagnetic field solving algorithms are available as user options in the code. Particular mention should be made of the implicit solver since this is the one actually employed in these simulations. The basic idea behind this algorithm is very similar to the notion behind predictor-corrector. That is, spatial gradients of a magnetic field at several points in time are used to estimate the time

rate of change of the electric field. If these several points in time include advanced (unknown) magnetic fields, then the algorithm is implicit. In MAGIC, the implicit equations are solved by repetition for a single time step, making use of relaxation coefficients to improve convergence. This algorithm was originally developed by B. Godfrey of MRC (Reference 10), and has been extensively tested by use (e.g., Reference 6) in applications involving magnetic insulation.

The primary advantages of the time-biased over standard centered difference methods are that (1) high frequency noise is greatly reduced, (2) certain numerical instabilities are damped, and (3) the Courant criterion is usually relaxed. On this last point, the penalty of iterative solution outweighs the advantage of larger time steps. That is, the time-biased algorithm is always more expensive computationally. However, use of this algorithm (along with temporal filtering of magnetic forces) has virtually eliminated the debilitating wave trapping normally encountered in magnetic insulation type problems (see Reference 7 for a discussion of wave trapping).

Local charge conservation is another algorithm which is essential to a good representation of intense particle beam devices. The majority of PIC codes conserve charge only in the global sense - that is, system charge equals charge created minus charge destroyed. In many applications, the fluctuations in individual cell fields (due to various charge weighting schemes) are small compared with fields themselves. In such applications, the global conservation schemes are adequate. In beam-diode problems, however, the accumulated charge creation and destruction typically greatly exceed the system charge. In this case, the field fluctuations can exceed the magnitude of the fields themselves. This proceeds linearly with time in a simulation, culminating in obviously catastrophic results.

This effect is eliminated if charge conservation is ensured locally (cell-by-cell). There are several approaches possible to achieve this.

For example, some electromagnetic PIC codes periodically during the simulation (say, every 50 time steps) will solve Poisson's equation, and use the results to "correct" the local conservation directly through the current density algorithm. By contrast, MAGIC relies on consideration of multiple, orthogonal motions of particles and exact enforcement of the continuity equation in the direction of motion. Thus, local conservation is provided automatically by the current density algorithm in MAGIC, eliminating the need for subsequent, periodic "corrections".

MAGIC has been used to simulate too many devices to conveniently list them all here. Still, it is useful to mention several examples which illustrate the power and feasibility of the code. The first is explained in Reference 11. MAGIC was there used to simulate the effect on electron beam transmission of adding a dielectric liner to the cylindrical outer wall of an experimental drift tube cavity. The second example relates to an extensive series of foilless diode simulations conducted with MAGIC by Sandia National Laboratories (Reference 12). Some 22,000 macroelectrons were used in these runs which tested the effects of different values of an applied, uniform, axial magnetic field,  $B_0$ . The final example presented in Reference 13 looked at the problem of electron leakage in the NRL hybrid-inverted coaxial magnetron.

## 5. RESULTS

The primary results from this research effort were derived from five separate sets of MAGIC simulations conducted on the NRL VAX-11/780 computer. As detailed in the following five subsections, each simulation shed light on different aspects of the experimental device being modeled. They represent a logical progression of added insight. As new data emerged from each run, minor changes were made to the original, numerical model and new diagnostic output was requested. The starting point of the effort was a simulation of the full device as shown in Figure 2 with voltage pulses applied as shown in Figure 4 but with no particle emission. Then the simulation was rerun with only the hollow cathode pulse applied, allowing particle emission there, to test the formation of the outer hollow beam. In the next case, both pulses were applied again and both cathodes were allowed to emit. This was the first test of the dual beam configuration and it appeared to confirm previous experimental results. To gain additional physical information, the central beam was then tested without the hollow beam present. Finally, the dual beam case was rerun, this time using a shortened voltage pulse time history for the rod cathode. The major conclusions to be drawn from all of these runs are summarized in Section 6.

**5.1 "Cold Test" of the CPA.** A useful first test of the CPA configuration being modeled was a simple "cold test" of the device. This involved imposing the desired voltage pulses (see Figure 4) on the respective, opposing diode ports while not allowing any particle emission from the two cathodes. This showed how the two initially pure TEM waveforms combine in the cavity and illustrated the nature of the net electric fields down the entire length of the source-free tube.

At the start of the simulation, a voltage of  $1.5 \times 10^6$  volts was applied with a rise-time of less than 0.1 ns across the entrance port to the hollow cathode from its power transmission line. This was introduced as a pure TEM wave at that numerical boundary with a radially graded



electric field of about  $(1.5 \times 10^6)/(0.38 \times 10^{-2}) = -3.95 \times 10^8$  volts per meter. At this point in the presentation, a certain feature of the MAGIC code's treatment of boundary conditions should be explained. The same input data prescription that allows the imposition of the TEM wave along the specified numerical boundary segment also ensures the absorption of any TEM waves incident on that surface. This eliminates unwanted reflections of waves from that boundary as long as the incident wave is purely TEM. To guarantee that as closely as possible, the axial lengths of each of the two transmission line entrance port regions in the numerical model should be much greater than the respective radial separations between the coaxial conductors in those lines. For the hollow cathode port, the axial length is 1.08 cm (see Figure 2) compared to the radial gap of 0.38 cm, thus yielding a comfortable ratio of better than 2.8:1. For the rod cathode inlet, the corresponding lengths for this first simulation were 2.56 cm compared to 1.28 cm or a ratio of exactly 2:1 which was not quite as comfortable.

After the passage of 500 time steps of  $1.4 \times 10^{-12}$  second each, the wave front had traveled about 21 cm down the tube and, thus, had almost reached the opposing diode structure. It was decided to sample the electric field structure in the tube at that time. Figure 5 displays a MAGIC "LOGPRINT" map of the radial electric field component value at every data point in the mesh. A word of explanation regarding the plot is in order. The upper half of the figure represents that half of the device closer to the rod diode and the lower half represents the half closer to the hollow cathode, respectively. In each half, the lower margin consists of a column of 1- to 3-digit numbers above which is a blank column. That blank column corresponds to the tube centerline. The 1- to 3- digit numbers immediately below it are the axial data cell position numbers (see Figure 2). The left margin of the upper half of the figure consists of two vertical columns. The first is the "tens" digit and the second is the "units" digit of the radial data cell position numbers. In the overall map, the silhouettes of the two cathodes and the anode beam stop are clearly visible. Note, however, that their respective left-to-right

100-42751-21642751-22

94950	4444477777777777	5
94951	4444444447777777	6
94952	4444444447777777	7
94953	4444444447777777	8
94954	4444444447777777	9
94955	9999999997777777	0
94956	9999999997777777	1
94957	9999999997777777	2
94958	9999999997777777	3
94959	9999999997777777	4
94960	9999999997777777	5
94961	9999999997777777	6
94962	9999999997777777	7
94963	9999999997777777	8
94964	9999999997777777	9
94965	9999999997777777	0
94966	9999999997777777	1
94967	9999999997777777	2
94968	9999999997777777	3
94969	9999999997777777	4
94970	9999999997777777	5
94971	9999999997777777	6
94972	9999999997777777	7
94973	9999999997777777	8
94974	9999999997777777	9
94975	9999999997777777	0
94976	9999999997777777	1
94977	9999999997777777	2
94978	9999999997777777	3
94979	9999999997777777	4
94980	9999999997777777	5
94981	9999999997777777	6
94982	9999999997777777	7
94983	9999999997777777	8
94984	9999999997777777	9
94985	9999999997777777	0
94986	9999999997777777	1
94987	9999999997777777	2
94988	9999999997777777	3
94989	9999999997777777	4
94990	9999999997777777	5
94991	9999999997777777	6
94992	9999999997777777	7
94993	9999999997777777	8
94994	9999999997777777	9
94995	9999999997777777	0
94996	9999999997777777	1
94997	9999999997777777	2
94998	9999999997777777	3
94999	9999999997777777	4
95000	9999999997777777	5
95001	9999999997777777	6
95002	9999999997777777	7
95003	9999999997777777	8
95004	9999999997777777	9
95005	9999999997777777	0
95006	9999999997777777	1
95007	9999999997777777	2
95008	9999999997777777	3
95009	9999999997777777	4
95010	9999999997777777	5
95011	9999999997777777	6
95012	9999999997777777	7
95013	9999999997777777	8
95014	9999999997777777	9
95015	9999999997777777	0
95016	9999999997777777	1
95017	9999999997777777	2
95018	9999999997777777	3
95019	9999999997777777	4
95020	9999999997777777	5
95021	9999999997777777	6
95022	9999999997777777	7
95023	9999999997777777	8
95024	9999999997777777	9
95025	9999999997777777	0
95026	9999999997777777	1
95027	9999999997777777	2
95028	9999999997777777	3
95029	9999999997777777	4
95030	9999999997777777	5
95031	9999999997777777	6
95032	9999999997777777	7
95033	9999999997777777	8
95034	9999999997777777	9
95035	9999999997777777	0
95036	9999999997777777	1
95037	9999999997777777	2
95038	9999999997777777	3
95039	9999999997777777	4
95040	9999999997777777	5
95041	9999999997777777	6
95042	9999999997777777	7
95043	9999999997777777	8
95044	9999999997777777	9
95045	9999999997777777	0
95046	9999999997777777	1
95047	99	

**Figure 5.  $E_r$  at  $t = 500\Delta t$  for "Cold Test" Case.**

positions have been reversed compared to the cross section portrayed in Figure 2. The numbers which appear at each data point in Figure 5 represent the order-of-magnitude (power of ten) of the respective value of  $E_r$  (in volts per meter) with a scale factor of 1. Minus signs are overprinted on any negative value of  $E_r$  on the mesh. Stand alone minus signs indicate unprintably small negative values. The applied radial electric field values of order  $10^8$  V/m are clearly present at the hollow cathode power input port. The field strengths drop off, as expected, when one scans leftward toward the wave front. The traveling front is clearly outlined at around  $z = 132$ . The corresponding "LOGPRINT" map for the axial component of the electric field at the same instant in time is shown in Figure 6. Note that  $E_z$  is everywhere negative as expected.

Since it was not necessary in this "cold test" to worry about a hollow electron beam being formed and then reaching equilibrium, the turn-on of the rod cathode voltage pulse was advanced from the  $t = 2.12$  ns shown in Figure 4 to  $t = 1.5$  ns instead. The shape of the pulse itself, however, was kept the same. By  $t = 3.5$  ns (i.e.,  $t = 2500 \Delta t$ ), an approximate equilibrium of the fields in the device should have been approached. Figures 7 and 8 show the "LOGPRINTs" of the radial and axial electric field components, respectively at that time. Some minor, low magnitude ripples are still apparent in the  $E_r$  map but that for  $E_z$  is much smoother. The axial field is predominantly negative from the hollow cathode all the way out to about  $z = 90$  with the remainder turned positive due to the opposing rod cathode voltage pulse. The field strengths are particularly high near the tips of the cathodes as expected due to two-dimensional field enhancement effects (Reference 14). It can further be seen that  $E_z$  along the hollow cathode power input boundary is on the order of  $10^4$  V/m compared to  $E_r$  values of  $10^8$  there. This implies an almost perfect TEM field structure there which, in turn, guarantees almost no false reflections there. The situation is not quite so favorable along the rod cathode power inlet at the opposite end of the tube. There,  $E_z$  is on the order of  $10^5$ - $10^6$  V/m while  $E_r$  is like  $10^7$ - $10^8$  V/m. Thus, less than two orders of magnitude separate the two components there.



[illegible]

12710, 0202020, 020102

[illegible]

Figure 7.  $E_r$  at  $t = 2500 \Delta t$  for "Cold Test" Case.

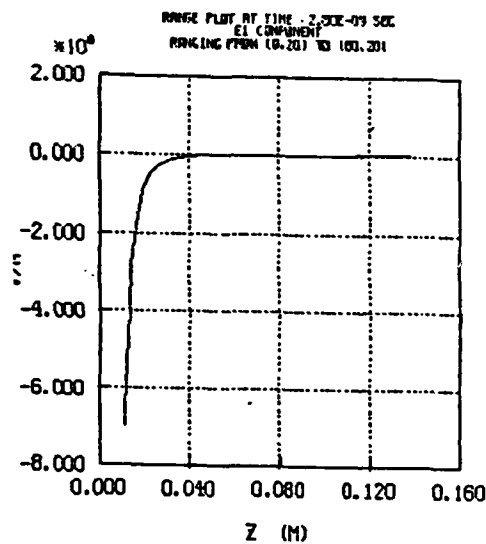


implying deviations from a pure TEM waveform of at least several percent. Some low-order but noticeable reflections should take place there. More on that later.

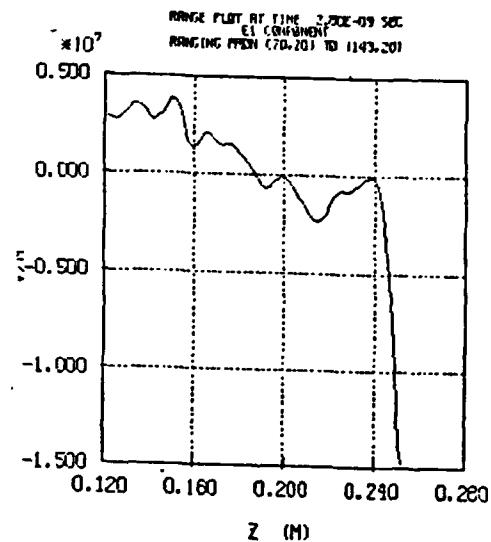
The next important diagnostic output from this run consisted of axial profiles of the electric field components along the paths which would be traveled by the two electron beams. These profiles are plotted in Figure 9. The upper two profiles, taken in combination, plot  $E_z$  (in V/m) versus  $z$  (in meters) across the full length of the device for a constant tube radius of  $r = 1.94$  cm, which should be about 0.08 cm less than the average outer radius of the hollow electron beam. Note that the field strength scales of the two plots are different; the left one runs from  $-8 \times 10^8$  to  $2 \times 10^8$  V/m while the right has values only from  $-1.5 \times 10^7$  to  $0.5 \times 10^7$  V/m. The plots show a strong, negative  $E_z$  over the first 2 cm out from the hollow cathode tip with a complimentary 2 cm length of enhanced  $E_z$  at the opposite end of the tube, just before the anode beam stop. The peak magnitude of  $E_z$  at that far end is down by a factor of about 50 from that near the cathode. These plots show in much stronger terms than Figure 8, that  $E_z$  is effectively negligible over most of the tube's length except at the ends.

The bottom two plots of Figure 9 give the axial profiles of  $E_r$  (left) and  $E_z$  (right) over most of the tube's length at a constant radius  $r = 0.24$  cm which is about 0.08 cm inside the expected outer radius of the central electron beam envelope. The radial field component plot is quite unremarkable. The strong  $E_r$  near the tip of the rod cathode can be expected to impart a significant radial momentum component to the motion of electrons emitted there but this is to be expected for both beams. More significant is the profile for  $E_z$  at this radius. Near the rod cathode tip, a strong, positive  $E_z$  will accelerate the electrons down the tube centerline but at the opposite end of the tube, a region of strong  $E_z$  of opposite sign is encountered. There, the central beam electrons will be decelerated. This is to be expected since the hollow

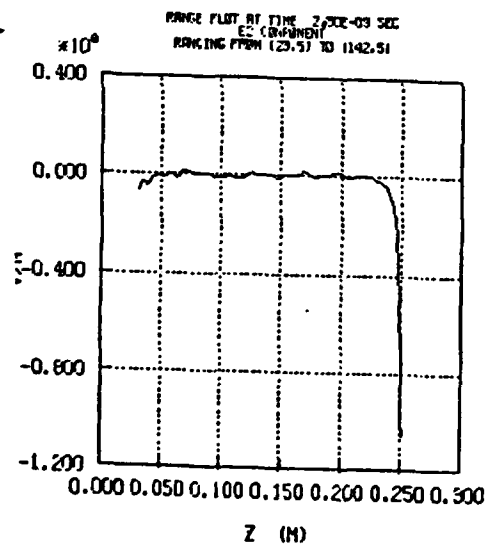
MAGIC VERSION JUNE 1983 DATE 6/17/83  
SIMULATION NAL COLLECTIVE PARTICLE ACCELERATOR



MAGIC VERSION JUNE 1983 DATE 6/17/83  
SIMULATION NAL COLLECTIVE PARTICLE ACCELERATOR



MAGIC VERSION JUNE 1983 DATE 6/17/83  
SIMULATION NAL COLLECTIVE PARTICLE ACCELERATOR



MAGIC VERSION JUNE 1983 DATE 6/17/83  
SIMULATION NAL COLLECTIVE PARTICLE ACCELERATOR

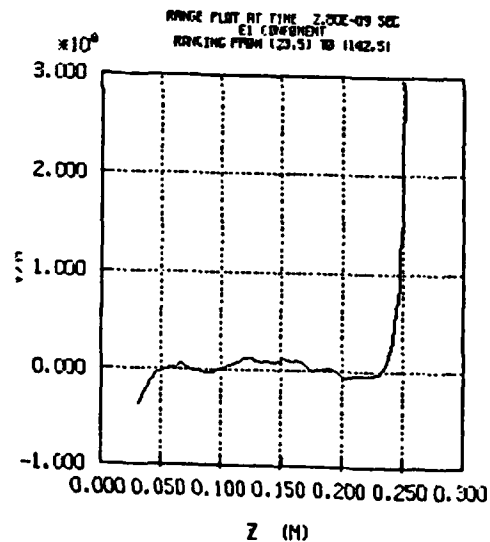


Figure 9. Axial profiles of  $E_z$  at  $R = .20$  (top two)  
 $E_z$  at  $R = 5$  (bottom right) and  $E_r$  at  
 $R = 5$  (bottom left).

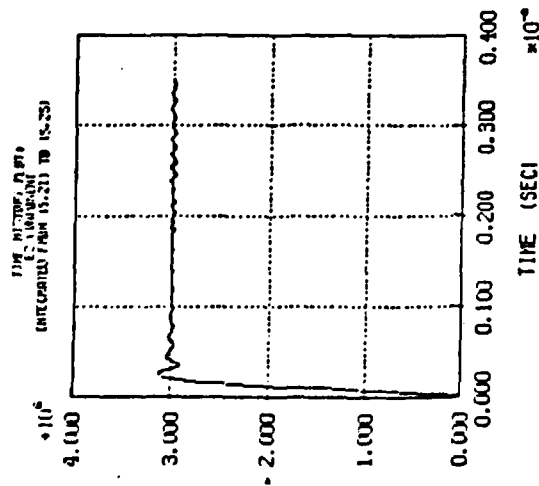


cathode is at -1.5MV while the rod cathode is at only -1.0MV. In the actual experiment, the tube length of over 5 meters makes electron reflection from such a reversed field region ignorable when considering early time ( $\leq 10$  ns) results since the central electrons will require at least 15 ns just to travel once to the region of the hollow cathode. In these simulations, however, the shorter tube length of only 25 cm requires that care be taken to sort out this reflecting electron effect from the gross behavior of the central beam. That question is addressed further in subsections 5.3, 5.4, and 5.5.

The final major diagnostic output from the code run consisted of the three time history plots shown in Figure 10. Examining them from left to right, the first presents the temporal shape of the actual voltage measured radially between the hollow cathode and the anode tube. The TEM wave applied at the power pulse inlet boundary was only 1.5MV (peak). The non-emitting hollow cathode tip, however, represents an infinite impedance mismatch in the coaxial feed line and therefore reflects the input wave and doubles the resultant hollow cathode-to-anode peak voltage to 3.0MV. It is this voltage that would be measured experimentally. If the hollow cathode emits electrons, that changes the impedance mismatch which changes the wave reflection coefficient which changes the measured voltage. With the hollow beam present, this was experimentally measured to be 1.5MV. Therefore, the voltage applied to that boundary in the simulation must be adjusted downwards until it yields a net measured electrode voltage of 1.5MV. This was, in fact, done as additional simulations were accomplished.

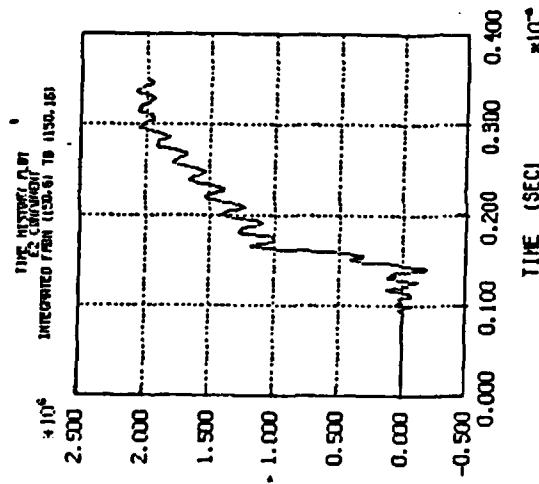
The next plot in Figure 10 is the corresponding measured voltage pulse on the rod cathode with respect to the anode (specifically, the anode beam dump). Comparing this and the previous one to their ideal, applied, numerical counterparts as shown in Figure 4, demonstrates a very close correspondence. The hollow cathode pulse is nearly identical. The rod cathode pulse (ignoring the previously mentioned turn-on time advance)

MSIC VERSION JUNE 1983 DATE 8/17/83  
SIMULATION FOR COLLECTIVE PARTICLE RECELERATION



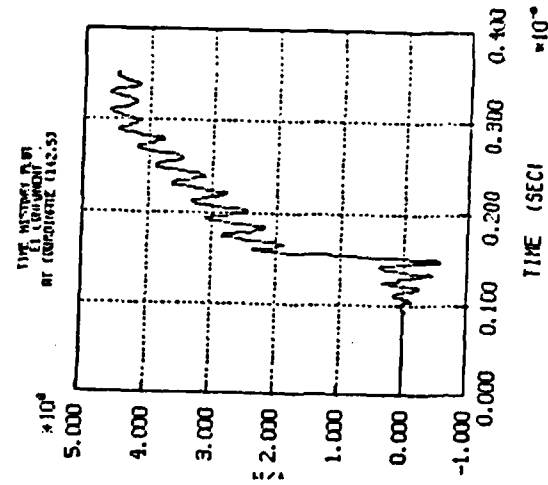
(a)

MSIC VERSION JUNE 1983 DATE 8/17/83  
SIMULATION FOR COLLECTIVE PARTICLE RECELERATION



(b)

MSIC VERSION JUNE 1983 DATE 8/17/83  
SIMULATION FOR COLLECTIVE PARTICLE RECELERATION



(c)

Figure 10. Time Histories of (a) Voltage on Hollow Cathode, (b) Voltage on Rod Cathode, and (c)  $E_z$  at Tip of Rod Cathode.

also has good shape fidelity except for the 2-5% ripples which appear to be due to minor reflections of waves hitting the rod cathode power inlet boundary. (It was already stated that the non-TEM components will be reflected there.) To help reduce these ripples, the axial length of the coaxial power inlet in the model was subsequently lengthened by the addition of two axial cell columns of  $\Delta Z = 0.24$  cm. That addition brings the total axial cell count up from 156 to 158 cells, giving a total of 3950 data cells covering the entire numerical mesh.

The final plot in Figure 10 simply presents the time history of the magnitude of  $E_z$  (in volts/meter) measured just opposite the tip of the rod cathode. It faithfully reproduces the temporal shape of the rod cathode voltage pulse. No interference from the opposing cathode voltage pulse is obvious from this plot. Without charged particles present to strongly couple them, the two pulses from either end of the accelerator tube seem fairly independent. No threat to the successful operation of this device can yet be observed. The next step in these studies involved the "turning on" of emission from the hollow cathode tip alone and examining the formation of the hollow electron beam. In the CPA experiments at NRL, no difficulties were ever experienced with propagating a hollow beam of some 30 kA down the full length of the five meter tube whether or not the central beam was present.

5.2 Hollow Beam Only. Having tested the pure electromagnetic response of the CPA model, the next step involved the inclusion of charged particles in the simulations. In the CPA experiments, it was observed that the hollow, high current, electron beam would always faithfully propagate down the entire length of the tube. In this first numerical run with particles, it was decided to examine the formation of the hollow beam alone, without any voltage pulse being applied to the rod cathode and without electron emission being allowed there. For this simulation, a peak voltage, 1.5MV pulse was applied to the hollow cathode diode. The pulse shape was that shown in Figure 4a, with a rise time of slightly less

than 0.1 ns. Electron emission was permitted along the entire protruding front face of the hollow cathode. (Note that MAGIC uses a physically true, Gaussian emission algorithm which calculates how much charge should be emitted from a given surface at a given time step by sampling the local, normal electric field - see Section 4 of this report.) If the hollow cathode diode being modeled corresponded exactly to the physical device under study, it would be mandatory to include in the simulation electrons emitted from the cathode shank. Such shank emission has been shown to significantly effect the current characteristics of a diode (Reference 15). Such emission was not included here for the following reasons:

- a. The radial anode-cathode gap in the model is artificially small and would therefore give rise to an artificially large shank emission current.
- b. As long as the hollow beam is stable and remains within reasonable limits with regard to its total current, any finer details with regard to its microscopic characteristics are not of major importance to these simulations.
- c. The "turning on" of some length of the cathode shank to emission would require a lengthening of that coaxial, inlet port region in the numerical model in order to ensure accurate TEM wave power injection at that boundary. This would require the addition of extra cells to the numerical model which would increase computer run times. (The additional, numerical particles emitted from the shank would even more dramatically increase typical run times.)

After 500 time steps of  $\Delta t = 1.4 \times 10^{-12}$  second, a sample electron position plot was generated, as shown in Figure 11. Strong ripples are evident in the beam as is typical in foilless diode operation (Reference 16). It appears that substantial phase mixing of the ripples takes place by halfway down the tube. In viewing this figure, it is important to keep in mind the gross distortion of axial-to-radial scales. The total

MAGIC VERSION JUNE 1983 DATE 9/11/83  
SIMULATION NRL COLLECTIVE PARTICLE ACCELERATOR

TRAJECTORY PLOT OF ELECTRONS ( ISPE = 1 )  
AT TIME 7.00E-10 SEC FOR 1 TIME STEPS

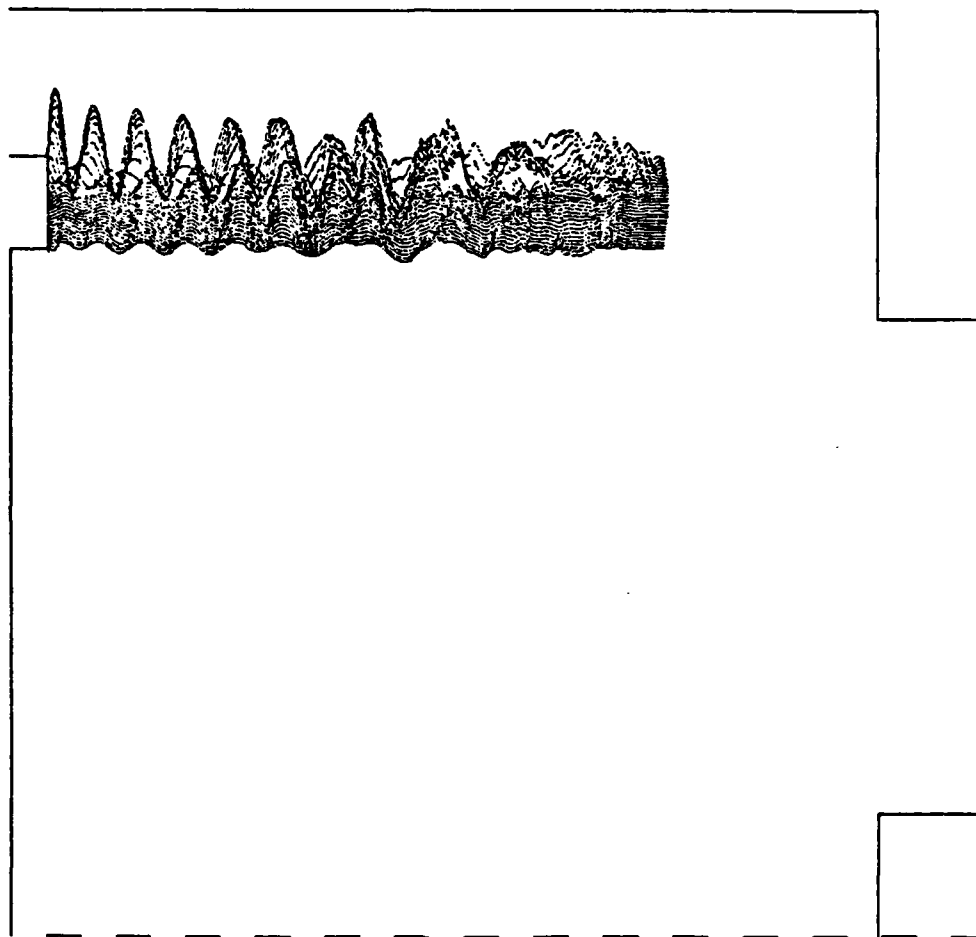


Figure 11. Particle Plot for Hollow Beam Case at  $t = 500\Delta t$ .

distance from the dashed centerline to the outer tube wall is actually only 2.4 cm while the distance from the hollow cathode tip to the axially-opposing anode beam stop is 24.14 cm. Thus axial dimensions are extremely compressed. This effect accentuates the amplitude of the ripples.

After another 500 time steps, the beam is fairly well established as can be seen from the sample position plot of Figure 12. The phase mixing of the ripples is even more pronounced here. Significant gaps between the particle streams near the cathode, however, indicate the advisability of increasing the total number of particles used to represent the beam. An increased number density should also result in decreased choppiness of the downstream portion of the beam. In this simulation, the total, average particle count was about 19,000. The field characteristics of this single beam model were likewise diagnosed in detail.

The "LOGPRINTs" for both the radial and axial components of the electric field are displayed in Figures 13 and 14 respectively. The  $E_r$  plot shows the expected maintenance of a strong, uniform radial E-field between the beam and the anode wall. The corresponding  $E_z$  plot shows high field strength values concentrated at either end of the tube with low values in between. To help visualize what has happened to the E-field in the tube, it would be instructive to view an equipotential plot. However, MAGIC works only with  $E_r(z,r)$  and  $E_z(z,r)$ , not with  $\phi(z,r)$ . Nevertheless, parallel results are available from another foilless diode simulation the author has run (Reference 16) and these are shown in Figure 15. This simulation was run with the quasistatic DIODE2D code at the Naval Research Laboratory. The top part of the figure shows the numerical model and the bottom shows  $\phi(z,r)$  in the anode tube when a well-collimated hollow electron beam is propagating down the tube. Note that, as in the present simulation, electrons emitted from the cathode tip are first accelerated axially in a region of enhanced  $E_z$ . That first acceleration gradient does not impart the full diode voltage to them. For the example shown, only four 10% equipotential contours are crossed in that first region before electrons effectively enter a "drift" mode down most of the

MAGIC VERSION JUNE 1983 DATE 9/11/83  
SIMULATION NRL COLLECTIVE PARTICLE ACCELERATOR

TRAJECTORY PLOT OF ELECTRONS ( ISPE = 1 )  
AT TIME 1.40E-09 SEC FOR 1 TIME STEPS

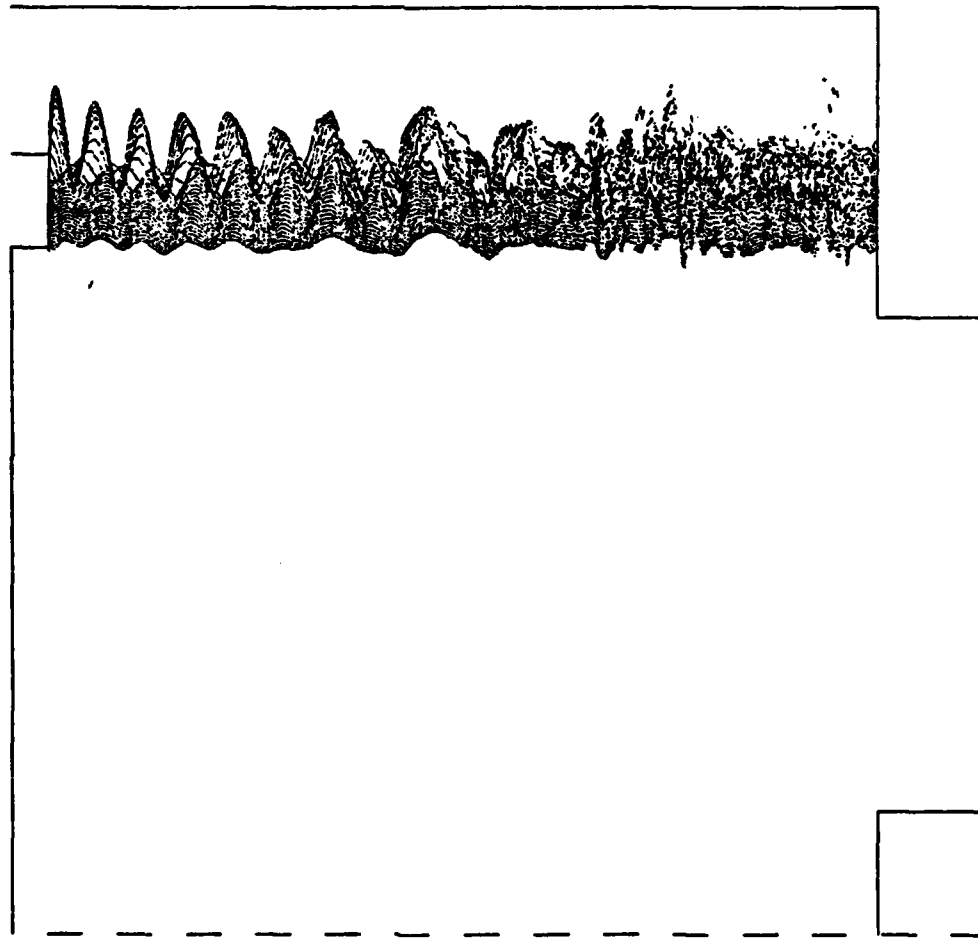


Figure 12. Particle Plot for Hollow Beam Case at  $t = 1000 \Delta t$ .







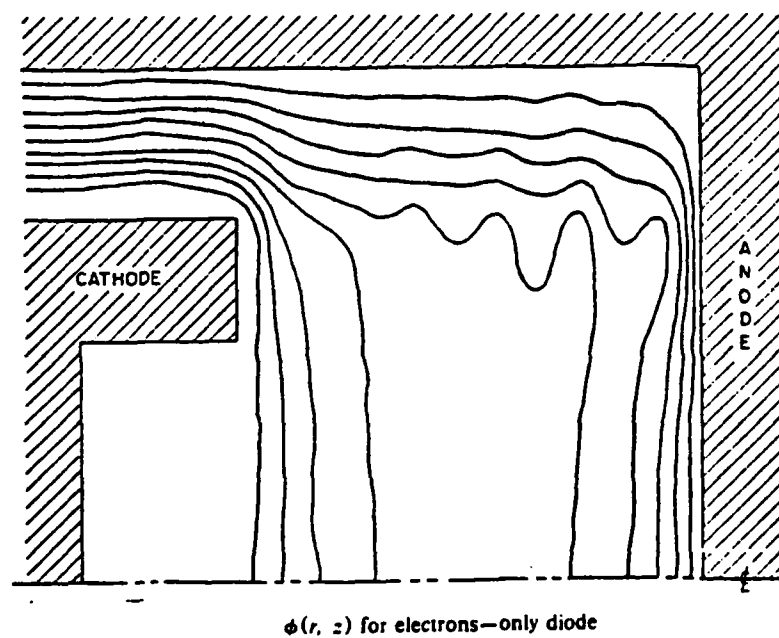
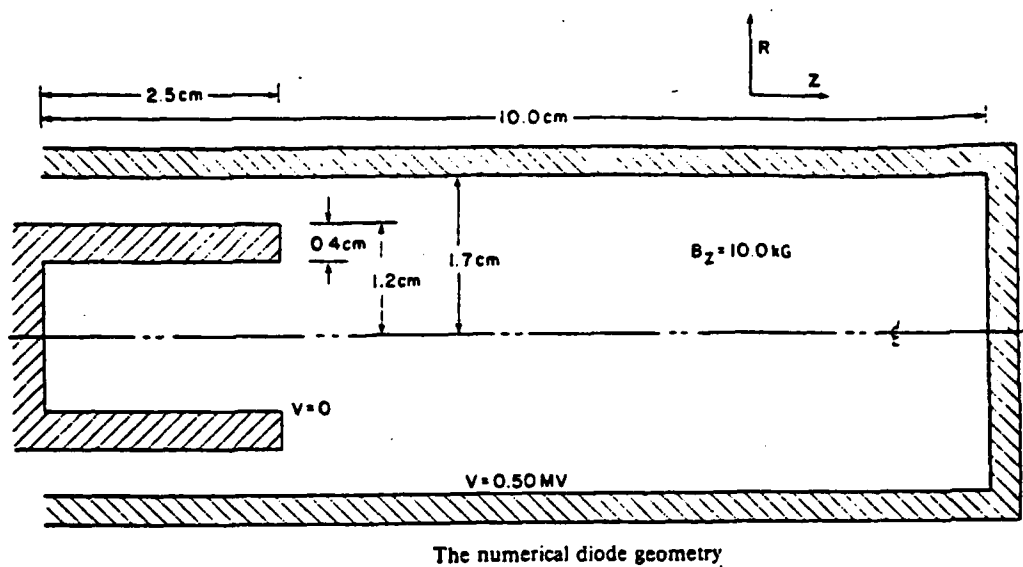


Figure 15. Equipotential Contours for a Typical Hollow Beam Foilless Diode (from Reference 16).

remaining length of the tube. Finally, just before impacting the anode end-plate, the electrons cross another region of enhanced  $E_z$  over which they are brought up to full diode energy. Notice that the regions of enhanced  $E_z$  at both ends of the beam extend radially inward with only slightly decreasing intensity. Carrying these qualitative results back to the present MAGIC simulation, implies that the presence of the intense, outer, hollow beam would create a region of enhanced  $E_z$  of the wrong sign at the tip of the rod cathode which would have to be overcome by the 1.0MV voltage pulse there for axial propagation of the central beam. This may be surmised as the major cause for the propagation problems encountered in the actual experiments and the remainder of these simulations give confirmation to that hypothesis.

In agreement with the above description for a typical electron acceleration history in the hollow beam are the axial profiles of  $E_z$  at  $r = 1.94$  cm (just inside the outer radius of the hollow beam) displayed in the top two plots of Figure 16. Large values of  $E_z$  are axially confined to narrow regions ( $\leq 2$  cm) immediately adjacent to the cathode tip (left) and the anode beam stop (right). The bottom two plots are the corresponding axial profile for the radial electric field at  $r = 1.94$  cm. They show nothing particularly remarkable and are included only for the sake of completeness. Much more significant is the axial profile of  $E_z$  at  $r = 0.24$  cm (just inside the future outer envelope of the central beam) shown in Figure 17. As could be predicted, a strong, negative  $E_z$  dominates the region near the rod cathode tip (right plot). The peak field there is  $-1.2\text{MV/cm}$ . That must be neutralized by the rod cathode voltage before electrons can even be emitted, let alone accelerated down the axis. In the opposite half of the device (left plot) at the same radius, Figure 17 shows two rather extended regions of significant negative  $E_z$  which would act to decelerate any central beam electron. The simulations in the following three sections will demonstrate how this field structure is modified by the presence of the central beam and how that beam is effected by the resultant fields.

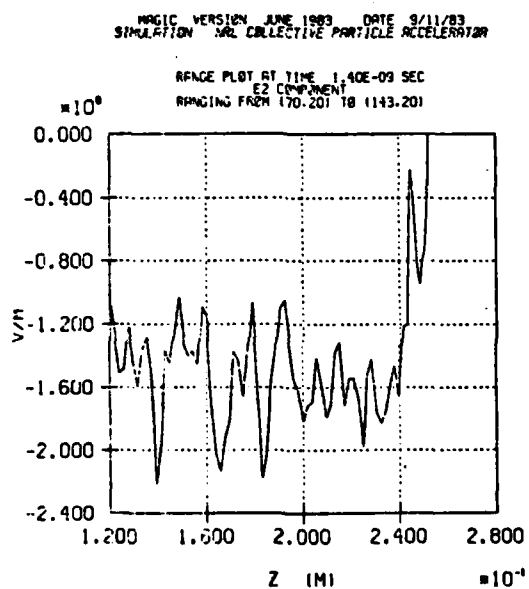
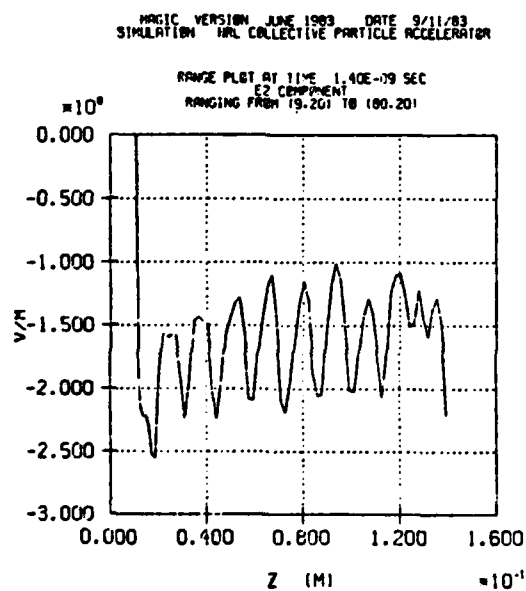
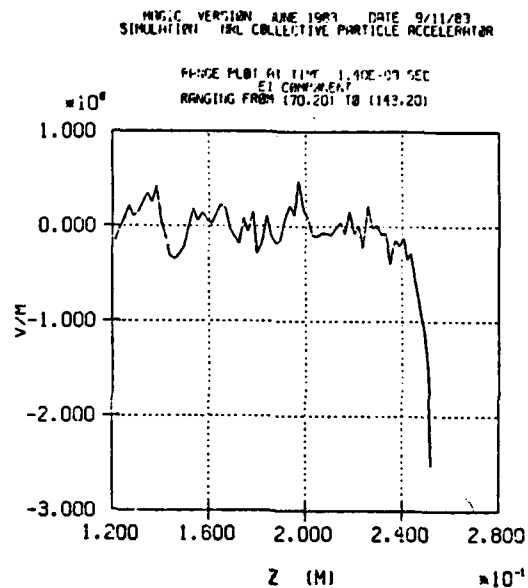
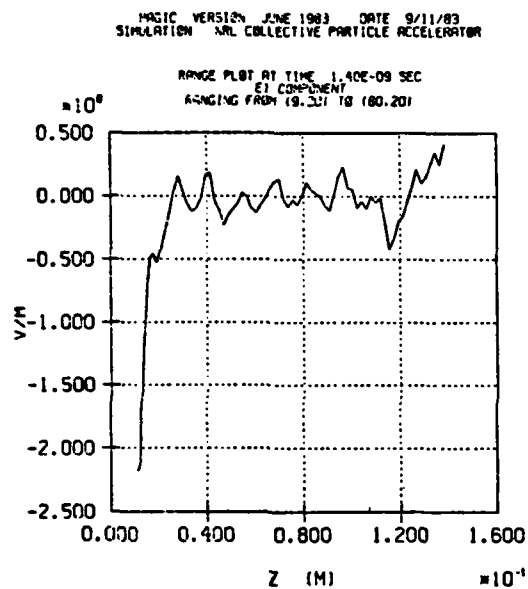
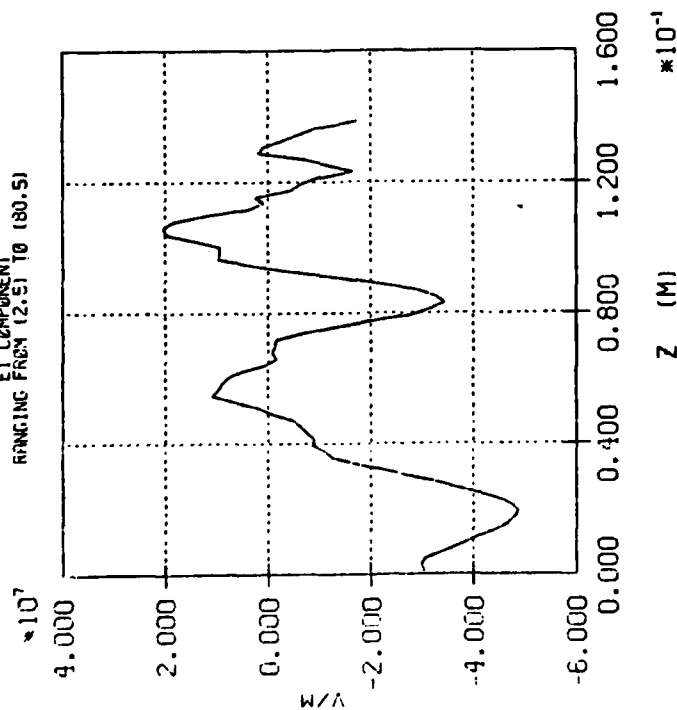


Figure 16. Axial Profiles of  $E_z$  (top) and  $E_r$  (bottom)  
at  $R = 1.94$  cm and  $t = 1000 \Delta t$  for Beam Case.

MAGIC VERSION JUNE 1983 DATE 9/11/83  
SIMULATION NRL COLLECTIVE PARTICLE ACCELERATOR

RANGE PLOT AT TIME 1.40E-09 SEC  
E1 COMPONENT  
RANGING FROM 12.51 TO 180.51



MAGIC VERSION JUNE 1983 DATE 9/11/83  
SIMULATION NRL COLLECTIVE PARTICLE ACCELERATOR

RANGE PLOT AT TIME 1.40E-09 SEC  
E1 COMPONENT  
RANGING FROM 170.51 TO 1143.51

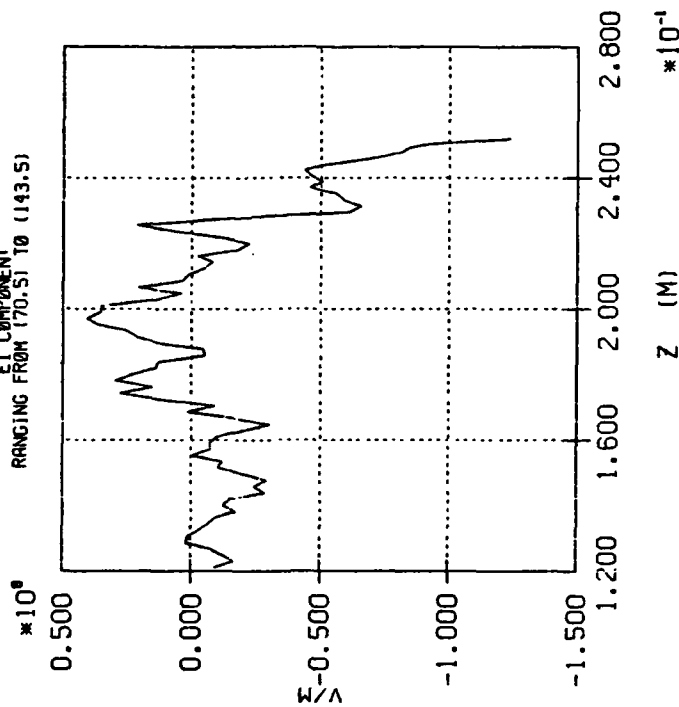


Figure 17. Axial Profile of  $E_z$  at  $R = 0.24$  cm and  $t = 1000 \Delta t$  for Hollow Beam Case.

The final set of diagnostics for this Hollow-Beam-Only case is presented in Figure 18. The upper left plot shows the measured time history of the voltage between the hollow cathode and the anode. Just as in the previous "cold test" simulation, a voltage of 1.5 MV is being applied at the inlet boundary but is then being augmented by the wave reflected from the impedance mismatch at the end of the cathode shank. With no hollow beam, the mismatch was virtually infinite, resulting in a voltage doubling. Now, with the hollow beam present, there is only a finite mismatch which boosts the measured peak voltage from the applied 1.5 MV to about 2.2 MV. Therefore, to agree with the experiment, the applied voltage must be lowered to about  $(1.5)(1.5)/2.2 = 1.0$  MV. That is the value used there in all of the following simulations. The upper right plot monitors the magnitude of the axial electric field component a distance of 0.04 cm axially away from the rod cathode tip. It shows the creation of a strong negative field there due to the presence of the hollow electron beam. This should inhibit the emission and/or propagation of an electron beam from that cathode. The bottom two plots of Figure 18 correspond to the  $B_\theta$  probe-type measurements such as those actually performed in the experiment (although the experimental probes displayed time-integrated results). The left plot traced the value of  $B_\theta$  at a radius of 2.345 cm and a distance 4.185 cm axially downstream from the hollow cathode tip. It shows a rapid leveling off of  $B_\theta$  to an average value of about -0.675 webers per meter<sup>2</sup> ( = -6.75 kilogauss). This translates to a beam current of about 79 kA which is more than a factor of two above that used in the experiments. Lowering the effective diode voltage from 2.2 MV to 1.5 MV in the remaining simulations lowered the hollow beam current to a more reasonable value. The lower right plot of Figure 18 traces  $B_\theta$  at the same radius but at an axial distance of 20.395 cm downstream from the cathode tip. It shows the beam time-of-flight delay and the leveling off to the same value of about -0.675 w/m<sup>2</sup>.

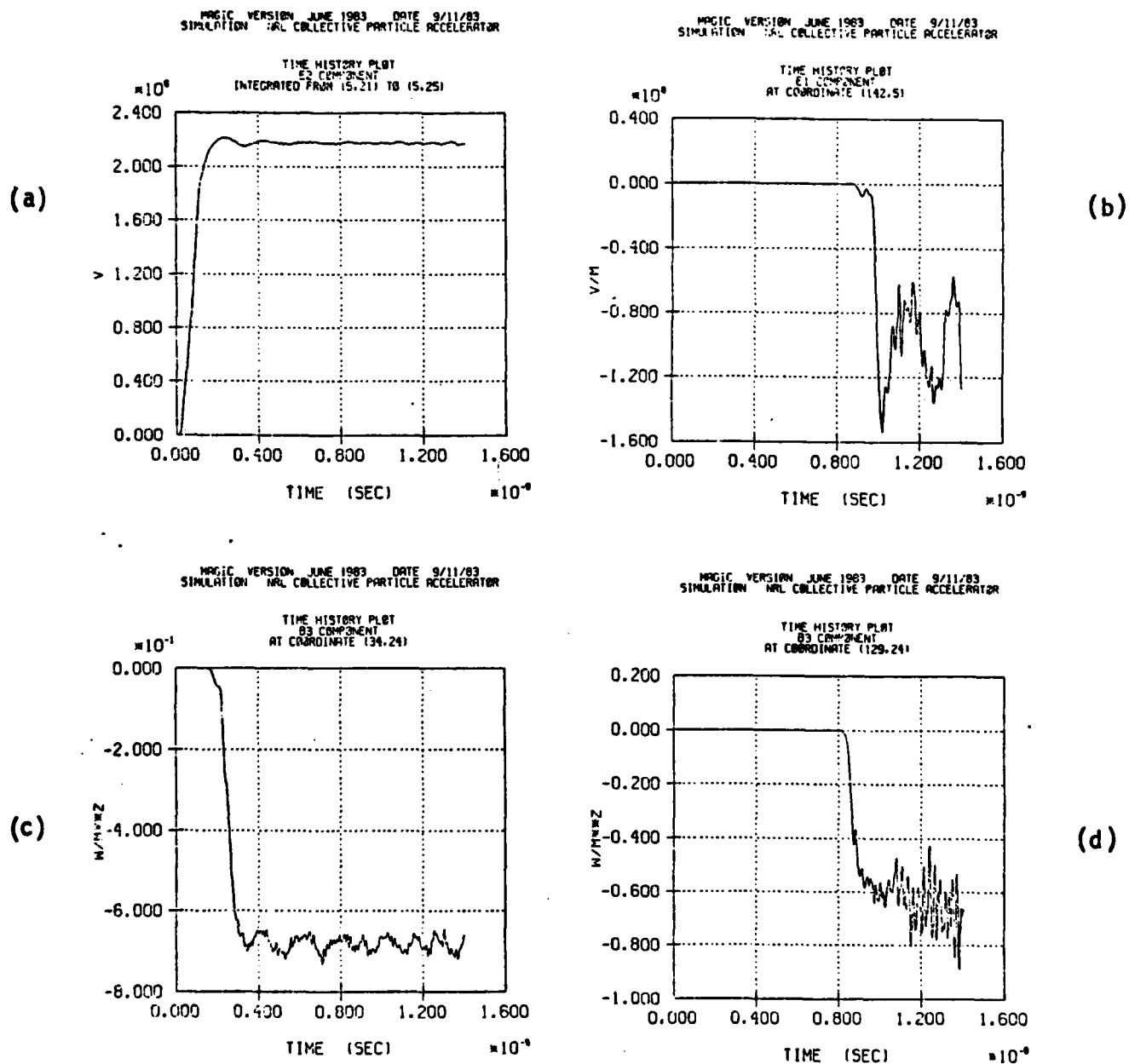


Figure 18. Hollow Beam Case Time Histories for (a) Hollow Cathode Voltage Pulse, (b)  $E_z$  at (142,5), (c)  $B_\theta$  at (34,24), and (d)  $B_\theta$  at (129,24)

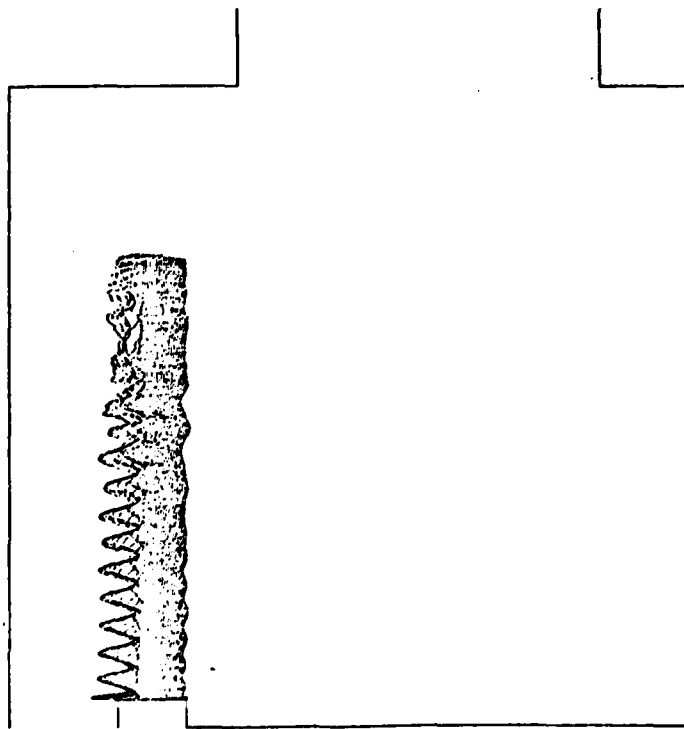
5.3 Dual Beam Case I. The next step in this simulation program was to test the dual beam operation of the CPA model with an appropriately adjusted hollow cathode voltage value and, thereby, a lowered hollow beam current. To accomplish this, the plateau value of the peak voltage in Figure 4a was lowered to 1.0MV. The corresponding peak voltage for the rod cathode (Figure 4b) was left as shown. Figures 19, 20, and 21 display six sample particle plots for the electrons of both beams at 0.7, 2.1, 2.8, 3.5, 4.2 and 4.9 nanoseconds. (The rod cathode voltage pulse began at 2.12 ns.) The peak simulation particle count for this run was about 35,000 macroparticles. The increased particle density significantly enhanced the smooth appearance of the equilibrium hollow beam. For the parameters chosen, these figures clearly demonstrate that the central beam does propagate across the entire CPA tube. That is qualitatively obvious. To quantify the nature of this propagation, more detailed diagnostics must be examined.

The first of these is the  $E_z$ -field LOGPRINT of Figure 22. Unlike the corresponding plots of Figures 5 and 6, the minus signs, which indicate negative field values, are not overprinted on the field magnitude number but rather are offset printed in a one-to-one map directly above the number plot. This makes the negative values a good deal easier to pick out. As in the previous case, the highest field values (7's and 8's) are most strongly concentrated at either end of the tube. For the hollow beam, there are intense negative  $E_z$  regions at the beginning and end while those for the central beam are appropriately positive and of smaller extent. Unlike the hollow beam, the central beam also hosts regions of 7-strength  $E_z$  fields located far from its end-points (e.g., - between  $Z = 38$  and  $Z = 57$  in Figure 22). What's more, these regions are of mixed sign which indicates some degree of significant beam deceleration.

The corresponding radial E-field LOGPRINT may be found in Figure 23. As could be expected, the field is almost everywhere negative and displays a strong uniformity in the axial dimension due to the axially uniform electron space charge distribution. Particularly noteworthy is the very



MAGIC VERSION JUNE 1983 DATE 9/18/83  
 SIMULATION NRL COLLECTIVE PARTICLE ACCELERATOR  
 TRAJECTORY PLOT OF ELECTRONS ( ISPE = 1 )  
 AT TIME 7.03E-10 SEC FOR 1 TIME STEPS



MAGIC VERSION JUNE 1983 DATE 9/19/83  
 SIMULATION NRL COLLECTIVE PARTICLE ACCELERATOR  
 TRAJECTORY PLOT OF ELECTRONS ( ISPE = 1 )  
 AT TIME 2.10E-09 SEC FOR 1 TIME STEPS

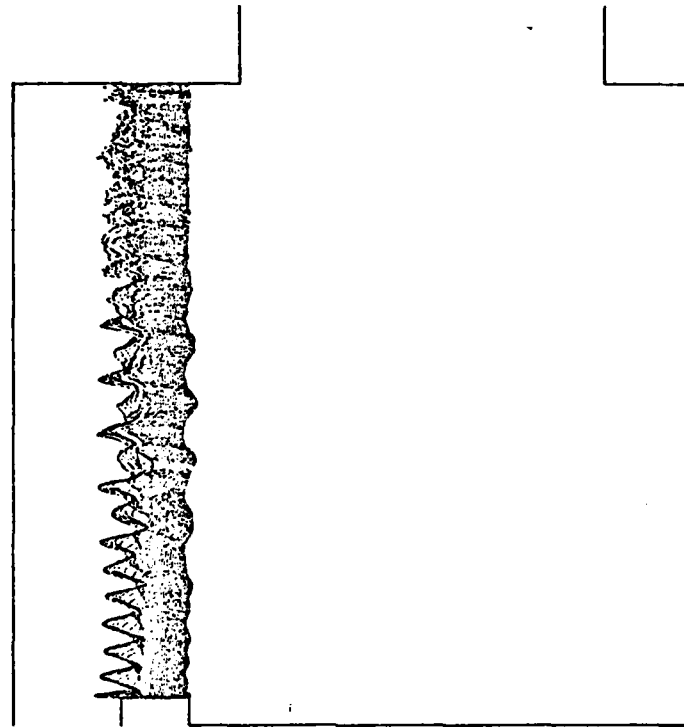
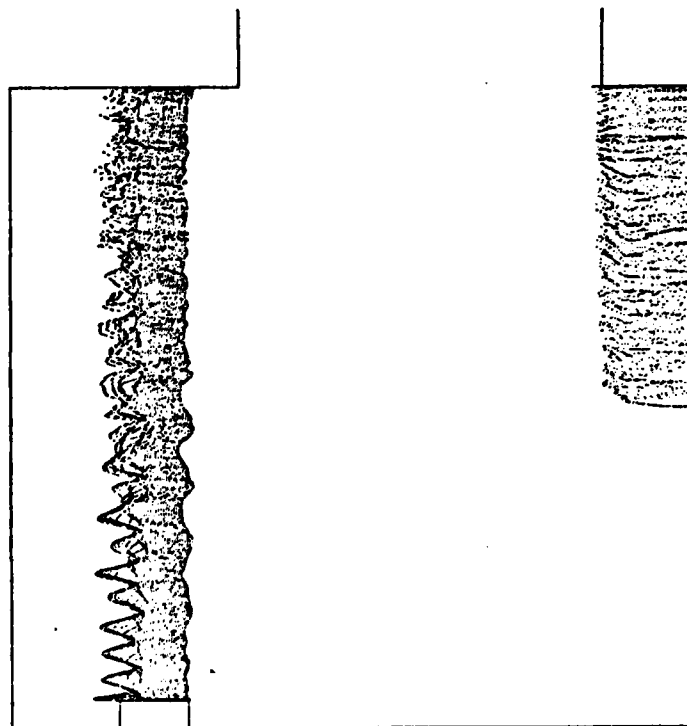


Figure 19. Hollow Beam at  $t = 500\Delta t$  and  $t = 1500\Delta t$  for Dual Beam Case I.

MAGIC VERSION JUNE 1983 DATE 9/20/83  
 SIMULATION NRL COLLECTIVE PARTICLE ACCELERATOR  
 TRAJECTORY PLOT OF ELECTRONS ( ISPE = 1 )  
 AT TIME 2.60E-09 SEC FOR 1 TIME STEPS



MAGIC VERSION JUNE 1983 DATE 9/20/83  
 SIMULATION NRL COLLECTIVE PARTICLE ACCELERATOR  
 TRAJECTORY PLOT OF ELECTRONS ( ISPE = 1 )  
 AT TIME 3.50E-09 SEC FOR 1 TIME STEPS

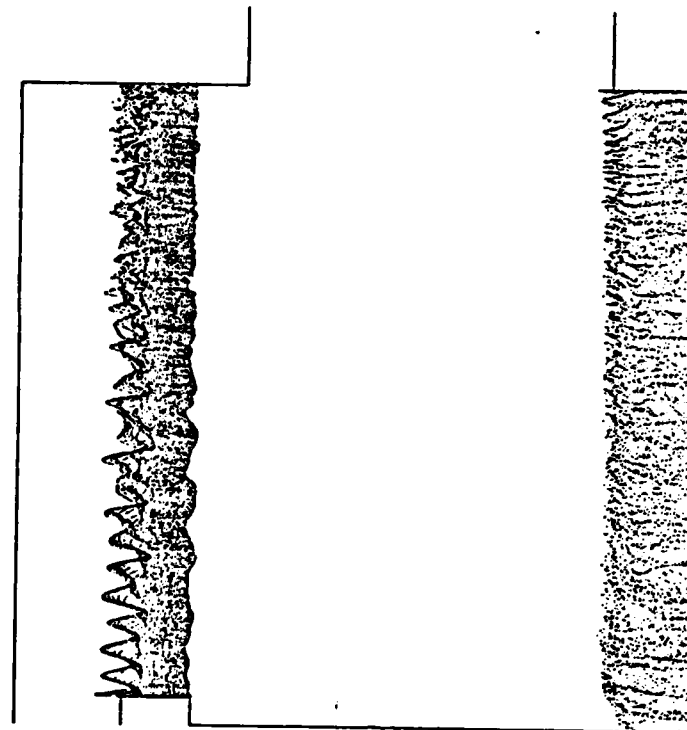
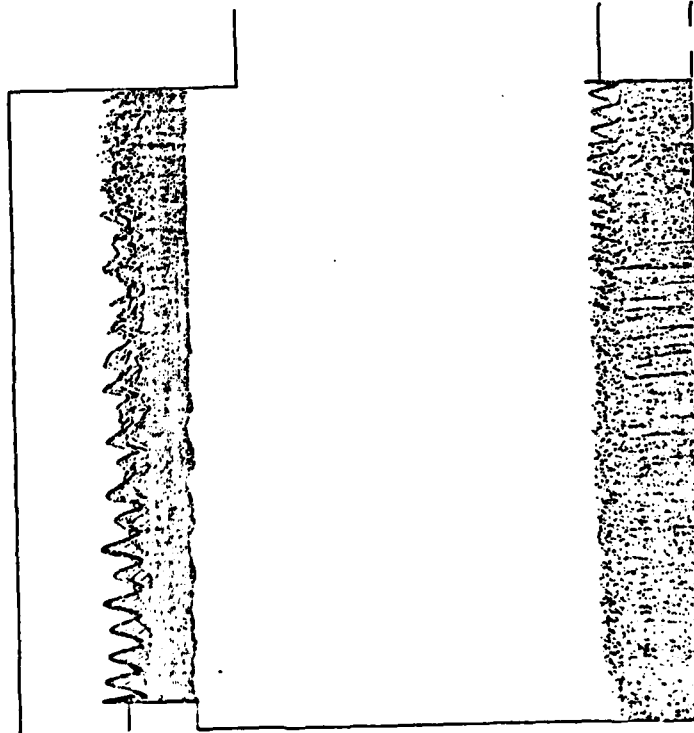


Figure 20. Both Beams at  $t = 2000\Delta t$  and  $t = 2500\Delta t$  for Dual Beam Case I.

MAGIC VERSION JUNE 1983 DATE 9/21/83  
 SIMULATION NRL COLLECTIVE PARTICLE ACCELERATOR  
 TRAJECTORY PLOT OF ELECTRONS ( ISPE = 1 )  
 AT TIME 4.20E-09 SEC FOR 1 TIME STEPS



MAGIC VERSION JUNE 1983 DATE 9/21/83  
 SIMULATION NRL COLLECTIVE PARTICLE ACCELERATOR  
 TRAJECTORY PLOT OF ELECTRONS ( ISPE = 1 )  
 AT TIME 4.90E-09 SEC FOR 1 TIME STEPS

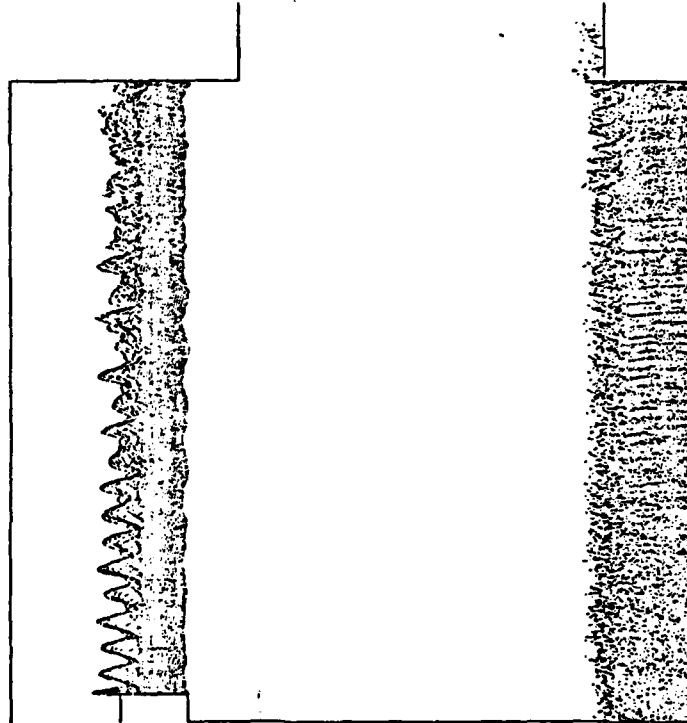


Figure 21. Both Beams at  $t = 3000\Delta t$  and  $t = 3500\Delta t$  for Dual Beam Case I

E1 COMPONENT, SCALD BY 1.000E+00

27456789012345678901234

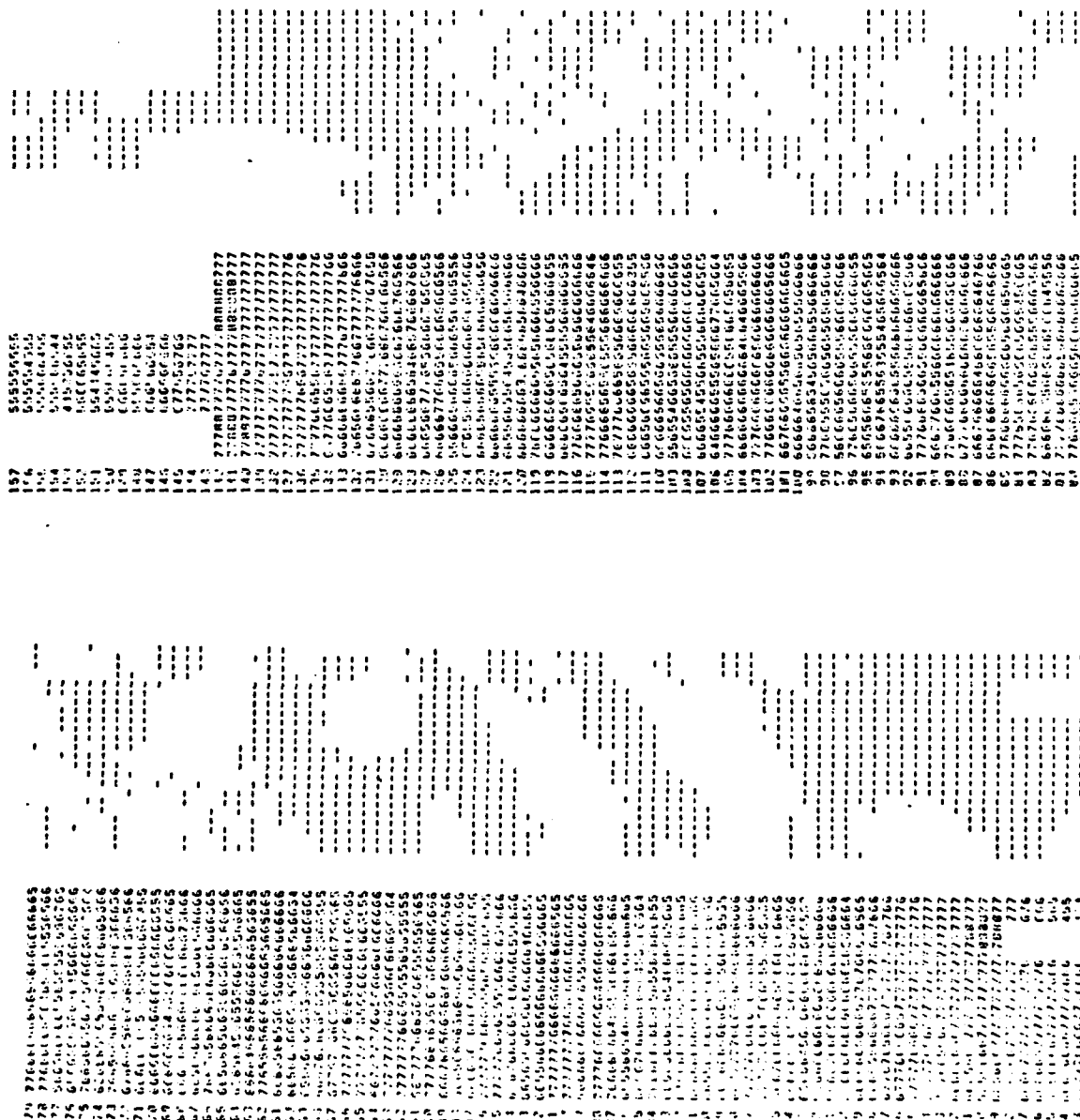


Figure 22.  $E_2$  at  $t = 3500\Delta t$  for Dual Beam Case 1.

137	8088897777
138	8088897777
139	8088897777
140	8088897777
141	8088897777
142	8088897777
143	8088897777
144	8088897777
145	8088897777
146	8088897777
147	8088897777
148	8088897777
149	8088897777
150	8088897777
151	8088897777
152	8088897777
153	8088897777
154	8088897777
155	8088897777
156	8088897777
157	8088897777
158	8088897777
159	8088897777
160	8088897777
161	8088897777
162	8088897777
163	8088897777
164	8088897777
165	8088897777
166	8088897777
167	8088897777
168	8088897777
169	8088897777
170	8088897777
171	8088897777
172	8088897777
173	8088897777
174	8088897777
175	8088897777
176	8088897777
177	8088897777
178	8088897777
179	8088897777
180	8088897777
181	8088897777
182	8088897777
183	8088897777
184	8088897777
185	8088897777
186	8088897777
187	8088897777
188	8088897777
189	8088897777
190	8088897777
191	8088897777
192	8088897777
193	8088897777
194	8088897777
195	8088897777
196	8088897777
197	8088897777
198	8088897777
199	8088897777
200	8088897777

52

uniform region of 8-strength  $E_r$  sandwiched between the hollow beam and the anode tube. This is indicative of the near textbook performance of that beam. The picture of its steady behavior is further enhanced by the axial profiles of  $E_z$  and  $E_r$  as measured at  $t = 4.9$  ns at a radius of  $r = 1.94$  cm. (just inside the hollow beam's outer radius) shown in Figure 24.  $E_z$  in the beam oscillates mildly about zero throughout the entire beam except in the end regions where it goes strongly negative. Conversely,  $E_r$  maintains a rough plateau of approximately  $-1.10 \times 10^8$  V/m along the entire beam except for the ends where it goes to zero. In contrast to these rather classic axial field profiles is the axial profile of  $E_z$  at a radius of  $r = 0.24$  cm (just inside the outer radius of the central beam) shown at the same time in the simulation in Figure 25. In the half of the tube nearest the rod cathode (the right-hand figure) the field behaves as expected. In the downstream half of the tube, however, a region of strong deceleration is encountered at about  $Z = 0.09$  m. and the final peak acceleration field is more than a factor of two lower than that near the cathode.

The macroscopic behavior of this dual beam case is summarized in Figure 26. The upper two plots show the time histories of the hollow cathode and rod cathode voltage pulses respectively. The hollow diode voltage is now 1.5MV, just as in the experiment, but that for the rod cathode reaches a peak value of about 1.7MV which is 0.7MV too great. This was adjusted downward and tested as reported in subsection 5.4 which follows. The final diagnostic shown in the bottom two plots in the figure is the  $B_\theta$  measurement to detect the presence of the central beam current. Both measurements were taken at a radius of 2.345 cm; the left at  $Z = 4.185$  cm and the right at  $Z = 20.395$  cm (see Figure 2). They both show a hollow beam measurement of about  $-0.4$  w/m<sup>2</sup>(= -4kG) or a current of about 47kA, much closer to the experimentally measured value than the previous case. A deflection of at best  $+0.025$  w/m<sup>2</sup>(= +0.25kG) can be detected at about 4 ns indicating a central beam current of about 2.9kA. Since the peak voltage on the rod cathode is so exaggerated, however, this current measurement should not be directly related to the actual experiment.

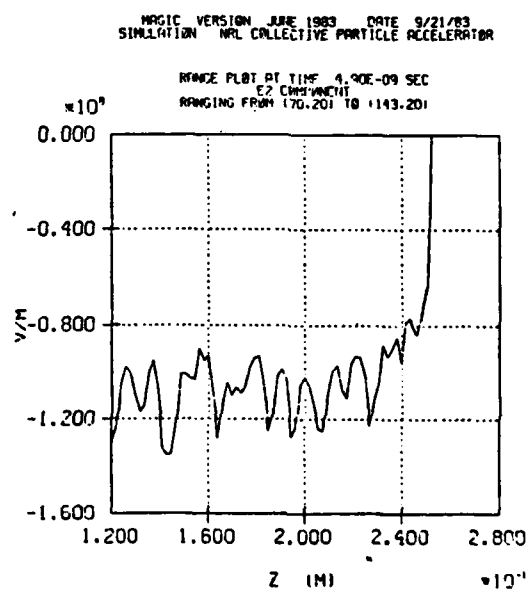
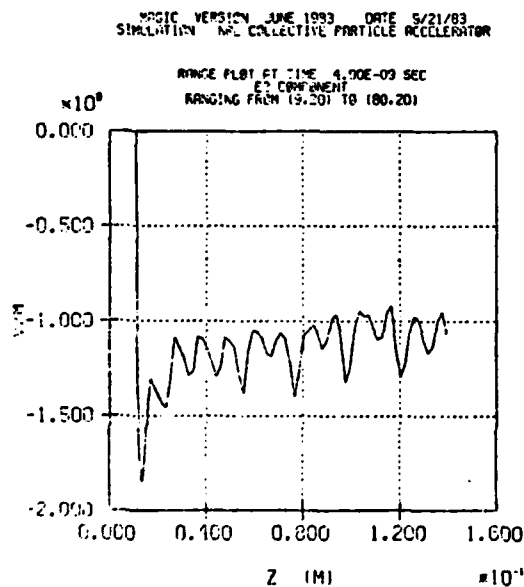
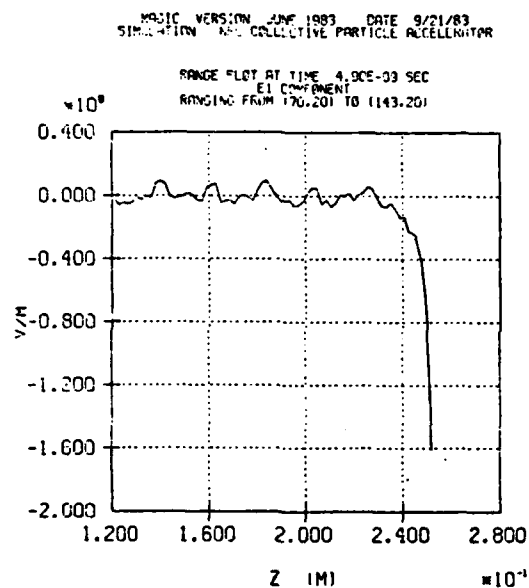
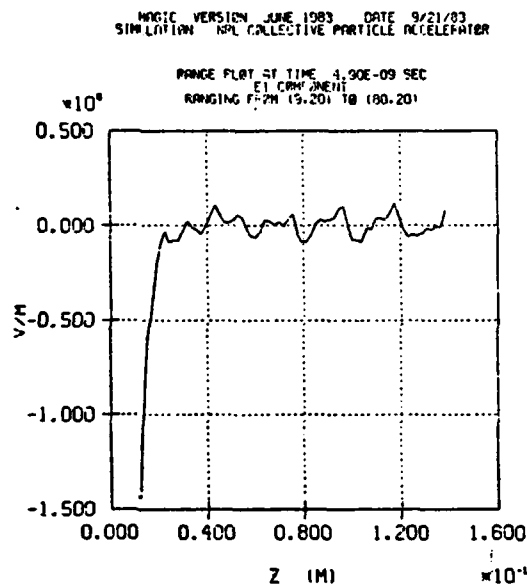
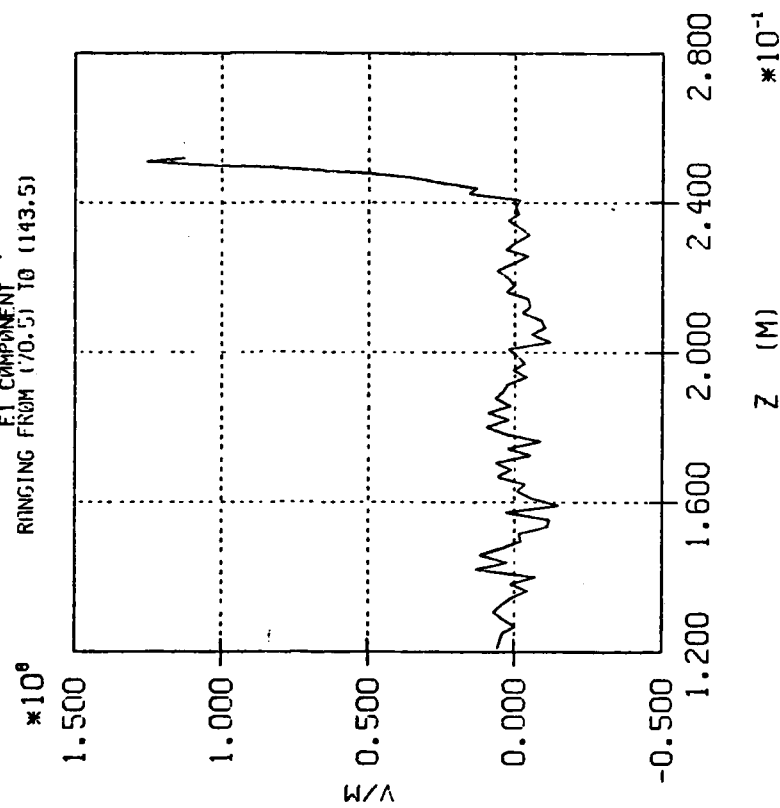


Figure 24. Axial Profiles of  $E_z$  (top) and  $E_r$  (bottom)  
at  $t = 3500 \Delta t$  and  $R = 18 \Delta R$  for Dual Beam Case I.

MAGIC VERSION JUNE 1983 DATE 9/21/83  
SIMULATION NRL COLLECTIVE PARTICLE ACCELERATOR

RANGE PLOT AT TIME 4.90E-09 SEC  
E1 COMPONENT  
RINGING FROM (70.5) TO (143.5)



MAGIC VERSION JUNE 1983 DATE 9/21/83  
SIMULATION NRL COLLECTIVE PARTICLE ACCELERATOR

RANGE PLOT AT TIME 4.90E-09 SEC  
E1 COMPONENT  
RINGING FROM (12.5) TO (160.5)

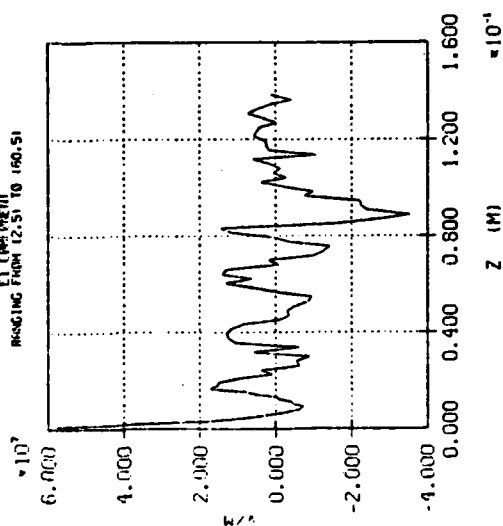


Figure 25. Axial Profile of  $E_z$  at  $R = 3\Delta r$  and  $t = 3500\Delta t$  for Dual Beam Case I.



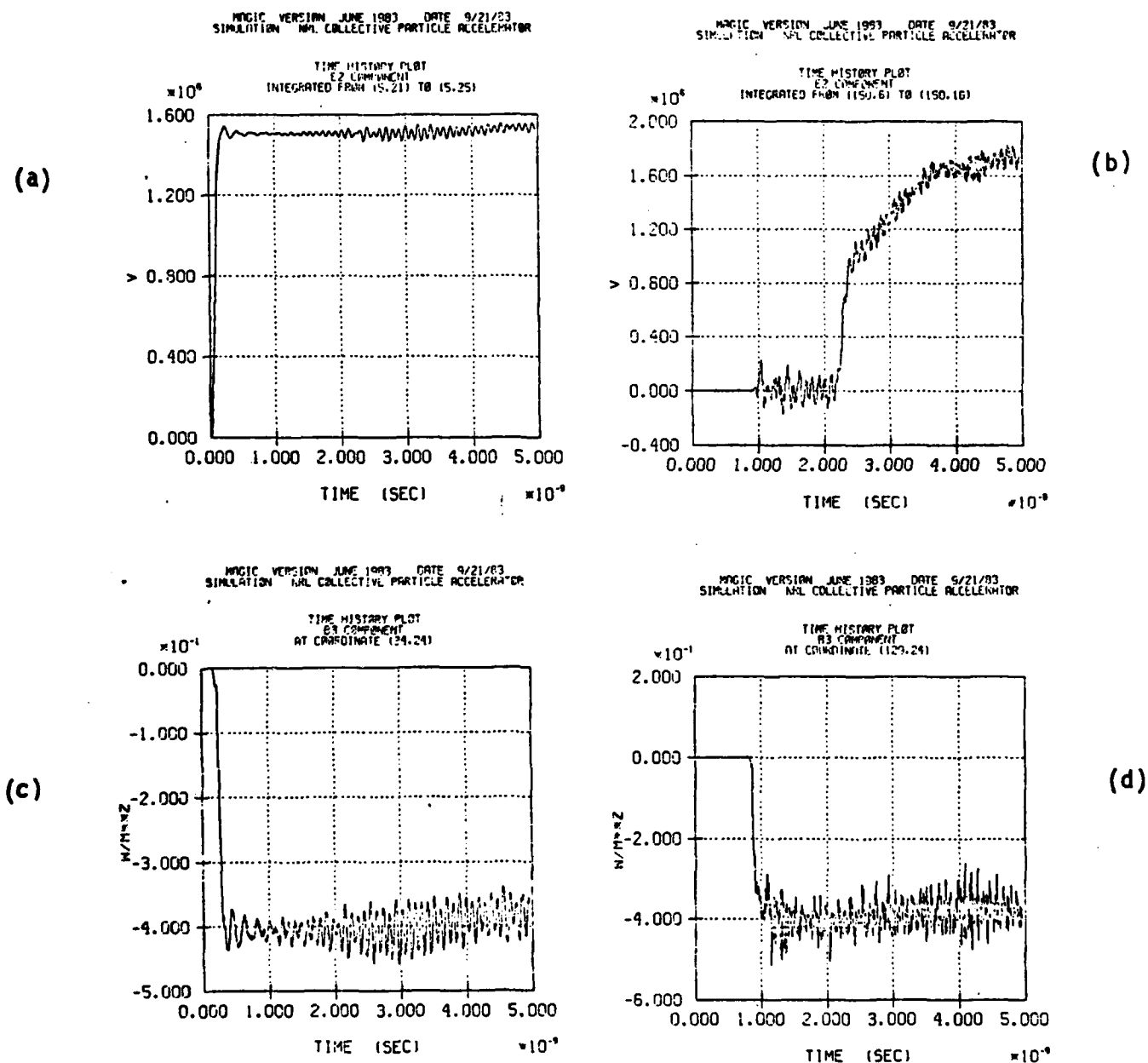


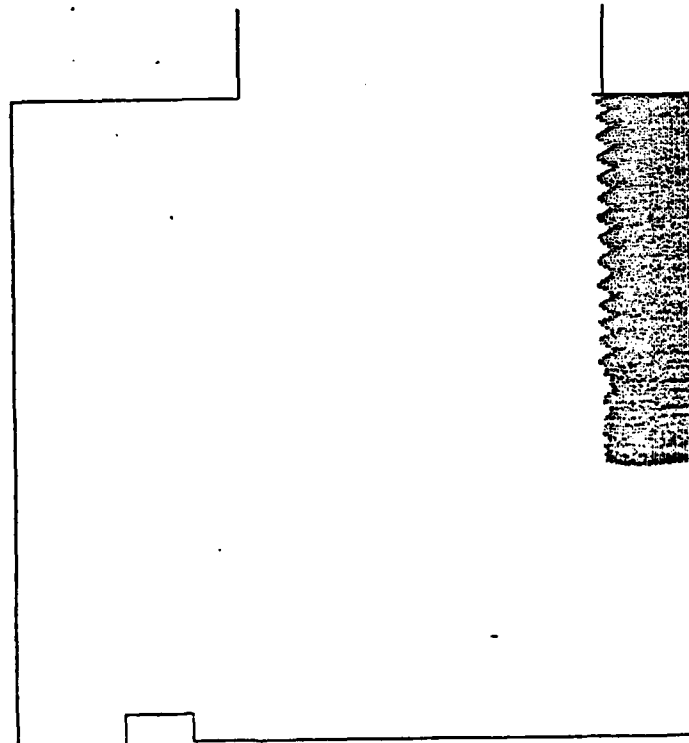
Figure 26. Case I Time Histories for (a) Hollow Cathode Voltage, (b) Rod Cathode Voltage, (c)  $B_\theta$  at (34,24), and (d)  $B_\theta$  at (129,24) For Dual Beam Case I.

5.4 Central Beam Only. At this point in the research effort, it was deemed necessary to simulate the CPA model device in the absence of the hollow beam. Running this case with only the central beam present accomplished two major objectives: first, the applied voltage on the rod cathode was adjusted downward to realize the correct 1.0 MV of measured voltage and, second, a benchmark figure for the full current of the central beam was obtained. For the purposes of this simulation, the voltage pulse applied to the rod diode was changed to the same form as that which had been applied to the hollow cathode in the previous runs. (No voltage is applied to the hollow cathode in this run.) The pulse turns "on" at  $t = 0$  with a linear, rapid rise to a plateau value of 0.615 MV in 0.0925 ns.

The formation and propagation of the central beam for these operating conditions is documented in the sample electron particle plots of Figures 27 and 28. Some degree of what appears to be striation structure is visible in the downstream, left one-third of the beam, but no intensification of the structure or perturbations to the beam propagation is evident. The beam seems to propagate freely. The good behavior of the beam is reinforced by the classic shape of the  $E_z$  axial profile shown in Figure 29. Measured at a constant radius of 0.24 cm (just inside the outer radius of the beam), it oscillates only mildly about zero over almost the entire length of the beam except for the two end regions where sharp axial acceleration takes place.

The validity of our choice for the applied voltage is affirmed by the upper left time history plot of Figure 30. A near perfect 1.0 MV is measured radially across the rod diode gap. Out of curiosity, a similar voltage measurement was made axially down the length of the tube at a radius of 0.24 cm between the rod cathode and the (floating) hollow cathode. This is shown in the upper right plot of the same figure. The transit time for the electromagnetic wave is clearly visible in the voltage jump at about one nanosecond. The plateau voltage measured in this manner is only slightly less than 1.0 MV. To gauge the effect of the

MAGIC VERSION JUNE 1983 DATE 10/17/83  
 SIMULATION NRL COLLECTIVE PARTICLE ACCELERATOR  
 TRAJECTORY PLOT OF ELECTRONS ( JSPE = 1 )  
 AT TIME 7.00E-10 SEC FOR 1 TIME STEPS



MAGIC VERSION JUNE 1983 DATE 10/17/83  
 SIMULATION NRL COLLECTIVE PARTICLE ACCELERATOR  
 TRAJECTORY PLOT OF ELECTRONS ( JSPE = 1 )  
 AT TIME 1.05E-09 SEC FOR 1 TIME STEPS

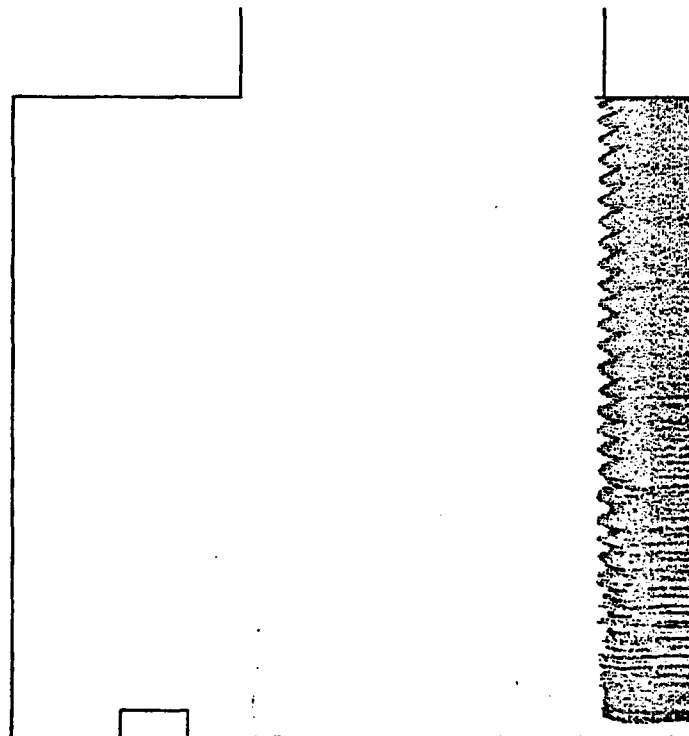
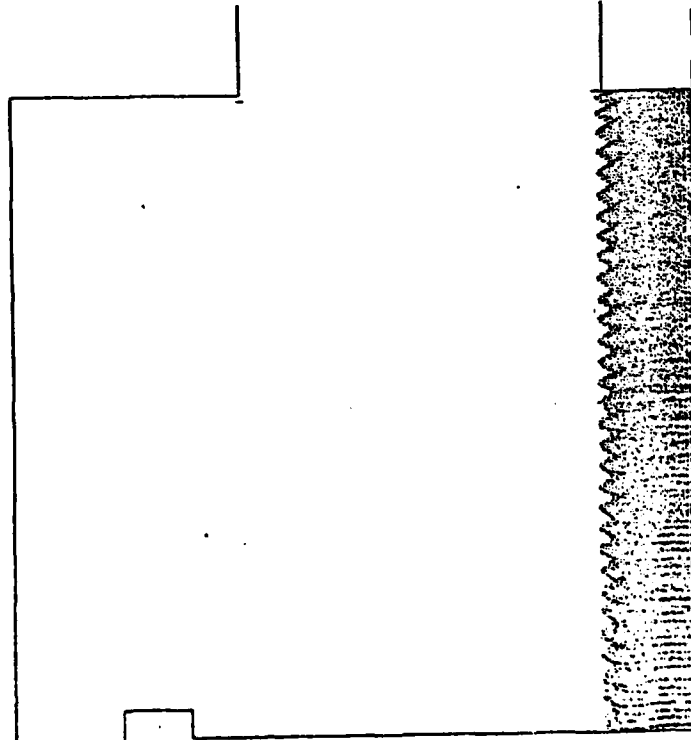


Figure 27. Central Beam at  $t = 500\Delta t$  and  $t = 750\Delta t$ .

MAGIC VERSION JUNE 1983 DATE 10/19/83  
 SIMULATION NRL COLLECTIVE PARTICLE ACCELERATOR  
 TRAJECTORY PLOT OF ELECTRONS ( ISPE = 1 )  
 AT TIME 2.45E-09 SEC FOR 1 TIME STEPS



MAGIC VERSION JUNE 1983 DATE 10/20/83  
 SIMULATION NRL COLLECTIVE PARTICLE ACCELERATOR  
 TRAJECTORY PLOT OF ELECTRONS ( ISPE = 1 )  
 AT TIME 3.50E-09 SEC FOR 1 TIME STEPS

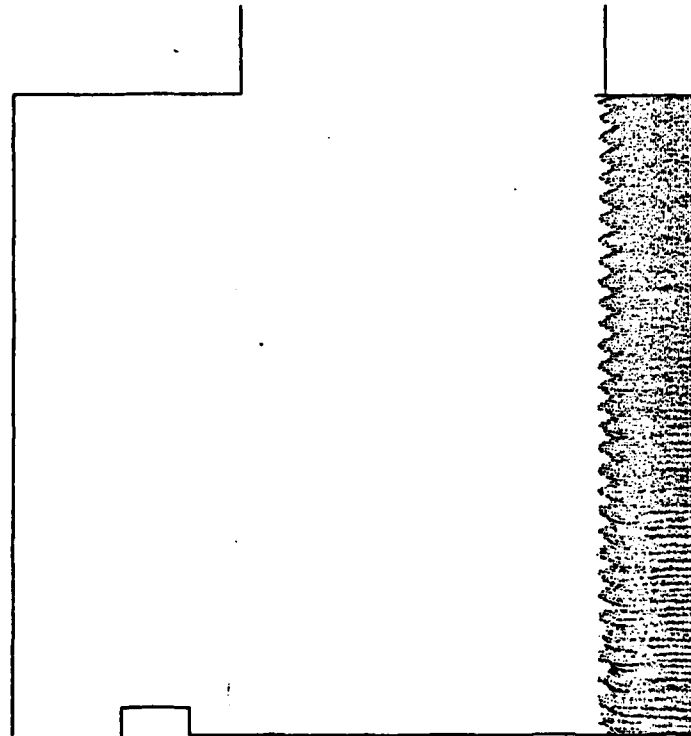
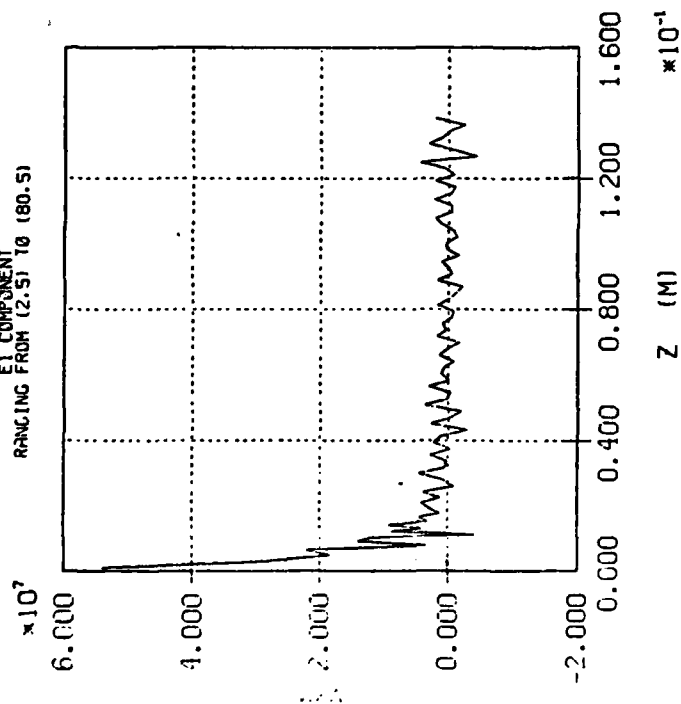


Figure 28. Central Beam at  $t = 1750\Delta t$  and  $t = 2500\Delta t$ .

MAGIC VERSION JUNE 1983 DATE 10/20/83  
SIMULATION NRL COLLECTIVE PARTICLE ACCELERATOR

RANGE PLOT AT TIME 3.50E-09 SEC  
E1 COMPONENT  
RANGING FROM (2.5) TO (80.5)



MAGIC VERSION JUNE 1983 DATE 10/20/83  
SIMULATION NRL COLLECTIVE PARTICLE ACCELERATOR

RANGE PLOT AT TIME 3.50E-09 SEC  
E1 COMPONENT  
RANGING FROM (170.5) TO (1143.5)

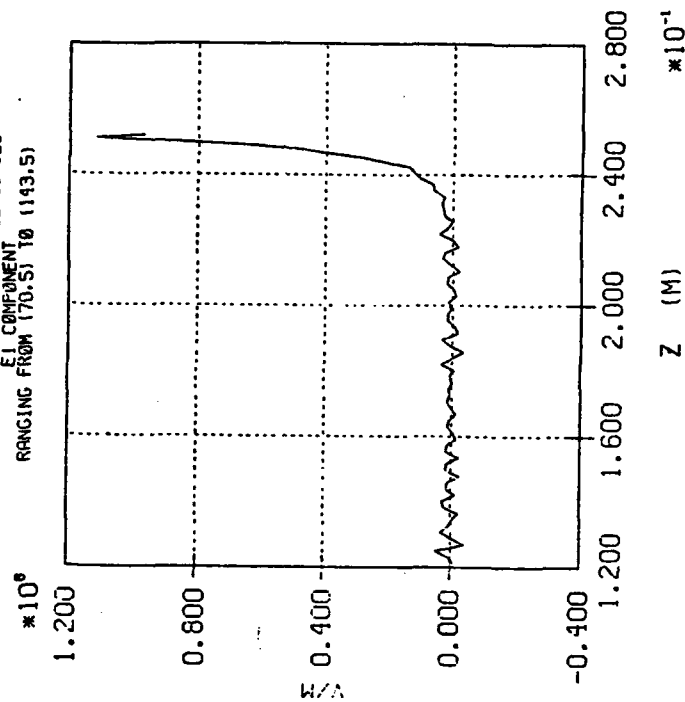


Figure 29. Axial Profile of  $E_z$  at  $t = 2500\Delta t$  and  $R = 3\Delta R$  for Central Beam Case.

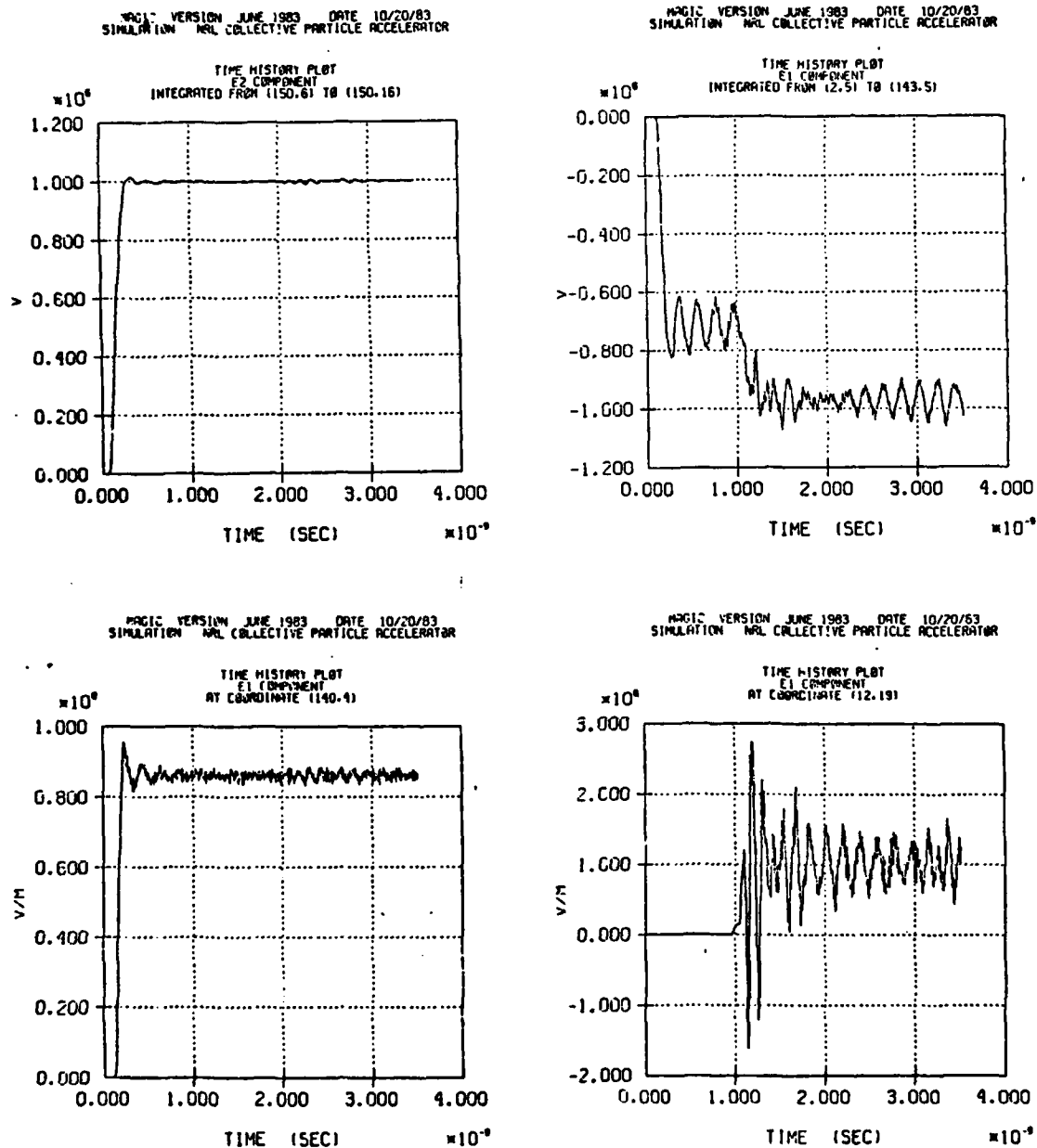


Figure 30. Time History Plots for Radially and Axially Measured Voltages of Rod Cathode (top Left and Right) and  $E_z$  Measured at tip of Rod Cathode and Hollow Cathode (bottom Left and Right) for Central Beam.

central beam on the normal electric fields at the tip of each cathode which, in turn, governs the emission rate there, time histories of  $E_z$  measured at the tip of the rod cathode (left) and hollow cathode (right) are also shown in the bottom two plots of Figure 30. A quite stable  $0.86 \times 10^8 \text{ V/m}$  is measured at the rod cathode while only an insignificant  $1.0 \times 10^6 \text{ V/m}$  is measured at the hollow cathode. Clearly, the central beam exerts very little influence on the emission characteristics of the hollow beam. The final diagnostic for this case is the all-important current measurement benchmark for the beam. This is obtained directly from the time history plots of Figure 31 which track  $B_\theta$  at a constant radius of 1.41 cm for axial distances of 0.22 (top left), 2.235 (top right), 4.565 (bottom left), and 19.955 cm (bottom right) downstream of the tip of the rod cathode. All four measurements yield a plateau  $B_\theta$  of  $0.034 \text{ w/m}^2$  ( $= 0.34 \text{ kG}$ ) which indicates a steady central beam current of about 2.4 kA. This is in excellent agreement with experimental findings of 2-3 kA.

5.5 Dual Beam Case II. There now remained only to run the full, dual beam case with both applied voltages properly adjusted. In addition, as in the previous case, the rod cathode was brought linearly to full voltage in under a tenth of a nanosecond (after the hollow beam was established) so that full voltage operation of the central beam could be observed before electrons reflected from the opposing hollow cathode wall could interfere with the bulk of the beam. (Remember, in the experiment, the tube was 5 meters long so a slow pulse rise time could be tolerated without worrying about electrons reflected from the far end of the tube.) To greatly enhance insight into the detailed physics of the beams, phase space plots were also added to the simulation diagnostics package.

As in the previous dual beam case, the hollow beam was allowed time to equilibrate before a voltage was applied to the rod diode. Specifically, 1.5 ns elapsed before rod cathode "turn-on". The subsequent development of the central beam is glimpsed at  $t = 2.45, 2.80, 3.15, 3.50, 3.85,$  and  $4.20 \text{ ns}$  in Figures 32 through 37 respectively. The left half of each

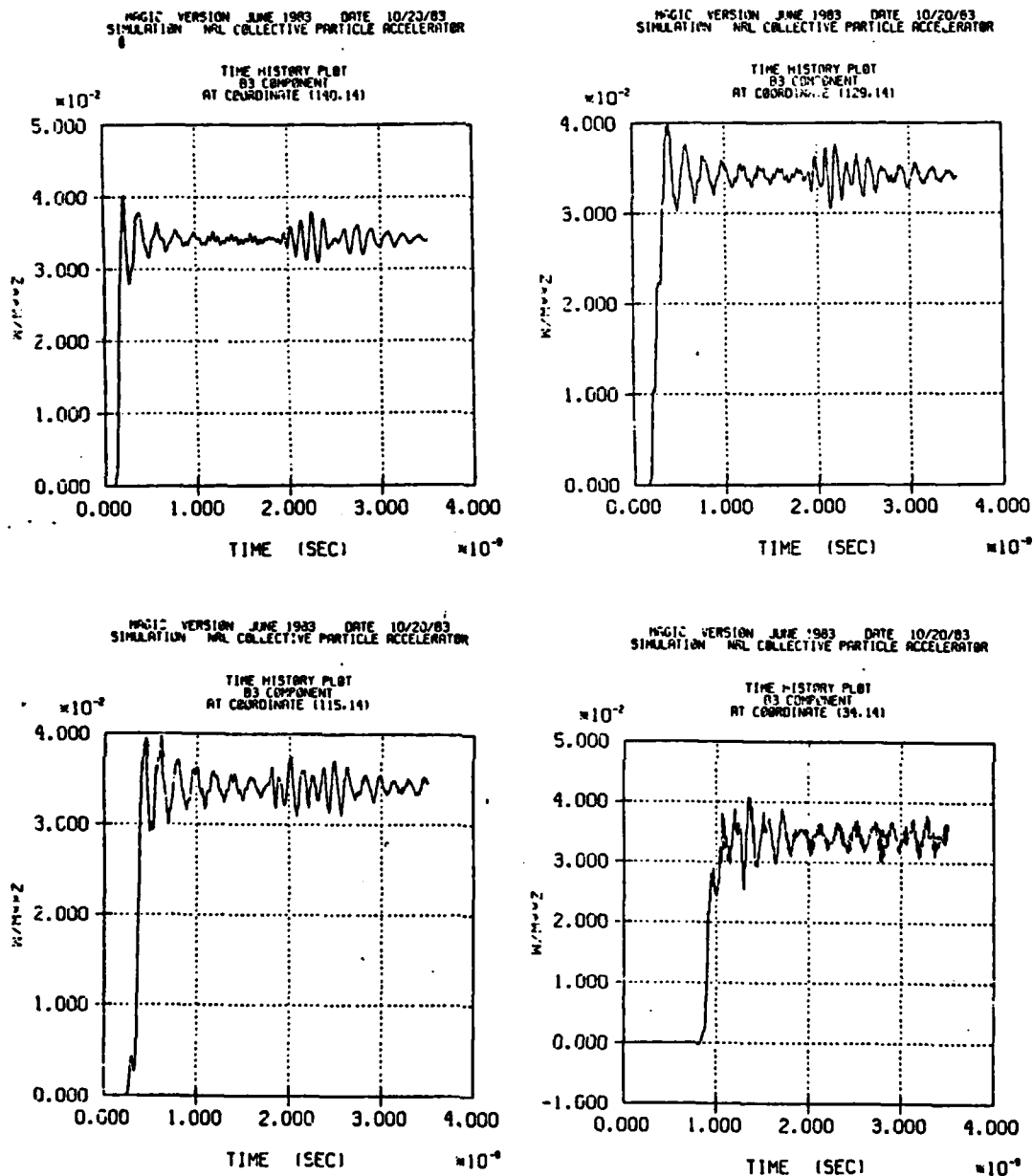
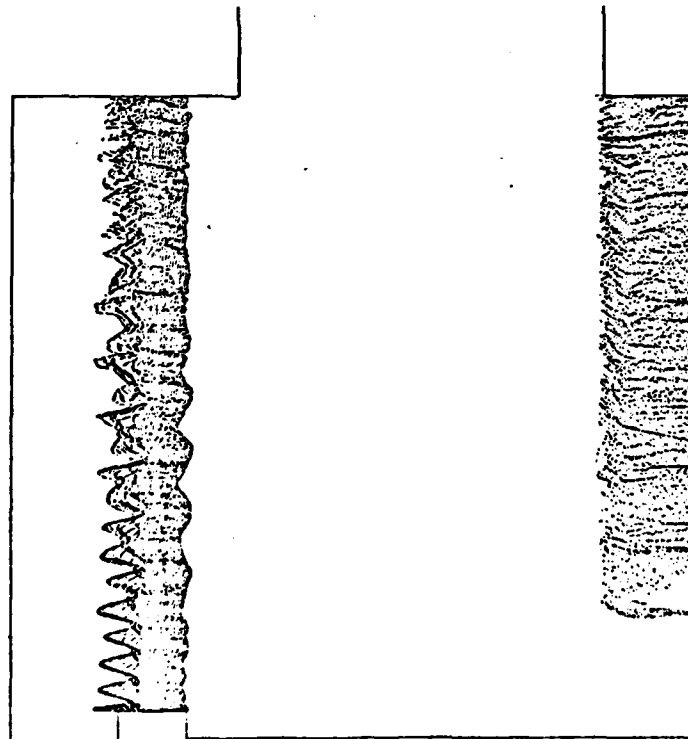


Figure 31. Time History Plots for  $B_0$  Measured at  $R = 1.41$  cm for Distances of 0.22 (top left), 2.235 (top right), 4.565 (bottom left), and 19.955 cm (bottom right) Downstream of Rod Cathode for Central Beam Case.



MAG:C VERSION JUNE 1983 DATE 10/23/83  
 SIMULATION NRL COLLECTIVE PARTICLE ACCELERATOR  
 TRAJECTORY PLOT OF ELECTRONS ( ISPE = 1 )  
 FIT TIME 2.45E-09 SEC FOR 1 TIME STEPS



MAG:C VERSION JUNE 1983 DATE 10/23/83  
 SIMULATION NRL COLLECTIVE PARTICLE ACCELERATOR

PHASE-SPACE PLOT OF P1 VS. X1 AT TIME 2.45E-09 SEC  
 SPECIES NUMBER 1 O/H RATIO -1.759E+11  
 X2 WINDOW 0.00E+00 TO 1.00E-02  
 P2 WINDOW -1.00E+10 TO 1.00E+10  
 P3 WINDOW -1.00E+10 TO 1.00E+10

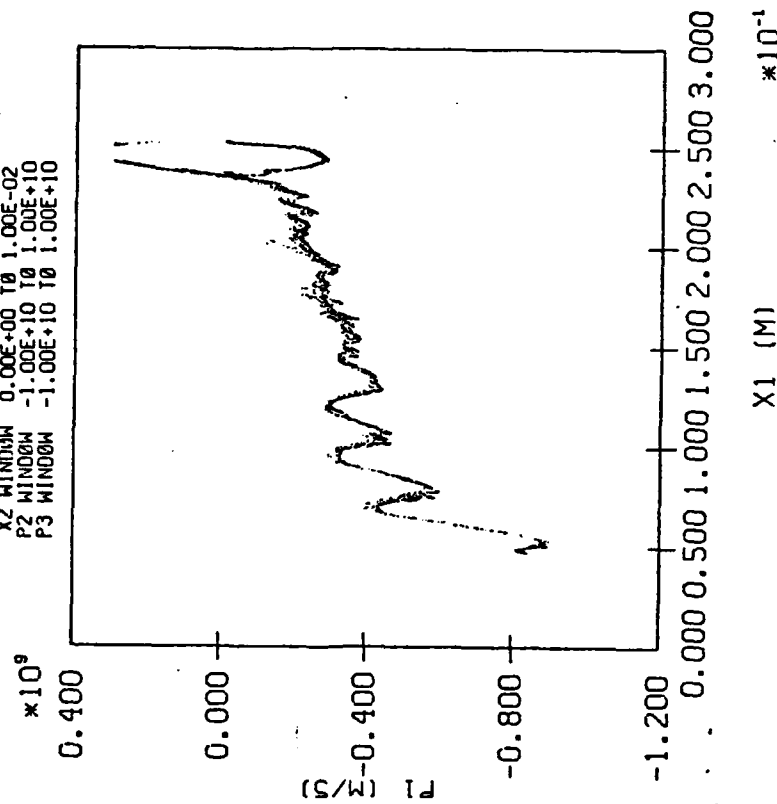
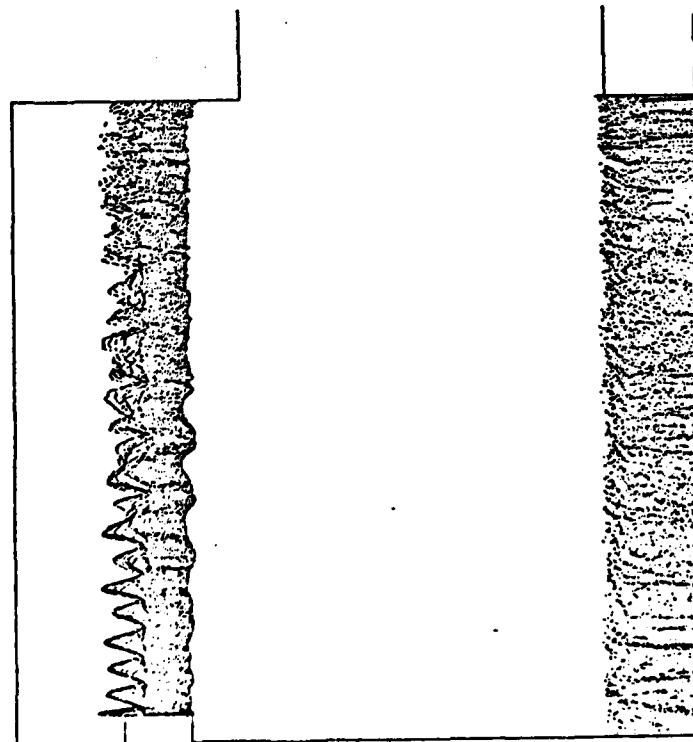


Figure 32. Real Space Plot for Both Beams and Phase Space Plot for  
 Central Central Beam for Dual Beam Case II at  $t = 1750\Delta t$ .

MAGIC VERSION JUNE 1983 DATE 10/23/83  
 SIMULATION NRL COLLECTIVE PARTICLE ACCELERATOR  
 TRAJECTORY PLOT OF ELECTRONS (LSPE = 1.1)  
 AT TIME 2.80E-09 SEC FOR 1 TIME STEPS



MAGIC VERSION JUNE 1983 DATE 10/23/83  
 SIMULATION NRL COLLECTIVE PARTICLE ACCELERATOR  
 PHASE-SPACE PLOT OF P1 VS. X1 AT TIME 2.80E-09 SEC  
 SPECIES NUMBER 1 Q/M RATIO -1.759E+11  
 X2 WINDOW 0.00E+00 TO 1.00E-02  
 P2 WINDOW -1.00E+10 TO 1.00E+10  
 P3 WINDOW -1.00E+10 TO 1.00E+10

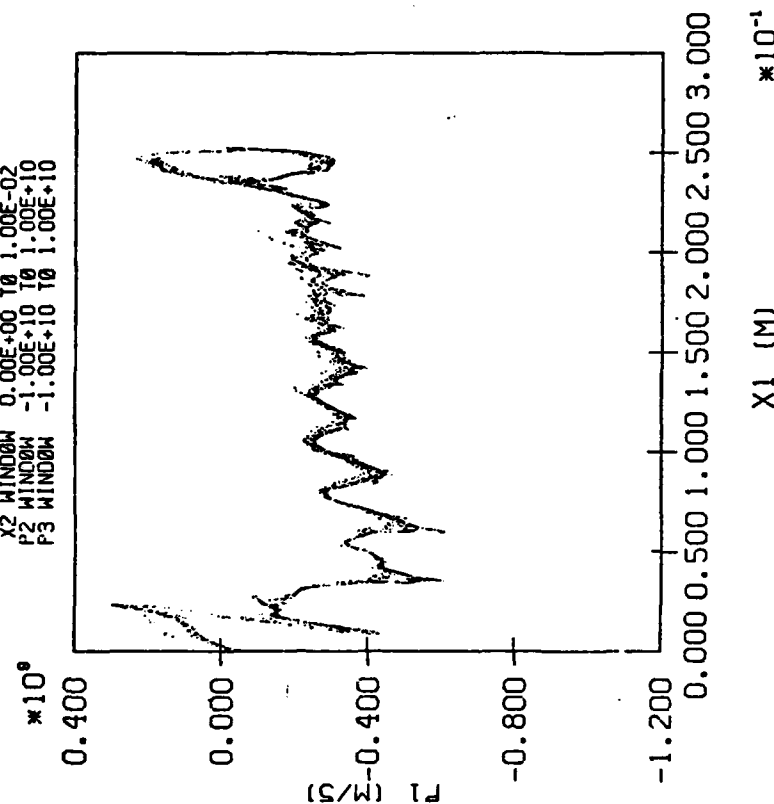
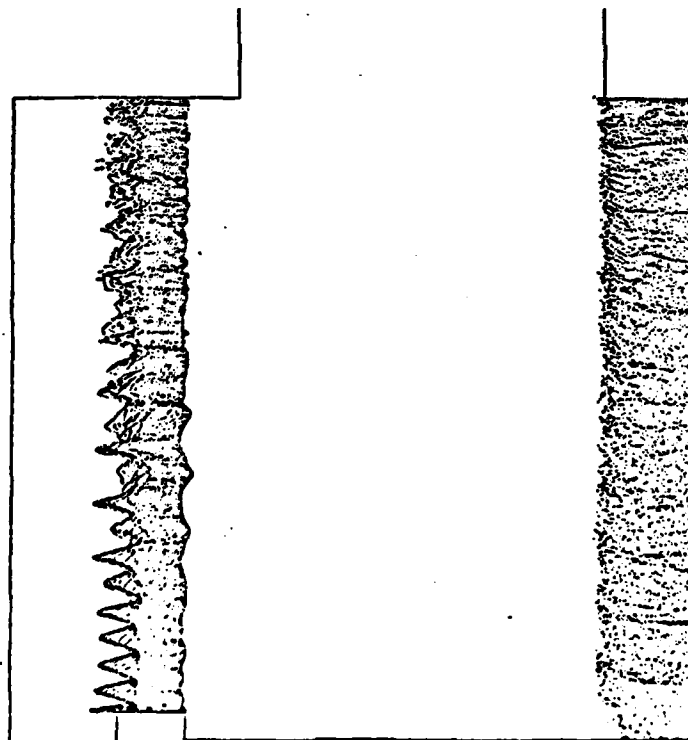


Figure 33. Real Space Plot for Both Beams and Phase Space Plot for Central Beam for Dual Beams Case II at  $t = 2000\Delta t$ .

MAGIC VERSION JUNE 1983 DATE 10/25/83  
SIMULATION NRL COLLECTIVE PARTICLE ACCELERATOR

TRAJECTORY PLOT OF ELECTRONS ( ISPE = 1 )  
AT TIME 3.15E-09 SEC FOR 1 TIME STEPS



MAGIC VERSION JUNE 1983 DATE 10/25/83  
SIMULATION NRL COLLECTIVE PARTICLE ACCELERATOR

PHASE-SPACE PLOT OF P1 VS. X1 AT TIME 3.15E-09 SEC  
SPECIES NUMBER 1 Q/M RATIO -1.759E+11  
X2 WINDOW 0.00E+00 TO 1.00E-02  
P2 WINDOW -1.00E+10 TO 1.00E+10  
P3 WINDOW -1.00E+10 TO 1.00E+10

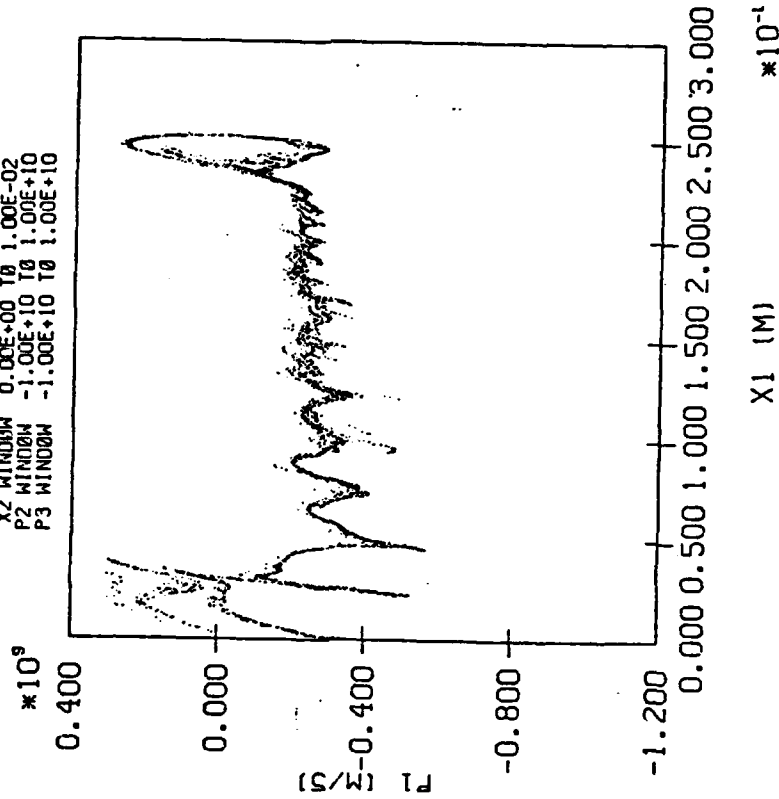


Figure 34. Real Space Plot for Both Beams and Phase Space Plot for Central Beam for Dual Beams Case II at  $t = 2250\Delta t$ .

MAGIC VERSION JUNE 1983 DATE 10/25/83  
SIMULATION NRL COLLECTIVE PARTICLE ACCELERATOR

PHASE-SPACE PLOT OF P1 VS. X1 AT TIME 3.50E-09 SEC  
SPECIES NUMBER 1 Q/M RATIO -1.75E+11  
X2 WINDOW 0.00E+00 TO 1.00E-02  
P2 WINDOW -1.00E+10 TO 1.00E+10  
P3 WINDOW -1.00E+10 TO 1.00E+10

$\times 10^9$

C.400

0.000

P1 (M/5)

-0.400

-0.800

-1.200

0.000 0.500 1.000 1.500 2.000 2.500 3.000

X1 (M)

$\times 10^{-1}$

MAGIC VERSION JUNE 1983 DATE 10/25/83  
SIMULATION NRL COLLECTIVE PARTICLE ACCELERATOR

TRAJECTORY PLOT OF ELECTRONS (ISPE = 1)  
AT TIME 3.50E-09 SEC FOR 1 TIME STEPS

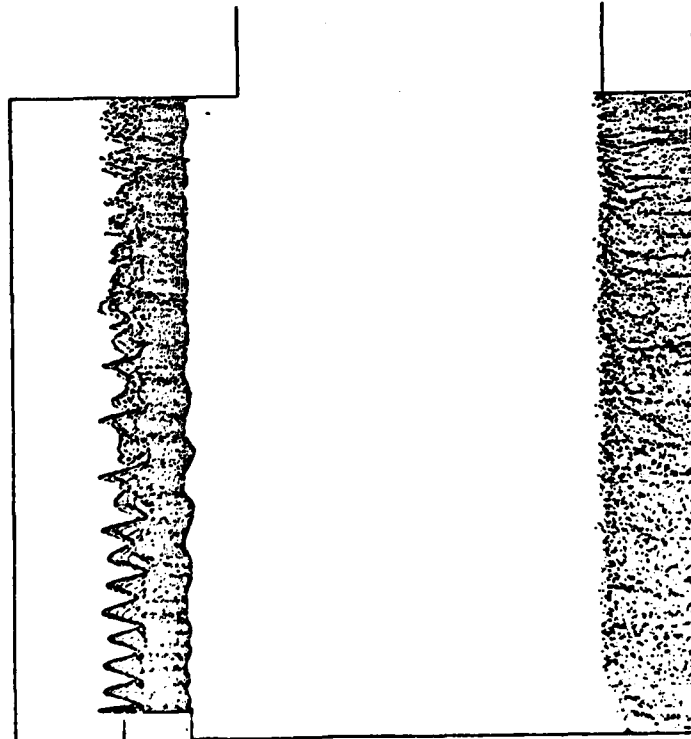
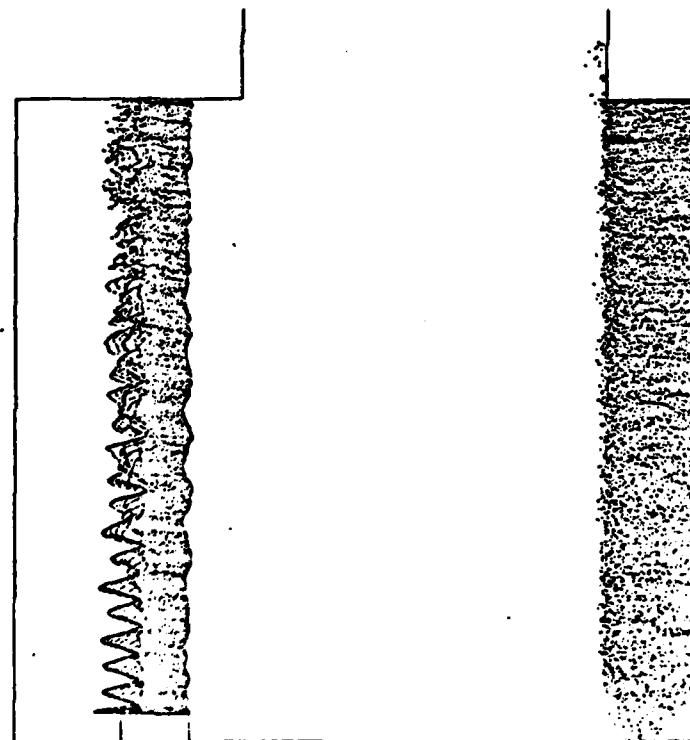


Figure 35. Real Space Plot for Both Beams and Phase Space Plot for Central Beam for Dual Beam Case II at  $t = 2500\Delta t$ .

MAGIC VERSION JUNE 1983 DATE 10/26/83  
 SIMULATION NRL COLLECTIVE PARTICLE ACCELERATOR  
 TRAJECTORY PLOT OF ELECTRONS (ISPE = 1)  
 AT TIME 3.85E-09 SEC FOR 1 TIME STEPS



MAGIC VERSION JUNE 1983 DATE 10/26/83  
 SIMULATION NRL COLLECTIVE PARTICLE ACCELERATOR  
 PHASE-SPACE PLOT OF P1 VS. X1 AT TIME 3.85E-09 SEC  
 SPECIES NUMBER 1 O/M RATIO -1.759E+14  
 X2 WINDOW 0.00E+00 TO 1.00E-02  
 P2 WINDOW -1.00E+10 TO 1.00E+10  
 P3 WINDOW -1.00E+10 TO 1.00E+10

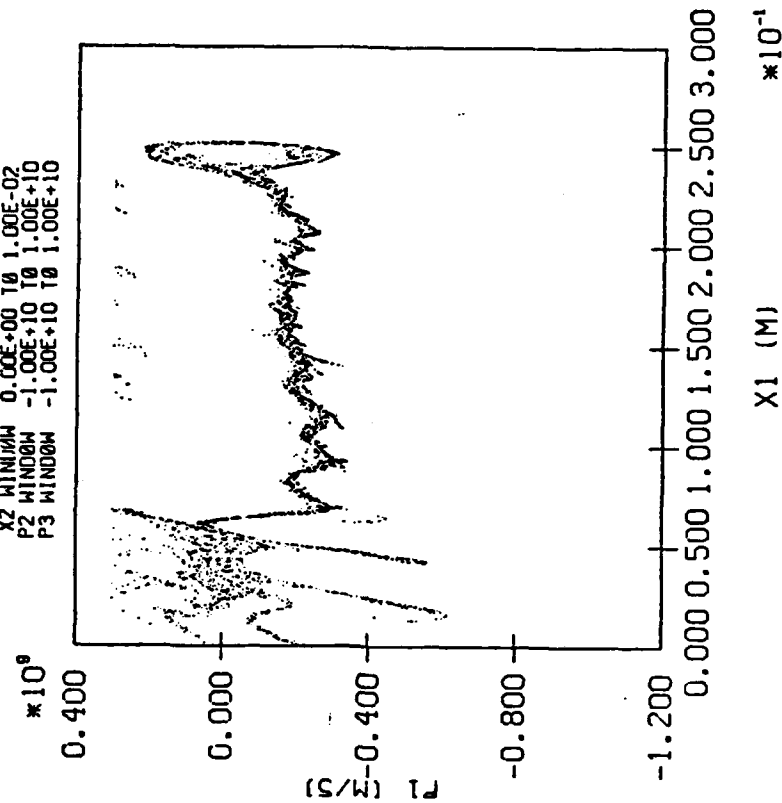
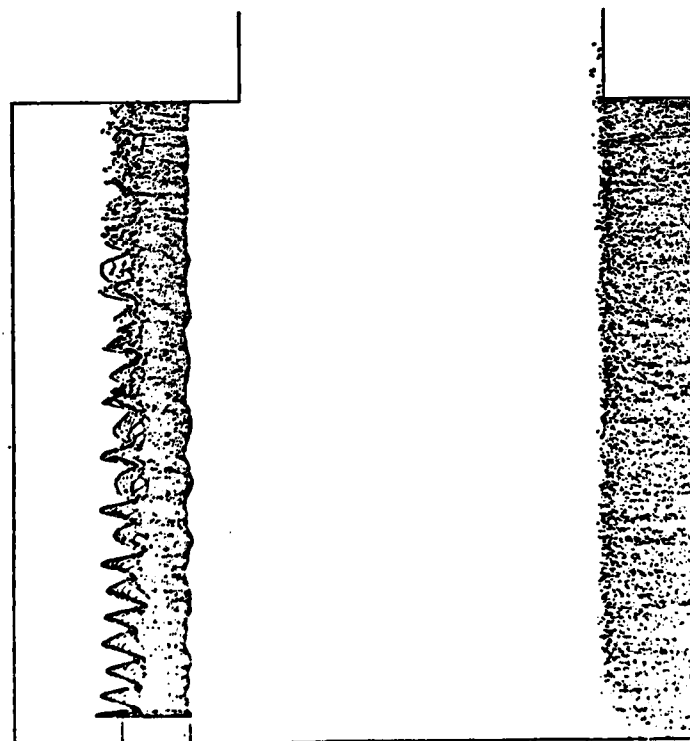


Figure 36. Real Space Plot for Both Beams and Phase Space Plot for Central Beam for Dual Beam Case II at  $t = 2750\Delta t$ .

MAGIC VERSION JUNE 1983 DATE 10/26/83  
SIMULATION NRL COLLECTIVE PARTICLE ACCELERATOR

TRAJECTORY PLOT OF ELECTRONS ( ISPE = 1 )  
AT TIME 4.20E-09 SEC FOR 1 TIME STEPS



MAGIC VERSION JUNE 1983 DATE 10/26/83  
SIMULATION NRL COLLECTIVE PARTICLE ACCELERATOR

PHASE-SPACE PLOT OF P1 VS. X1 AT TIME 4.20E-09 SEC  
SPECIES NUMBER 1 D/N RATIO -1.759E+11  
X2 WINDOW 0.00E+00 TO 1.00E-02  
P2 WINDOW -1.00E+10 TO 1.00E+10  
P3 WINDOW -1.00E+10 TO 1.00E+10

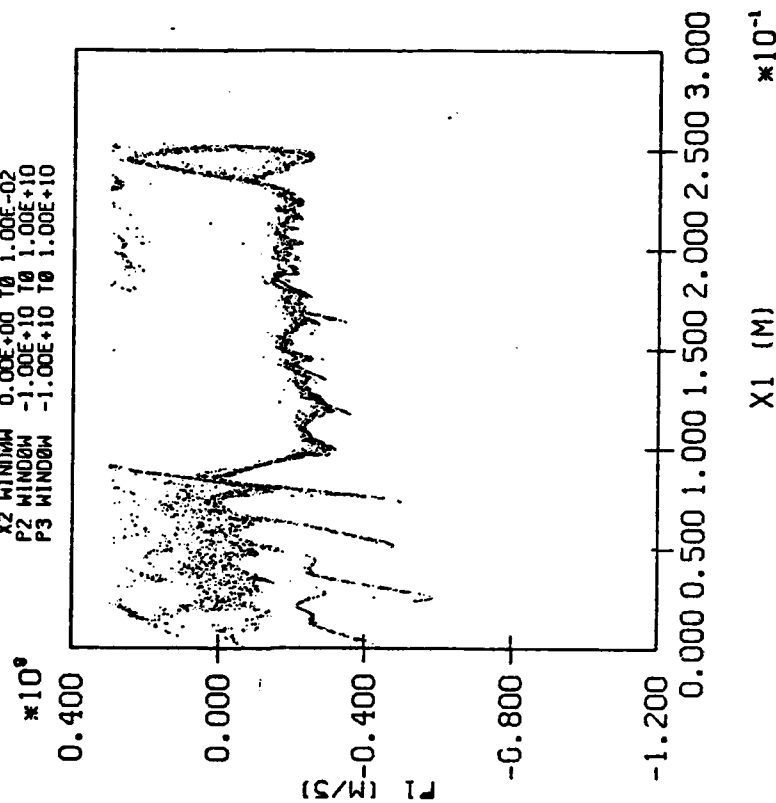


Figure 37. Real Space Plot for Both Beams and Phase Space Plot for Central Beam for Dual Beam Case II at  $t = 3000\Delta t$ .

figure presents a sample electron position plot while the right half shows the  $P_z$  versus  $Z$  phase-space plot for the central beam electrons. The key result to be gleaned from these figures is clear; a region containing a strongly reflected component of electrons is formed almost immediately in the central beam between  $Z = 23$  and  $Z = 25$  cm (i.e. right off the tip of the rod cathode). This indicates the presence of a virtual cathode there. Such an entity arises due to a local build-up of electron space-charge which, in turn, probably arose from the previously observed "reversed" E-field created all along that end of the tube due to the presence of the outer beam. This reflected electron structure persists through all of the subsequent time figures. The corresponding particle position plots also show evidence of enhanced electron number density in the region less than two centimeters downstream from the rod cathode tip. In all but the first of this set of figures, are visible electrons reflected from the opposing hollow cathode wall (which is at a lower potential). These electrons clearly wreak havoc with the extreme downstream portion of the central beam but have not interfered with the important upstream physics during the course of this simulation. The correspondence with the experiment is therefore complete.

To round out the phase space picture of the simulation, two further figures are provided. Figure 38 plots  $P_z$  versus  $Z$  for all of the electron particles in the hollow beam at  $t = 4.2$  ns into the simulation. It shows what the axial phase space should look like for a typical foilless diode beam. Contrasting it to the previous plots for the central beam phase space highlights how severely that beam has been disrupted by the presence of the hollow beam. Figure 39, on the other hand, shows the central beam to be radially "quieter" than the hollow beam. It plots  $P_r$  versus  $P_z$  side-by-side for both beams. Average hollow beam electrons appear to have a significantly greater portion of their kinetic energy tied to radial motion. This gives rise to yet another interesting point. Electrons in the hollow beam with finite radial velocities will interact with the 25 kG imposed  $B_z$  to yield a finite azimuthal current density. This  $J_\theta$  (particularly if shank emission is allowed) could result in a

MAGIC VERSION JUNE 1983 DATE 10/26/83  
SIMULATION NRL COLLECTIVE PARTICLE ACCELERATOR

PHASE-SPACE PLOT OF P1 VS. X1 AT TIME 4.20E-09 SEC

SPECIES NUMBER 1 Q/M RATIO -1.759E+11

X2 WINDOW 1.00E-02 TO 2.40E-02

P2 WINDOW -1.00E+10 TO 1.00E+10

P3 WINDOW -1.00E+10 TO 1.00E+10

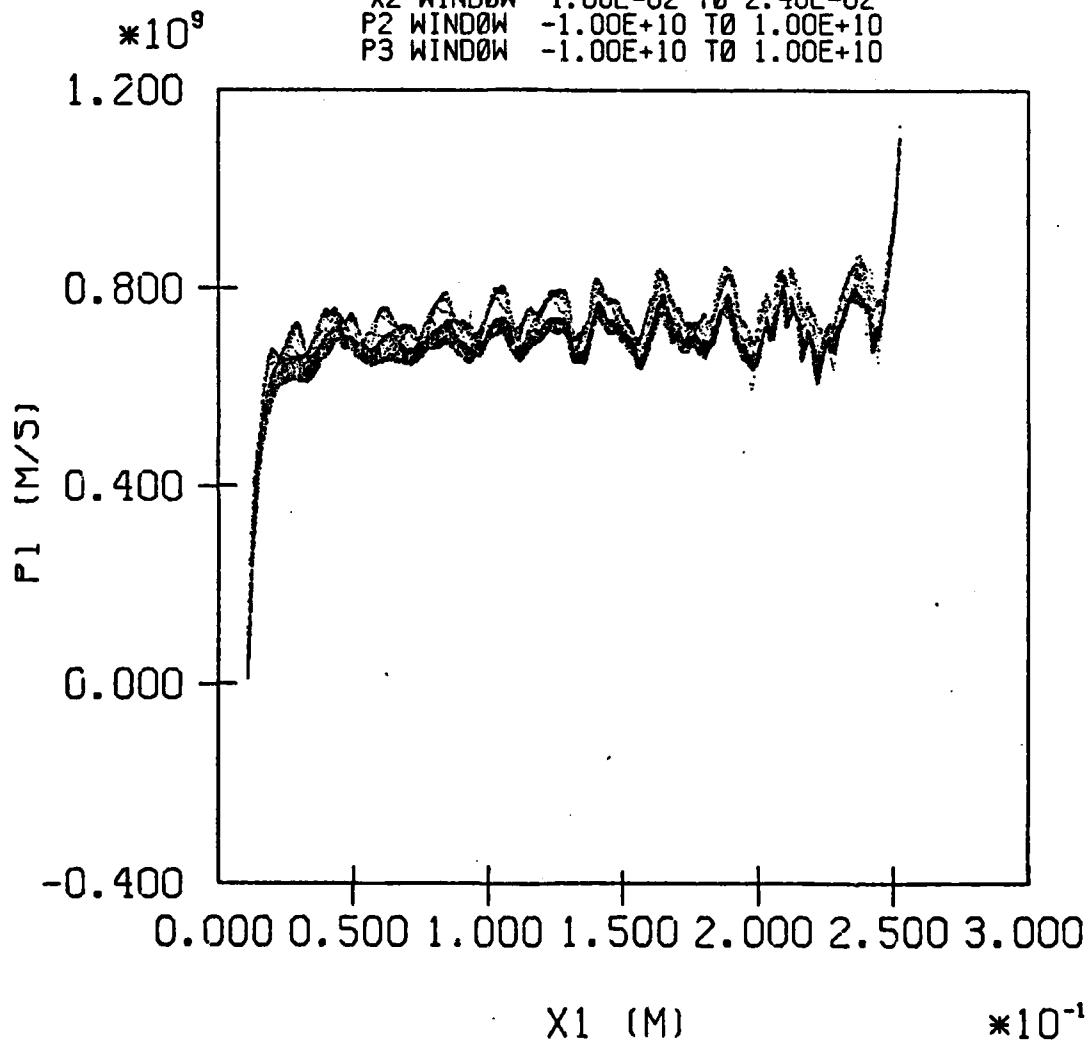
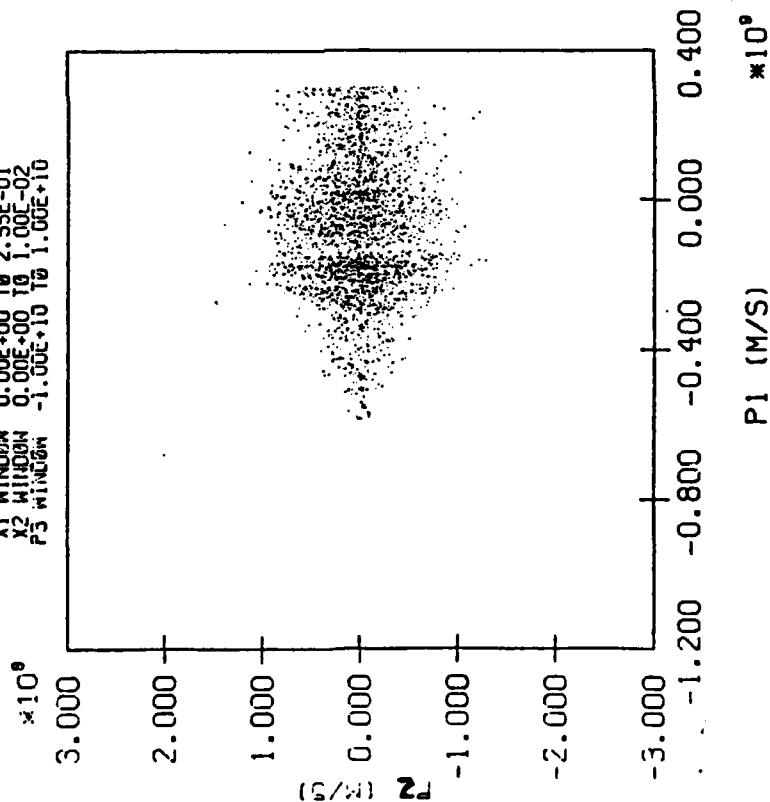


Figure 38. Phase Space Plot ( $P_z$  vs.  $Z$ ) Beam at  $t = 3000\Delta t$  in Dual Beam Case II.



MAGIC VERSION JUNE 1983 DATE 10/26/83  
SIMULATION NRL COLLECTIVE PARTICLE ACCELERATOR

PHASE-SPACE PLOT OF P2 VS. P1 AT TIME 4.20E-09 SEC  
SPECIES NUMBER 1 O/M RATIO -1.759E+11  
X1 WINDOW 0.00E+00 TO 2.55E-01  
X2 WINDOW 0.00E+00 TO 1.00E-02  
P3 WINDOW -1.00E+10 TO 1.00E+10



MAGIC VERSION JUNE 1983 DATE 10/26/83  
SIMULATION NRL COLLECTIVE PARTICLE ACCELERATOR

PHASE-SPACE PLOT OF P2 VS. P1 AT TIME 4.20E-09 SEC  
SPECIES NUMBER 1 O/M RATIO -1.759E+11  
X1 WINDOW 0.00E+00 TO 2.55E-01  
X2 WINDOW 0.00E+00 TO 1.00E-02  
P3 WINDOW -1.00E+10 TO 1.00E+10

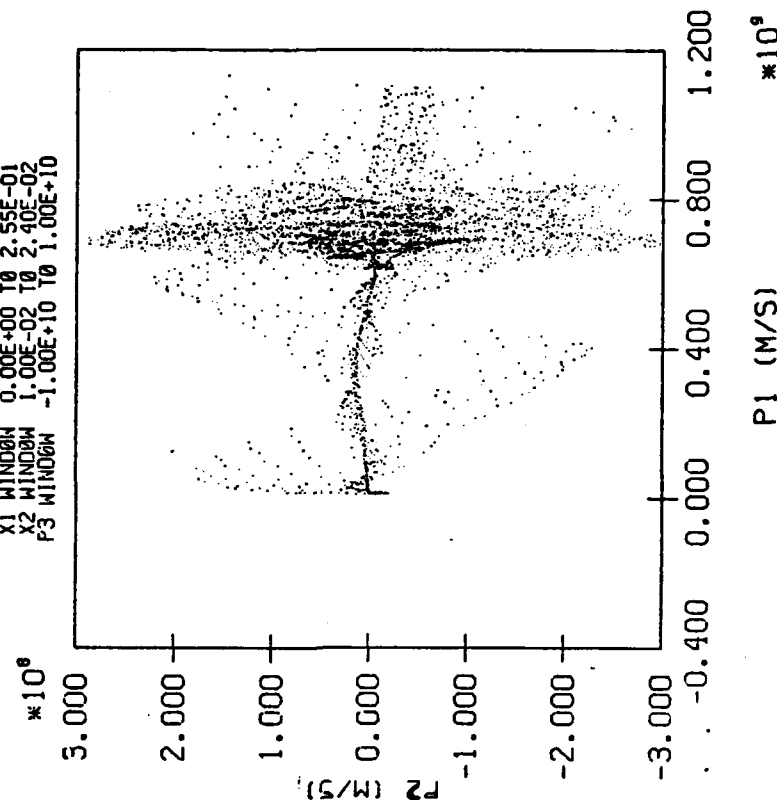


Figure 39. Plots of  $P_2$  versus  $P_1$  for Central Beam (left) and Hollow Beam (right) at  $t = 3000\Delta t$  in Dual Beam Case II.

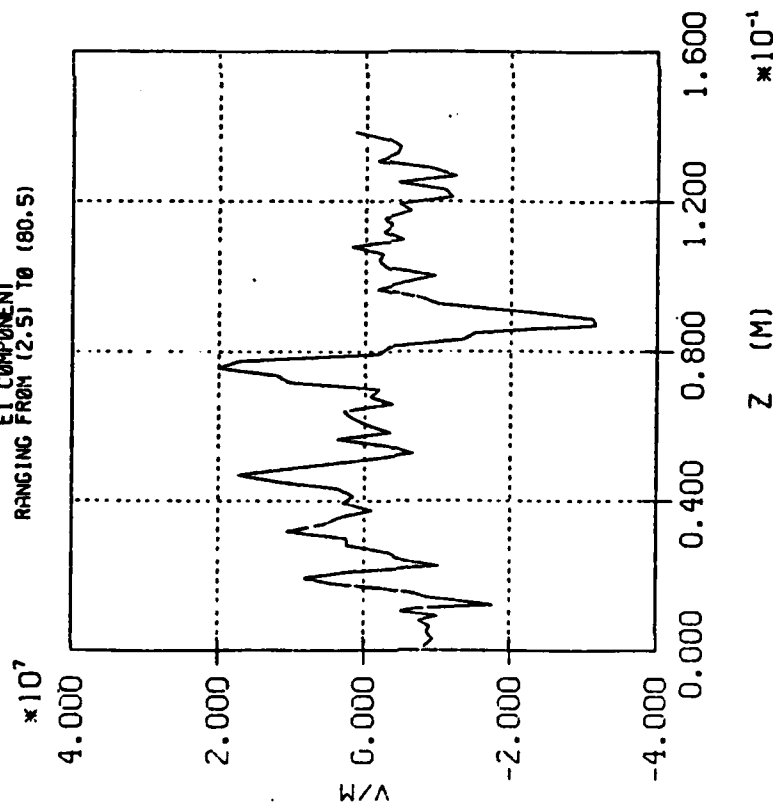
diamagnetic effect inside the hollow beam. This could thus lower the strength of the axial field which acts upon the central beam. Distributed evenly over the full length of the beams, this effect is probably small for the present case, but if there are any localized axial regions of particularly intense  $J_\theta$ , then the collimation of the central beam due to the applied  $B_z$  could be severely disrupted. The present simulations have purposely suppressed any azimuthal motion of the electrons in order to limit the electromagnetics to the first mode set,  $(E_z, E_R, B_\theta)$ , thereby streamlining the computational costs. Previous diode simulation experience (see References 17 and 18) have shown it to be very safe to ignore  $J_\theta$  in parameter ranges such as these. However, if the decision is made to renew the CPA experimental effort, new simulations should be conducted to test any revised and improved device configuration including  $J_\theta$  effects. For the present case, the observed virtual cathode seems bad enough to thwart proper operation. Adding  $J_\theta$  effects could only make things worse for the central beam. If methods are found to mitigate this virtual cathode effect, then a check on  $J_\theta$  is warranted.

To further appreciate the weakening effects of the hollow beam on the central beam, compare the axial profile of  $E_z$  just inside the central beam's outer radius for this run shown in Figure 40 to that of the previous run in Figure 29 for which only the central beam was present. The initial accelerating field at the far right has been cut in half. Furthermore, it is followed immediately by a decelerating region (the virtual cathode). Then the field oscillates about zero until hitting another strong decelerating field at about  $Z = 9.0$  cm (probably due to the electrons reflecting from the opposing cathode wall). The corresponding profile for the hollow beam in this case still exhibits the typical foilless diode beam form as shown in Figure 41.

The voltage characteristics for the device in this simulation are shown in Figure 42. The upper two plots display the time histories of the voltage pulses on the hollow cathode (left) and rod cathode (right).

MAGIC VERSION JUNE 1983 DATE 10/26/83  
SIMULATION NRL COLLECTIVE PARTICLE ACCELERATOR

RANGE PLOT AT TIME 4.20E-09 SEC  
E1 COMPONENT  
RANGING FROM (2.5) TO (80.5)



MAGIC VERSION JUNE 1983 DATE 10/26/83  
SIMULATION NRL COLLECTIVE PARTICLE ACCELERATOR

RANGE PLOT AT TIME 4.20E-09 SEC  
E1 COMPONENT  
RANGING FROM (70.5) TO (143.5)

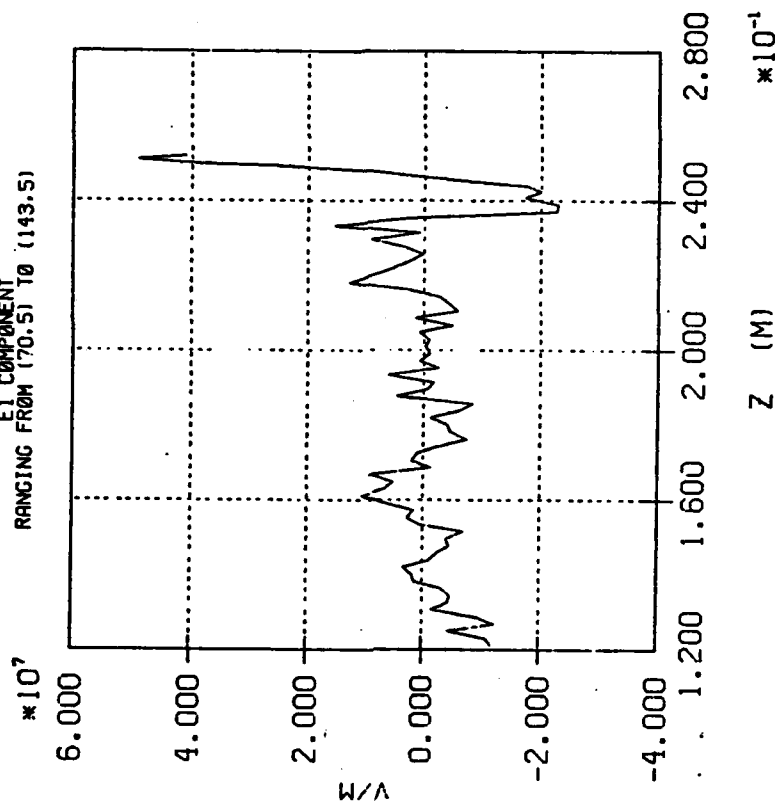
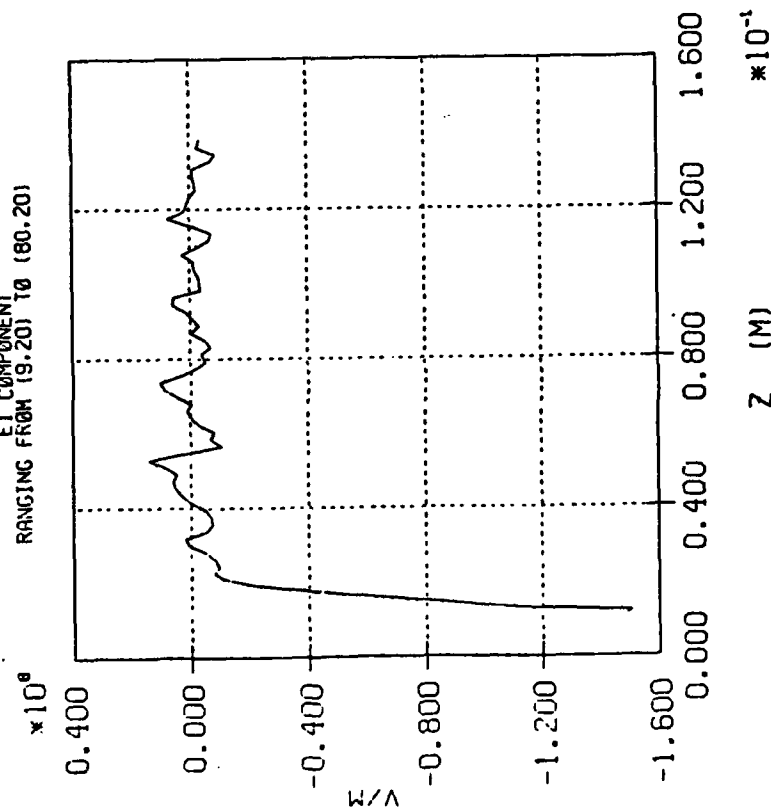


Figure 40. Axial Profile of  $E_z$  at  $R = 0.24$  cm (just inside central beam) at  $t = 3000\Delta t$  for Dual Beam Case II.

MAGIC VERSION JUNE 1983 DATE 10/26/83  
SIMULATION NRL COLLECTIVE PARTICLE ACCELERATOR

RANGE PLOT AT TIME 4.20E-09 SEC  
E1 COMPONENT  
RANGING FROM (9.20) TO (80.20)



MAGIC VERSION JUNE 1983 DATE 10/26/83  
SIMULATION NRL COLLECTIVE PARTICLE ACCELERATOR

RANGE PLOT AT TIME 4.20E-09 SEC  
E1 COMPONENT  
RANGING FROM (170.20) TO (143.20)

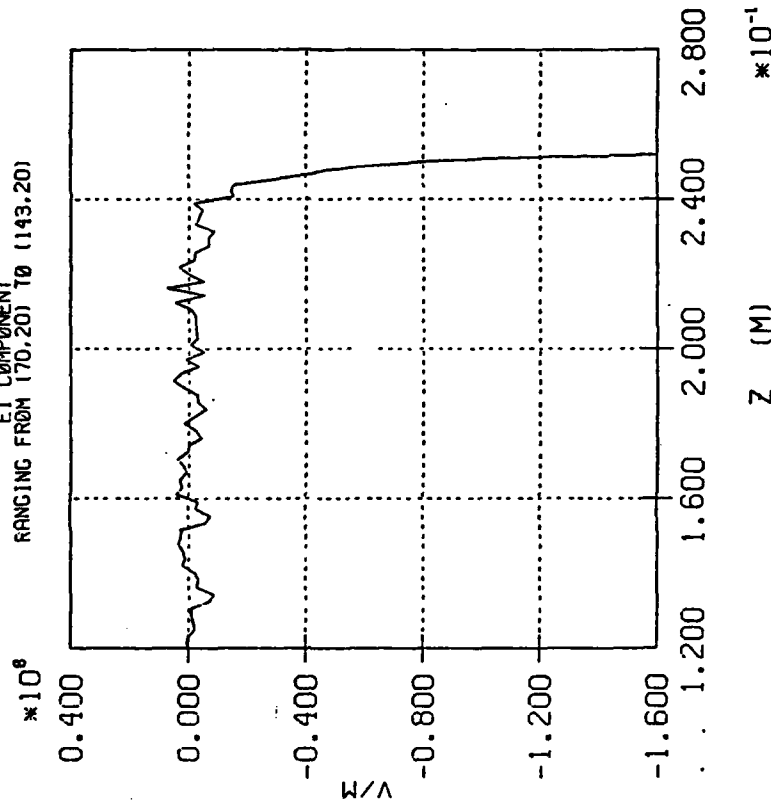


Figure 41. Axial Profile of  $E_z$  at  $R = 1.94$  cm (just inside hollow beam) at  $t = 300\Delta t$  for Dual Beam Case II.

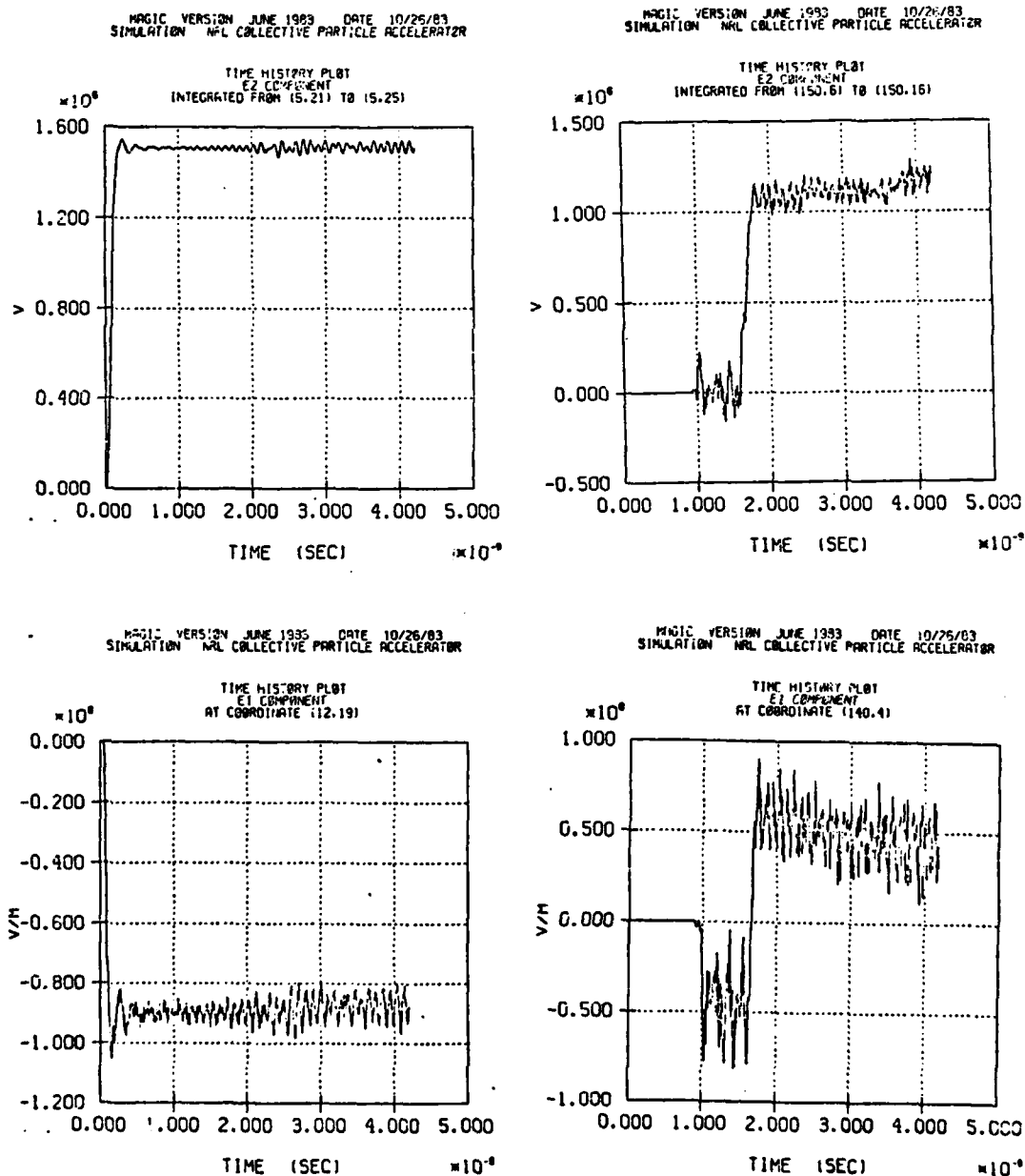
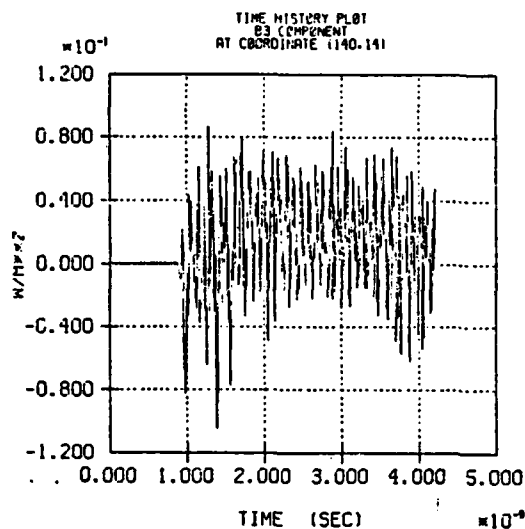


Figure 42. Time History Plots to Voltage on Hollow Cathode (top left), Voltage on Rod Cathode (top right),  $E_z$  near Tip of Hollow Cathode (bottom left), and  $E_z$  near Tip of Rod Cathode (bottom right) for Dual Beam Case II.

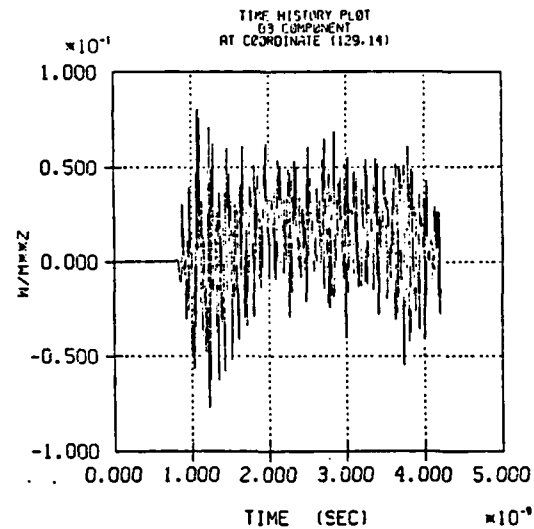
The plateau hollow cathode voltage is extremely close to the experimentally measured 1.5 MV while that for the rod cathode is closer to 1.1 MV compared to the observed 1.0 MV. The lower left plot traces  $E_z$  as a function of time at the hollow cathode tip and finds it to be quite steady at about  $-0.9 \times 10^8 \text{V/m}$ . The corresponding bottom right plot for  $E_z$  at the rod cathode tip shows a brief rise to  $0.5 \times 10^8 \text{V/m}$  followed by a gentle period of decay to  $0.42 \times 10^8 \text{V/m}$ .

Figure 43 presents the key diagnostic to this entire set of simulation runs, namely the measurements of the central beam axial currents in the presence of the hollow beam. The locations for these  $B_\theta$  measurements correspond exactly to those shown in Figure 31 for the central beam without the hollow beam. The change is rather dramatic. The sensors at 0.22, 2.235, and 4.565 cm from the rod cathode tip all show brief ( $\sim 1$  ns) rises to at most  $0.02 \text{ w/m}^2$  followed by quick declines to values of  $0.01 \text{ w/m}^2$  or less. The bottom right plot for the other end of the tube detects no significant, consistent axial current and, in fact, seems dominated by low-level displacement current noise, probably originating from the hollow beam. (The presence of these strong  $dE_z/dt$  oscillations inside the hollow beam argue for the future placement of the  $B_\theta$  sensor points much closer to the central beam to help sort out the desired signal from this background. This must be kept in mind experimentally too, although this computationally observed background  $B_\theta$  is probably of too high a frequency even to be detected on standard experimental hardware.) The peak, upstream central beam current that these measurements indicate is about 1.41 kA which quickly decays to 0.70 kA or less in approximately a nanosecond. This current is down by over a factor of three from the case without the hollow beam. It explains completely why no central beam propagation was detected in the full CPA experiment at NRL.

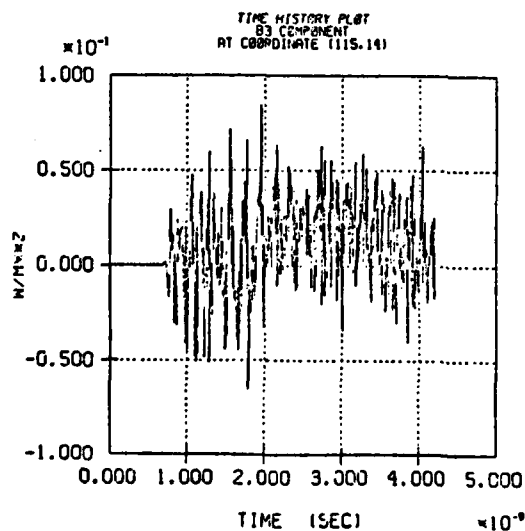
MAGIC VERSION JUNE 1983 DATE 10/26/83  
SIMULATION NRL COLLECTIVE PARTICLE ACCELERATOR



MAGIC VERSION JUNE 1983 DATE 10/26/83  
SIMULATION NRL COLLECTIVE PARTICLE ACCELERATOR



MAGIC VERSION JUNE 1983 DATE 10/26/83  
SIMULATION NRL COLLECTIVE PARTICLE ACCELERATOR



MAGIC VERSION JUNE 1983 DATE 10/26/83  
SIMULATION NRL COLLECTIVE PARTICLE ACCELERATOR

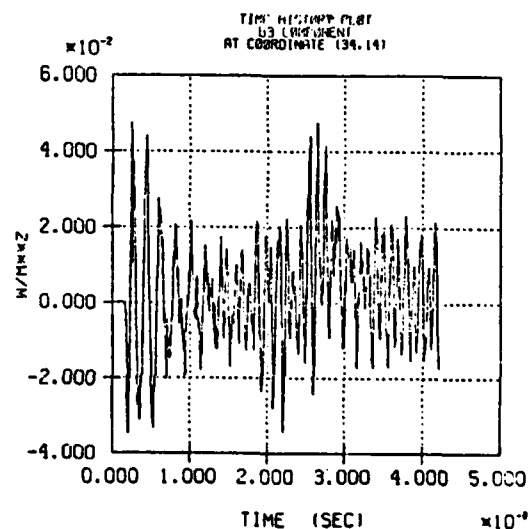


Figure 43. Time History Plots for  $B_\theta$  Measured at  $R = 1.41$  cm for Distances of 0.22 (top left), 2.235 (top right), 4.565 (bottom left), and 19.955 cm (bottom right) Downstream of Rod Cathode for Dual Beam Case II.

## 6. CONCLUSIONS

As a result of these numerical simulations, it can be concluded that the present configuration of the NRL Collective Particle Accelerator causes drastic reduction of the current carrying capacity of its central beam due to the formation of an effective, virtual cathode immediately adjacent to the physical rod cathode tip when the outer, hollow electron beam is present. At the same time, however, this weakened central beam is observed to propagate stably down the drift tube. It seems possible that modest redesign may be able to raise the central beam current to a level where useful CPA experiments could be conducted.

Key parameter adjustments which might lead to such a result include a lowering of hollow cathode voltage (and current) and/or a raising of rod cathode voltage. Possible changes of this nature must first be evaluated by the experimentalists in light of their effects on the desired acceleration mechanisms. Proposed adjustments should then be tested again via follow-on simulations to confirm their positive effects.



## 7. REFERENCES

1. Moshe Friedman, "A New Collective Particle Accelerator," NRL Memorandum Report 3724, February 1978 and M. Friedman, "The C.P.A.," IEEE Transactions on Nuclear Science, NS-26, No. 3, June 1979.
2. Peter J. Palmadesso, private communication.
3. Moshe Friedman, private communication.
4. B. Goplen, R. E. Clark, and J. McDonald, "Users' Manual for MAGIC/ Version - July 1981," Mission Research Corporation Report, MRC/WDC-R-016, July 1981.
5. B. Goplen, "Boundary Conditions for MAGIC," Mission Research Corporation Report, MRC/WDC-R-019, presented at the 23rd Annual APS Plasma Physics Division Meeting of 12-16 October 1981.
6. B. B. Godfrey and B. Goplen, "Practical Evaluation of Time-Biased Electromagnetic Field Algorithms for Plasma Simulations," AMRC-N-146, presented at the 22nd Annual APS Plasma Physics Division Meeting of 10-14 November 1980.
7. B. Goplen, R. E. Clark, and S. J. Flint, "Geometrical Effects in Magnetically Insulated Power Transmission Lines," Mission Research Corporation Report, MRC/WDC-R-001, April 1979.
8. W. A. Seidler, B. Goplen, and W. Thomas, "Investigation of Enhanced Electron Current Transport in a Dielectric Lined Cavity," IEEE Transactions on Nuclear Science, NS-26, No. 6, December 1979.
9. D. B. Seidel, B. C. Goplen, and J. P. VanDevender, "Simulation of Power Flow in Magnetically Insulated Convolutes for Pulsed Modular Accelerators," presented at the 14th Pulse Power Modulator Symposium, 3-5 June 1980.
10. B. B. Godfrey, Proceedings of the Ninth Conference on Numerical Simulation of Plasmas, Paper OD-4, 1980.
11. B. Goplen, "Boundary Conditions for MAGIC," MRC/WDC-R-019, October 1981.
12. Sandia Report SAND82-0192, February 1982.
13. R. E. Clark, W. M. Bollen, J. McDonald, and B. Goplen, "Simulation of Microwave Devices Using MAGIC," MRC/WDC-R-040, November 1982.
14. R. J. Barker, S. A. Goldstein, and R. E. Lee, "Computer Simulation of Intense Electron Beam Generation in a Hollow Cathode Diode," NRL Memo Report 4279, 1980.

15. A. T. Drobot, R. J. Barker, and S. A. Goldstein, "Numerical Simulation of Ion Production from the AURORA Diode," IEEE Int. Conf. on Plasma Science, Madison, Wisconsin; 1980.
16. R. J. Barker, C. W. Roberson, and F. Make, "Numerical Simulation of High Energy Light Ion Beam Flow Through a Foilless Diode," NRL Memo Report 5058, July 1983.
17. R. J. Barker and S. A. Goldstein, "Finite Axial Magnetic Field Effects in the Electron Reflexing Double Diode," Bull. Am. Phys. Soc. 24, 950; 1979.
18. R. J. Barker, S. A. Goldstein, and A. T. Drobot, "Computational Study of Magnetic Dam Effects in a High Impedance Diode," NRL Memo Report 4642, 1981.

## APPENDIX A

### DISSPATCH: A Software Package to Interface DISSPLA Calls with NCAR Graphics

Mission Research Corporation's two-dimensional, electromagnetic, particle-in-cell code, MAGIC, is designed to operate with the DISSPLA graphics software package written by the ISSCO Graphics Corporation. The popularity of DISSPLA nationwide has made it a virtual standard in the field and thus the most logical choice for use in connection with any transportable code. The VAX/780 computer available to Code 4780 at the Naval Research Laboratory does not, unfortunately, have the DISSPLA library available to it. Instead, it uses the NCAR Graphics software package. When MAGIC was moved to the NRL VAX, the decision was made to construct a software library which translates the DISSPLA subroutine calls in MAGIC to a form recognizable to the NCAR Graphics library. This approach necessitated the construction of a set of subroutines whose names corresponded to the desired DISSPLA CALLS and which, in turn, CALLED the combination of NCAR graphics routines which most closely accomplished the desired DISSPLA results. The set of new subroutines, written by MRC's James McDonald, forms an interface package which has been dubbed, DISSPATCH. Its use on a system which hosts NCAR graphics eliminates, as far as possible, the need for direct modification of any existing code which is already written in terms of DISSPLA. The price the user must pay for this convenience is the failure to fully utilize the real power of either DISSPLA or NCAR. Still, the plots which resulted from our use of DISSPATCH were very pleasing to the eye and looked infinitely better than the line-printer graphics which we would have otherwise been left with.

The user is also cautioned that the present version of DISSPATCH only deals with a subset of the total library of DISSPLA calls. Still, that subset is large enough to handle the likely needs of most users.

Specifically, the MRC MAGIC code required NCAR patches for the following list of DISSPLA calls:

ANGLE  
AREA2D  
AXSPLT  
COMPRS  
CURVE  
DONEPL  
DOT  
ENDPL  
FRAME  
GRACE  
GRAF  
GRID  
HEIGHT  
MARKER  
MESSAG  
MRSCOD  
NOCHEK  
PAGE  
PHYSOR  
RESET  
SCLPIC  
THKFRM  
XMESS  
XNAME  
YNAME.

These 25 separate calls were subdivided into four groups according to the manner in which they were handled by DISSPATCH. The first group was considered "expendable." These were deemed to be not important enough to warrant the trouble of writing NCAR counterparts. This group included GRACE, MARKER, NOCHEK, SCLPIC, and THKFRM. This was coded into DISSPATCH using the set of dummy subroutines shown in Figure A-1.

The second group consisted of all DISSPLA calls which have NCAR counterparts of the same name and very similar function. At present, there is only one member in this group, namely, CURVE. In DISSPLA, the call to CURVE is described as<sup>†</sup>

CALL CURVE (XARAY, YARAY, NPNTS, IMARK)

---

<sup>†</sup> DISSPLA Users Manual, Integrated Software Systems Corp.,  
San Diego, California (1981)

```
C
C
C      SUBROUTINE GRACE(X)
      RETURN
      END
C
C      SUBROUTINE MARKER(I)
      RETURN
      END
C
C      SUBROUTINE NOCHEK
      RETURN
      END
C
C      SUBROUTINE SCLPIC(X)
      RETURN
      END
C
C      SUBROUTINE THKFRM(X)
      RETURN
      END
```

Figure A-1. The "Expendable" DISSPLA Calls.

where

'XARRAY = name of array containing X values  
YARRAY = name of array containing Y values  
NPNTS = number of points to be plotted  
IMARK = frequency of marker symbols.

The following NCAR call<sup>†</sup> differs only in the number of arguments used:

CALL CURVE (X, Y, N)

where

X = an array of X coordinates  
Y = an array of Y coordinates  
N = the number of points on the curve.

Therefore, the DISSPLA call to CURVE can be used as-is with the IMARK argument being ignored by NCAR which will automatically plot every point.

The third "group" also contains only one member at present. This group is characterized by DISSPLA calls which have NCAR counterparts of the same name but different functions. The subroutine, FRAME, fits into this group. In DISSPLA, a call to FRAME draws a heavy boarder around the subplot area while in NCAR graphics the same call to FRAME advances the plotter one frame (similar to DISSPLA's ENDPL call). This disparity in functions defied any simple handling with DISSPATCH. To avoid the redundancy in names, a subroutine was added to DISSPATCH which emulated DISSPLA's FRAME with NCAR graphics but which was now given the name, FRAMER. Implementation of this feature with MAGIC required the changing of every occurence of "FRAME" to "FRAMER" in that code. A listing of the

---

<sup>†</sup> The System Plot Package, NCAR Technical Note NCAR-TN/162+1A,  
National Center for Atmospheric Research, Boulder, Colorado (1981)

new subroutine is provided in Figure A-2. It references a graphics COMMON block, DISCOM FOR, which is shared by other members of DISSPATCH and which is shown in Figure A-3.

The final group of subroutines forms the bulk of the DISSPATCH package and accurately embodies the philosophy of emulating DISSPLA calls with NCAR graphics "translations." This group consists of the following:

ANGLE  
AREA2D  
AXSPLT  
COMPRS  
DONEPL  
DOT  
ENDPL  
GRAF  
GRID  
HEIGHT  
MESSAG  
MRSCOD  
PAGE  
PHYSOR  
RESET  
XMESS  
XNAME  
YNAME.

The listings for these subroutines are provided in Figure A-4. It can be seen that an outside subroutine, PHYINT, is called by FRAMER, GRID, HEIGHT, and MESSAG. That utility algorithm is included in DISSPATCH to convert DISSPLA page units (inches relative to the physical origin) to NCAR's plotter address units. Its listing can be found in Figure A-5.

The ultimate question, of course, is "How effective has the DISSPATCH package been at improving the graphics output by MAGIC at NRL?" The answer is best given by presenting samples of the "before" and "after" plots. Figure A-6 is a sample time history curve as generated by the line-printer graphics. There are clearly significant problems in trying to discern the "wiggles" present in that curve. For comparison, Figure A-7 shows an even more complicated, longer time curve using DISSPATCH. Now, even the smallest "wobble" is clearly visible. Another key MAGIC

C  
C  
C

SUBROUTINE FRAMER  
INCLUDE 'DISCOM.FOR'

C

CALL PHYINT(0., 0., MX0, MY0)  
CALL PHYINT(AXX, AXY, MX, MY)  
CALL FRSTPT(MX0, MY0)  
CALL VECTOR(MX, MY0)  
CALL VECTOR(MX, MY)  
CALL VECTOR(MX0, MY)  
CALL VECTOR(MX0, MY0)  
RETURN  
END

Figure A-2. The NCAR Replacement for DISSPLA's FRAME.



```
LOGICAL PHYDEF  
COMMON /DISPAR/  PAGEX, PAGEY, PFRACX, PFRACY, AXX, AXY, CHRWID,  
1                CHRHGT, ISIZ, CHRANG, IOR, LXNAME(20),IXNAME,  
2                LYNAM(20), IYNAME, XOR, XST, XMX, YOR, YST, YMX, NDIVX,  
3                NDIVY, PHX, PHY, PHYDEF, LINETYPE
```

Figure A-3. The COMMON Block for DISSPATCH.

```

C
C
SUBROUTINE ANGLE(DEG)
  INCLUDE 'DISCOM.FOR'
C
  CHRANG = DEG
  IOR = INT(DEG)
  RETURN
  END
C
C
C
SUBROUTINE AREAD2D(X,Y)
  INCLUDE 'DISCOM.FOR'
C
  AXX = X
  AXY = Y
  IF (. NOT .PHYDEF) CALL PHYSOR(0.6 + (PAGEX-AXX)/2.0,(PAGEY-AXY)/2.0)
  RETURN
  END
C
C
C
SUBROUTINE AXSPLT(AMIN, AMAX, AXMAX, ORIG, STEP, AXIS)
C
  DIMENSION AMAN(4), NDIVA(3)
  DATA MANMAX / 4 / ,
1    AMAN / 1.0, 2.0, 4.0, 5.0 / ,
2    NDVMAX / 3/ ,
3    NDIVA / 4, 5, 6 /
C  IGRT(Z) = INT(Z-AINT(Z) + 1.0) + INT(Z) - 1
    IF (AMAX.GE.AMIN) GO TO 50
    STP = AMAX
    AMAX = AMIN
    AMIN = STP
50  CONTINUE
C
  BEST = 0.0
  DO ND = 1, NDVMAX
    NDIV = NDIVA(ND)
    STP = (AMAX-AMIN)/NDIV
    LSTP = IGRT(ALOG10(ABS(STP)))
    MSTP = 0

```

Figure A-4. The DISSPATCH DISSPLA Emulators.

AD-A135 533

NUMERICAL SIMULATIONS OF THE NRL COLLECTIVE PARTICLE  
ACCELERATOR(U) MISSION RESEARCH CORP ALEXANDRIA VA  
R J BARKER NOV 83 MRC/WDC-R-073 N00014-83-C-0519

2/2

UNCLASSIFIED

F/G 12/1

NL

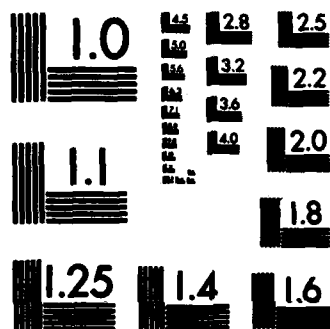


END

FORM

104

gtr



MICROCOPY RESOLUTION TEST CHART  
NATIONAL BUREAU OF STANDARDS-1963-A

```

100  MSTP = MSTP + 1
      IF (MSTP .GT .MANMAX) THEN
        MSTP = 1
        LSTP = LSTP + 1
      END IF
      STP = AMAM(MSTP) * 10.0 ** LSTP
      RMIN = IGRT(AMIN/STP) * STP
      RMAX = RMIN + STP * NDIV
      IF (RMAX .LT .AMAX) GO TO 100
      GOODNESS = (AMAX-AMIN)/(RMAX-RMIN)
      IF (GOODNESS .GT .BEST) THEN
        BEST = GOODNESS
        ORIG = RMIN
        STEP = STP
        AXIS = FLOAT(NDIV)
      END IF
    END DO
    RETURN
  END

```

C  
C  
C

```

SUBROUTINE COMPRS
  INCLUDE 'DISCOM.FOR'

```

C

```

  CALL SETI(12, 12)
  CALL PAGE(8.5, 11.0)
  CALL HEIGHT(.14)
  CALL ANGLE(0.0)
  RETURN
  END

```

C  
C  
C

```

SUBROUTINE DONEPL
  CALL FLUSH
  RETURN
  END

```

C  
C  
C

```

SUBROUTINE DOT
  INCLUDE 'DISCOM.FOR'

```

C

```

  CALL OPTN('DPATTERN', 4681)
  RETURN
  END

```

Figure A-4 (continued).

```

C
C
C
SUBROUTINE ENDPL(I)
CALL FRAME
RETURN
END

C
C
C
SUBROUTINE GRAF(XORIGD, XSTPD, XMAXD, YORIGD, YSTPD, YMAXD)
INCLUDE 'DISCOM.FOR'

C
DIMENSION IFMTX(3), IFMTY(3)

C
XORIG = XORIGD
XSTP = XSTPD
XMAX = XMAXD
YORIG = YORIGD
YSTP = YSTPD
YMAX = YMAXD
NDIVX = INT((XMAX-XORIG)/XSTP + .5)
NDIVY = INT((YMAX-YORIG)/YSTP + .5)
XFAC = PFRACX/PAGEX
YFAC = PFRACY/PAGEY
CALL SET(PHY*XFAC,(PHX + AXX)*XFAC,PHY*YFAC,(PHY + AXY) * YFAC,
1      XORIG, XMAX, YORIG, YMAX, 1)
IF (IXNAME.EQ.0 .AND. IYNAME.EQ.0) RETURN
CALL FRAMER
IXEX = INT(ALOG10(MAX(ABS(XORIG), ABS(XMAX))))
ENCODE(10,100, IFMTX) -IXEX
100 FORMAT('(', I3, 'PF6.3)')
IYEX = INT(ALOG10(MAX(ABS(YORIG), ABS(YMAX))))
ENCODE(10,100, IFMTY) -IYEX
CALL LABMOD(IFMTX, IFMTY, 6, 6, ISIZ, ISIZ, 0, 2*ISIZ, 0)
CALL HALFAX(NDIVX, 1, NDIVY, 1, XORIG, YORIG, 1,1)
XL = XMESS(LXNAME, IXNAME, 0., 0.)
CALL MESSAG(LXNAME, IXNAME, (AXX-XL)/2.0, -5.0*CHRHGT)
IF (IXEX.NE.0) THEN
    CALL MESSAG('*10', 3, AXX-1.5*CHRWD,-5.0*CHRHGT)
    NC = 1 + INT(ALOG10(FLOAT(ABS(IXEX)) + .001))
    IF (NC.LT.1) NC = 1
    IF (IXEX.LT.0) NC = NC + 1
    ENCODE(NC, 200, EXP) IXEX
200    FORMAT(I<NC>)
    CALL HEIGHT(CHRHGT/2.0)

```

Figure A-4 (continued).

```

        CALL MESSAG(EXP,NC,AXX + 3.0*CHRWID, -9.0*CHRHGT)
        CALL HEIGHT(CHRHGT*2.0)
    END IF
    YL = XMESS(LYNAME, IYNAME, 0., 0.)
    CALL ANGLE(90.0)
    CALL MESSAG(LYNAME, IYNAME, -8.0*CHRWID,(AXY-YL)/2.0)
    CALL RESET('ANGLE')
    IF (IYEX.NE.0) THEN
        CALL MESSAGE('*10', 3, -4.0*CHRWID,AXY + 2.0*CHRHGT)
        NC = 1 + INT(ALOG10(FLOAT(ABS(IYEX)) + .001))
        IF (NC.LT.1) NC = 1
        IF (IYEX.LT.0) NC = NC + 1
        ENCODE(NC, 200, EXP) IYEX
        CALL HEIGHT(CHRHGT/2.0)
        CALL MESSAG(EXP, NC, -2.0*CHRWID, AXY + 5.0*CHRHGT)
        CALL HEIGHT(CHRHGT *2.0)
    END IF
    RETURN
END

C
C
C
SUBROUTINE GRID(IX,IY)
    INCLUDE 'DISCOM.FOR'
C
    DO I = 1, NDIVX-1
        CALL PHYINT(I*AXX/NDIVX, -CHRHGT, MX, MY)
        CALL FRSTPT(MX, MY)
        CALL PHYINT(I*AXX/NDIVX, AXY, MX, MY)
        CALL VECTOR(MX, MY)
    END DO
    DO I = 1, NDIVY-1
        CALL PHYINT(-CHRWID, I*AXY/NDIVY, MX, MY)
        CALL FRSTPT(MX, MY)
        CALL PHYINT(AXX, I*AXY/NDIVY, MX, MY)
        CALL VECTOR(MX, MY)
    END DO
    RETURN
END

C
C
C
SUBROUTINE HEIGHT(HGT)
    INCLUDE 'DISCOM.FOR'
C
    CHRHGT = HGT
    CHRWID = HGT*6.0/7.0

```

Figure A-4 (continued).

```

CALL PHYINT(0.0, 0.0, I, J)
CALL PHYINT(CHRWID, 0.0, IZ, J)
ISIZ = IZ-1
RETURN
END

C
C
C
SUBROUTINE MESSAG(ICHARS, N, X, Y)
INCLUDE 'DISCOM.FOR'

C
DIMENSION ICHARS(20)
CHARACTERS*80 CHARS

C
C
CONVERT TO UPPER CASE.
NW = 1 + (N-1)/4
WRITE(CHARS, '(20A4)') (ICHARS(I), I = 1, NW)
DO I = 1, N
  K = ICHAR(CHARS(I : I))
  IF (K.GE.97 AND K.LE.122) K = K - 32
  CHARS(I:I) = CHAR(K)
END DO

C
CALL PHYINT(X, Y, MX, MY)
CALL PWRIT(MX, MY, %REF(CHARS), N, ISIZ, IOR, -1)
RETURN
END

C
C
C
SUBROUTINE MRSCOD(TLENG, NMRKSP, RATR)
INCLUDE 'DISCOM.FOR'

C
CALL OPTN('DPATTERN', .255)
RETURN
END

C
C
C
SUBROUTINE PAGE(X, Y)
INCLUDE 'DISCOM.FOR'

```

Figure A-4 (continued).



```

C
  PAGEX = X
  PAGEY = Y
  PMAX = MAX(X, Y)
  PFRACX = PAGEX/PMAX
  PFRACY = PAGEY/PMAX
  RETURN
  END

C
C
C
  SUBROUTINE PHYSOR(X, Y)
  INCLUDE 'DISCOM.FOR'

C
  DATA PHYDEF / .FALSE. /

C
  PHX = X
  PHY = Y
  PHYDEF = .TRUE.
  RETURN
  END

C
C
C
  SUBROUTINE RESET(X)
  INCLUDE 'DISCOM.FOR'

C
  DATA DOT / '544F44'X /

C
  IF(X.EQ.'HEIG') CALL HEIGHT(.14)
  IF(X.EQ.'ANGL') CALL ANGLE(0.0)
  IF(X.EQ.DOT .OR. X.EQ.'DASH'
1      .OR. X.EQ.'MRSC') CALL OPTN('DPATTERN',-1)
  RETURN
  END

C
C
C
  FUNCTION XMES(LNESS,IMESS,DUM1, DUM2)
  INCLUDE 'DISCOM.FOR'

C
  DIMENSION LMESS(20)

C
  XMES = CHRWD*IMESS
  RETURN
  END

```

Figure A-4 (continued).

```

C
C
C
SUBROUTINE XNAME(LXNAM, IXNAM)
  INCLUDE 'DISCOM.FOR'
C
  DIMENSION LXNAM(20)
C
  IF(IXNAM.NE.0) THEN
    DO I = 1, (IXNAM-1)/4 + 1
      LXNAME(I) = LXNAM(I)
    END DO
  END IF
  IXNAME = IXNAM
  RETURN
END

C
C
C
SUBROUTINE YNAME(LYNAM, IYNAM)
  INCLUDE 'DISCOM.FOR'
C
  DIMENSION LYNAM(20)
C
  IF(IYNAM.NE.0) THEN
    DP I = 1, (IYNAM-1)/4 + 1
    LYNAME(I) = LYNAM(I)
  END DO
  END IF
  IYNAME = IYNAM
  RETURN
END

```

Figure A-4 (concluded).

```

C
C
C
SUBROUTINE PHYINT(X,Y,IX,IY)
  INCLUDE 'DISCOM.FOR'
C
  CALL GETSI(IEX, IEY)
  IX = INT(2**IEX*(X + PHX)/PAGEX*PFRACX)
  IY = INT(2**IEY*(Y + PHY)/PAGEY*PFRACY)
  RETURN
END

```

Figure A-5. The PHYINT Utility Routine.

8

1



MAGIC VERSION JUNE 1983 DATE 9/11/83  
SIMULATION NRL COLLECTIVE PARTICLE ACCELERATOR

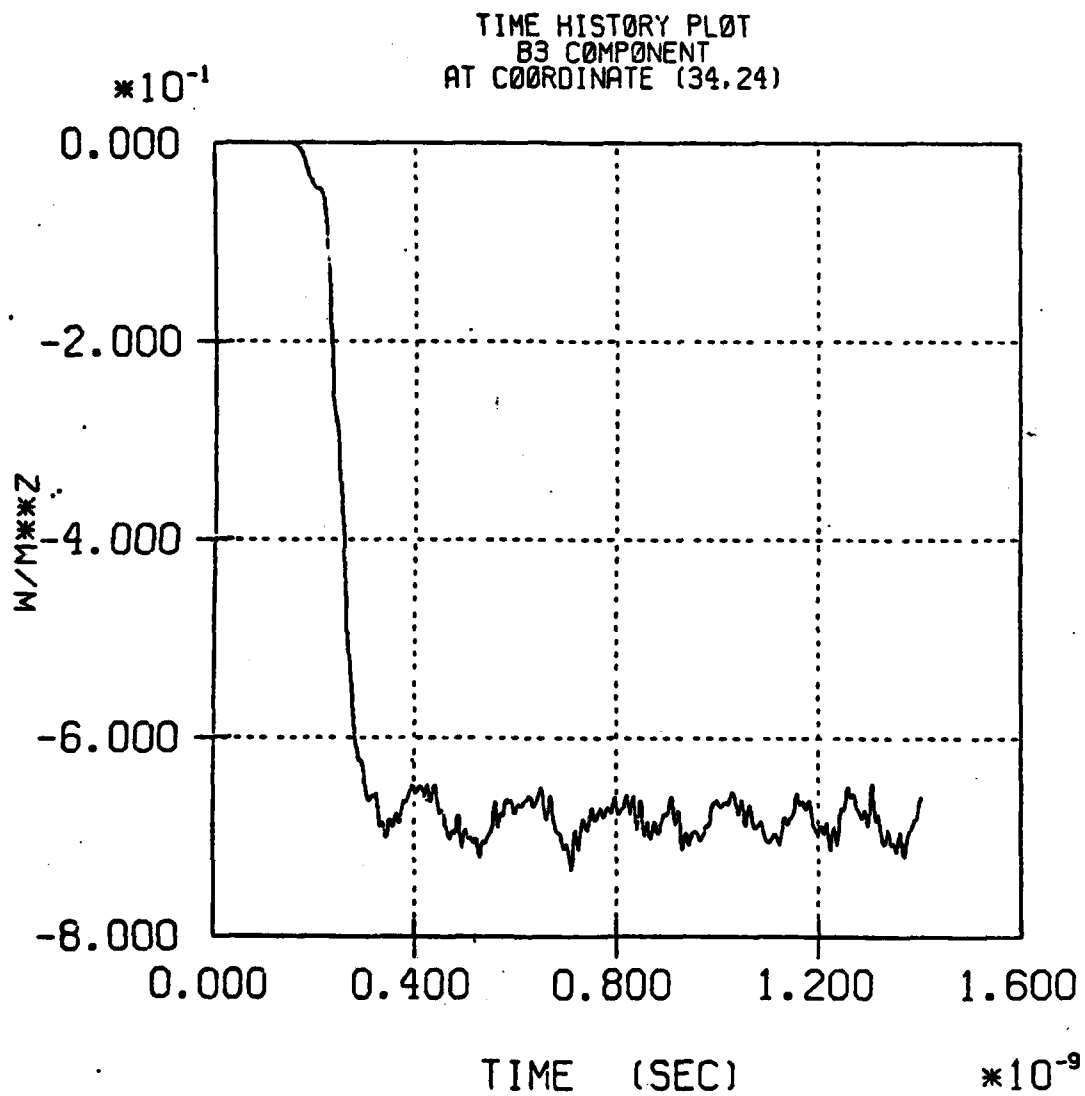


Figure A-7. Sample DISSPATCH Curve.

diagnostic consists of particle position plots. The best approximation a line printer can make is shown in Figure A-8. Much useful information is given in the plot with conducting surfaces labeled with C's and the symmetry boundary labeled with S's. In addition, the spacings between the C's and S's correspond to the actual, variable grid spacing used in the simulation mesh. However, the most important part of the plot namely the particle positions give virtually no resolution of stream fine structure. This is in dramatic contrast to the DISSPATCH particle position plot of Figure A-9.

The complete source listing for DISSPATCH may be found on the NRL, Building A50 VAX/780 on node [BARKER.MCD]DISSPLA.FOR. The corresponding object code is at [BARKER.MCD]DISSPLA.OBJ. It is hoped that other users will exercise the package and make suggestions for its improvement and/or expansion.

MAGIC Version: JUNE 1993 Date: 7/29/83  
Simulation: NRL CHARGED PARTICLE ACCELERATOR

TRAJECTORY PLOT OF ELECTRONS ( ISPE = 1 )  
AT TIME: 7.00E-11 SEC FOR 1 TIME STEPS

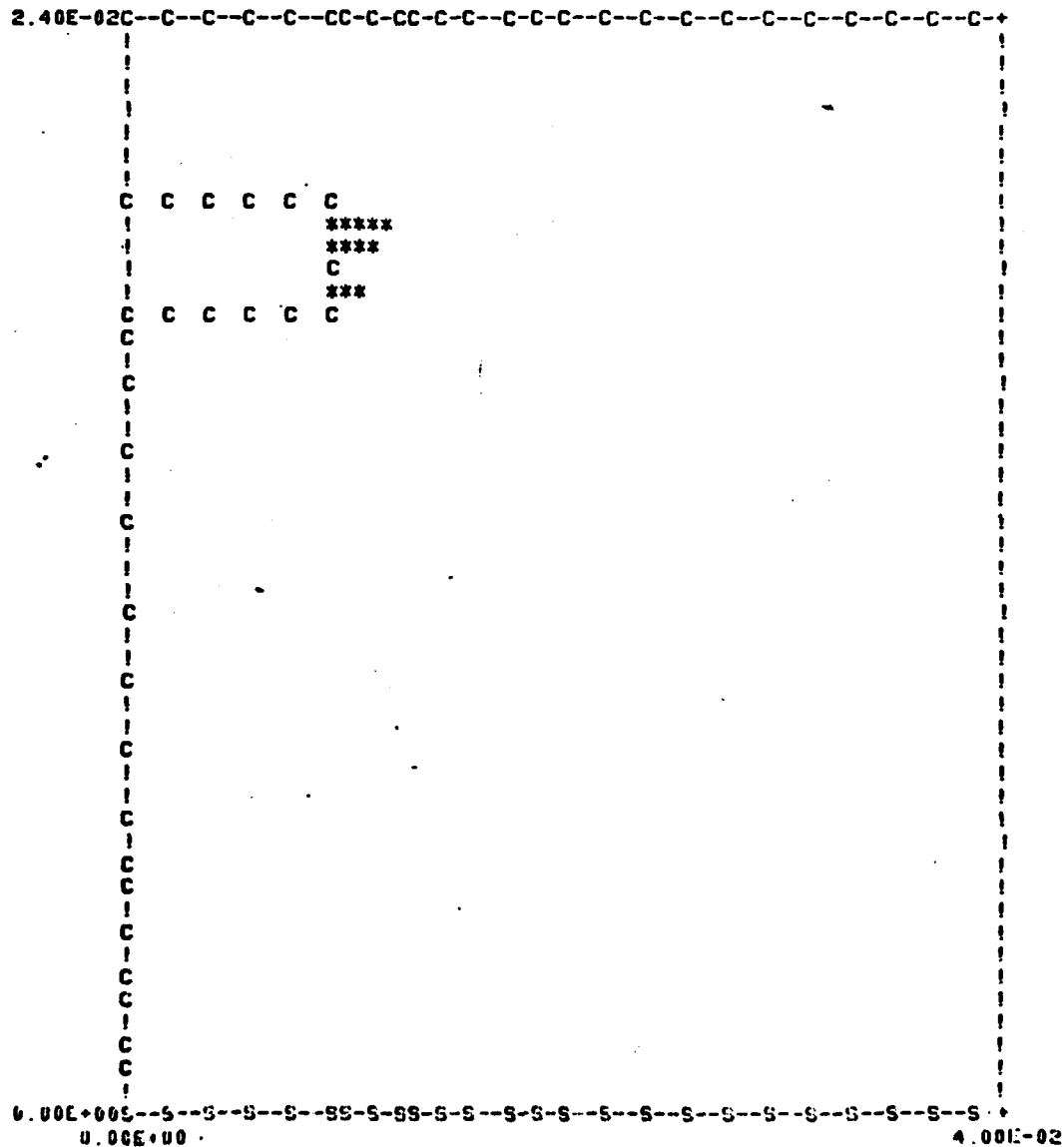


Figure A-8. Sample Line Printer Particle Plot.

MAGIC VERSION JUNE 1983 DATE 8/17/83  
SIMULATION NRL COLLECTIVE PARTICLE ACCELERATOR

TRAJECTORY PLOT OF ELECTRONS ( ISPE = 1 )  
AT TIME 7.00E-10 SEC FOR 1 TIME STEPS

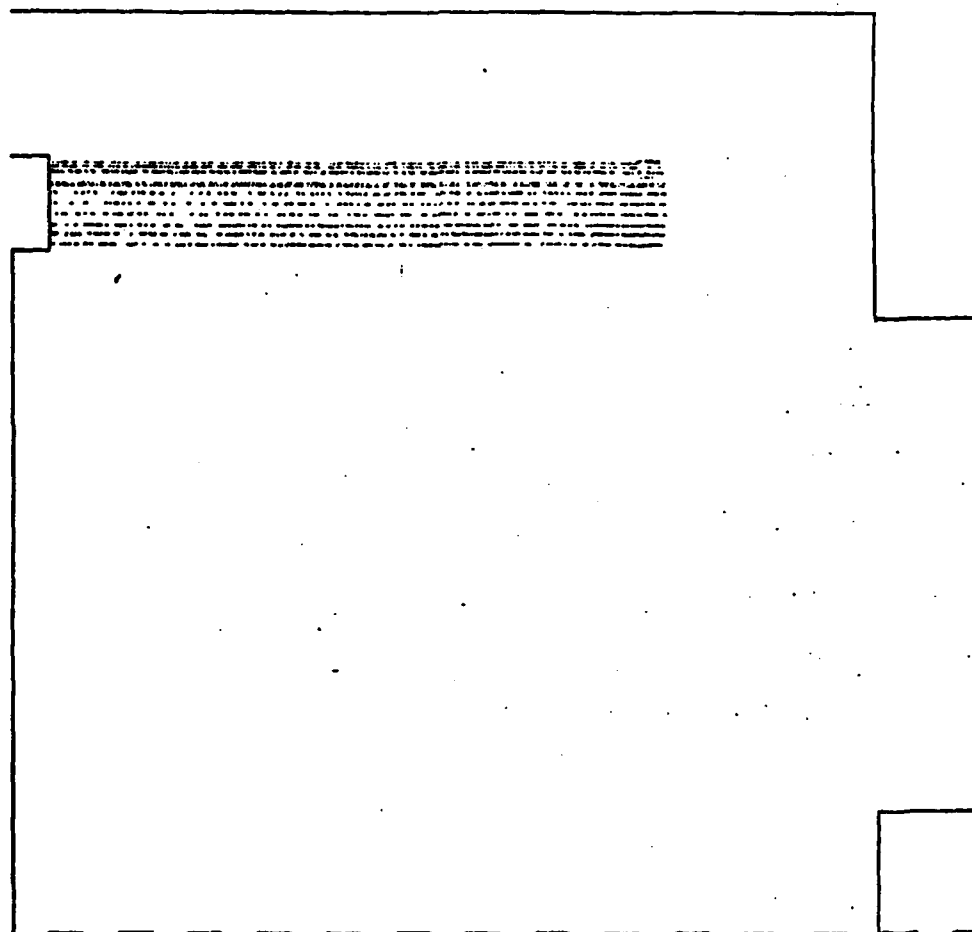


Figure A-9. Sample DISSPATCH Particle Plot.



**END**

**FILMED**

**1-84**

**DTIC**